Università degli Studi di Udine
Dottorato di Ricerca in
Tecnologie Chimiche ed Energetiche

PERFORMANCE EVALUATION OF TURBINE TRAILING EDGE COOLING CHANNELS UNDER STATIC AND ROTATING CONDITIONS

Dott. Claudio MUCIGNAT

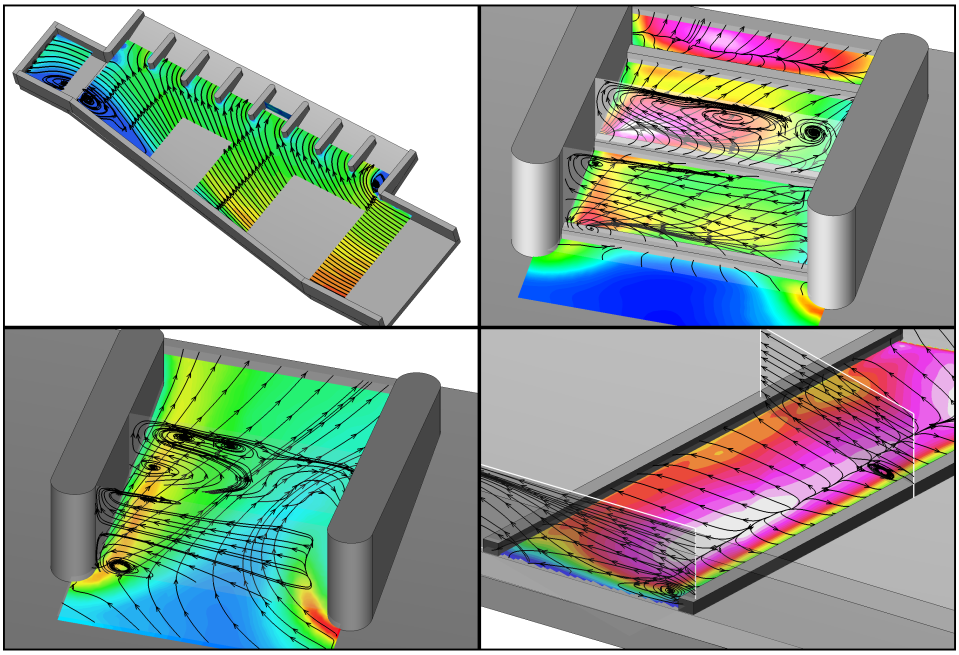

COMMISSIONE

Prof. Giovanna BARIGOZZI	Revisore
Dr. Filippo COLETTI	Revisore
Prof. Tommaso ASTARITA	Commissario
Prof. Pietro DE PALMA	Commissario
Prof. Enrico NOBILE	Commissario
Prof. Luca CASARSA	Supervisore
Dr. Alessandro ARMELLINI	Co-Supervisore

Prof. Alfredo SOLDATI	Coordinatore del Dottorato

Tesi di dottorato di *Claudio Mucignat*, discussa presso l'Università degli Studi di Udine

---

Author's Web Page: www.diegm.uniud.it/gmse/mucignat_claudio

Author's e-mail: claudio.mucignat@uniud.it claudio.mucignat@gmail.com

Author's address:

Dipartimento di Ingegneria Elettrica
Gestionale e Meccanica
Università degli Studi di Udine
Via delle Scienze, 106
33100 Udine – Italia
tel. +39 0432 558253
fax. +39 0432 558251
web: `http://www.diegm.uniud.it`

COVERART

Top-left: contours of time averaged velocity field and stream tracers on the symmetry plane, Ro=0.23, Re=20000.

Top-right: detail of Nusselt Number distribution at the channel suction side wall inside a inter pedestal trailing edge outlet and time averaged stream-tracers in planes xy', xz_1, and $xz_3$for configuration G2.

Bottom-left: detail of Nusselt Number distribution at the channel suction side wall inside a inter pedestal trailing edge outlet and time averaged stream-tracers in planes xy', xz_1, and $xz_3$for configuration G0.

Bottom-right: Bottom-left: detail of Nusselt Number distribution at the channel suction side wall between the 3^{RD} and 4^{TH} rib and time averaged stream-tracers in planes xy_{4-G1}, $xz-A$, and $xz-B$, configuration G1.

La scienza è una cosa meravigliosa... per chi non deve guadagnarsi da vivere con essa.

Albert Einstain

Abstract

Trailing edge cooling cavities in modern gas turbine airfoils play an important role in maintaining the trailing-edge temperature at levels consistent with blade design life. In this study a complete aero-thermal analysis on a trailing edge cooling duct is reported. The passage resembles the ones currently employed in high performance turbo-gas engines, and it is characterized by a trapezoidal cross-section of high aspect-ratio and coolant discharge at the blade tip and along the wedge-shaped trailing edge, where seven elongated pedestals are also installed. The tests were performed under engine similar conditions with respect to both Reynolds (Re = 20,000) and Rotation (Ro = 0, 0.23) numbers. Three different configurations have been taken into account, namely the smooth channel and two others characterised by the adoption of *riblets* in different portions of the duct.

The flow velocity was measured by means of 2D and Stereo-PIV techniques applied in the absolute frame of reference. In the rotating tests, the relative velocity fields were obtained through a pre-processing procedure of the PIV images developed on purpose. The thermal field was measured by means of Liquid Crystal Thermography.

In the static case, it has been proven that the 3D separation structures that surround the pedestals have a strong influence on the thermal field. Furthermore, it has been shown that the adoption of turbulence promoters is the radial development region is the most effective way to increase the performance of the device. A substantial modification of the whole flow behaviour due to rotational effects was observed, nevertheless no trace of rotation induced secondary Coriolis vortices has been found because of the progressive flow discharge along the trailing edge. For Ro = 0.23, at the channel inlet the high aspect-ratio of the cross section enhances inviscid flow effects which determine a mass flow redistribution towards the leading edge side. At the trailing edge exits, the distortion of the flow path observed in the channel central portion causes a strong reduction in the dimensions of the 3D separation structures that surround the pedestals. Under rotation the turbulence promoters placed in the radial development region of the channel determine a strong flow redirection towards the leading side of the channel which suppresses the recirculation bubble observed in the smooth channel.

Acknowledgments

Three years are gone quick, but drawing up a list of the things I have learned from my advisor Prof. Luca Casarsa and my co-advisor, Alessandro Armellini, will take surely longer. Spending the most of my time by their side was wonderful and now I am glad I can call them friends. Moreover they gave me the opportunity to spend a lot of time in the vicinity of a 200, and more, rpm spinning channel, I think me and it are somehow friends too now. Then, I wish to thank Prof. Piero Pinamonti and Prof. Pietro Giannattasio for introducing me to the Ph.D. course. A special mention goes to Alessandro Zanon, I will never forget our constructive conversations as well as the walks in the mountains (perhaps one?). I have to be grateful for the help given in the data acquisition by Andrea Colombini and Matteo Pascotto. Special thanks go the laboratory technicians Mr.Franco Duca and Mr. Gilberto Forte. The present manuscript has gained quality and clearness from the useful observations made by the reviewers Prof. Giovanna Barigozzi and Filippo Coletti, I am glad they appreciate it. Thanks also to Giampi, for the London-English revision and to Giorgio and Giovanni for the colour printing.

Many friends contributed to my work, even they are not conscious, with laughs, and right words at the right time, both in Udine and at home. Thanks Flavio and Matteo for the walks in the mountains where my mind rests in peace. I will never forget the time spent with my team mate and room mate Federico, he has always been a good friend and fought with my disorder. If I am a better man, he helped to this. Basketball has always been an important part of my life, therefore I have to be grateful to all my team mates for bearing the researcher craziness and frustrations: some of them became close friends.

Then comes the people closer to my mind, my family, who supported my long educational trip: I will never forget how big this opportunity is. And Irene, who is always in my heart, even in the middle of laser shots, seeding clouds, or horse-shoe structures.

Finally, there is one thing I sometimes think at. My grandfather Corrado emigrated to Canada to ensure a better future to his family. After about fifty years I could get my Ph.D. degree. People should never forget the importance of the access to a formative, high quality, public, Instruction.

Contents

List of Figures

List of Tables

Preface

Energy and Power have always had a key role in human life. Even today, when the concept of Sustainable Development is becoming an obliged way for our society, we can't prescind from the concept of energy and its exploitation. Nowadays a large amount of the energy we use is produced by systems based upon turbo-machines. Among them, the gas turbine is surely the last delivered, but it was immediately clear that it was well suited for all of the applications where power/weight ratio is a strict requirement, even if its efficiency was considerably lower than other technologies. Nowadays, the developing of gas turbine engines with considerably higher efficiencies spread the range of their application from aircraft propulsion to land-base electricity production and ship propulsion.

1

Introduction

Gas turbines engines are used in many fields of engineering, ranging from land based power generation systems to aircraft propulsion. The research conducted on gas turbines over the past several decades lead to the design of engines able to operate at ever increasing temperatures with a consequent significant augmentation of performance. The improvements in turbine blade cooling techniques developed through research have been the major contribution to this.

Aircraft Gas Turbine Engines

The aircraft gas turbine engines can be of three different types: turbo-jet, turbo-fan (Fig. 1.1) and turbo-prop. The basic principle is the same for all of them: the net thrust

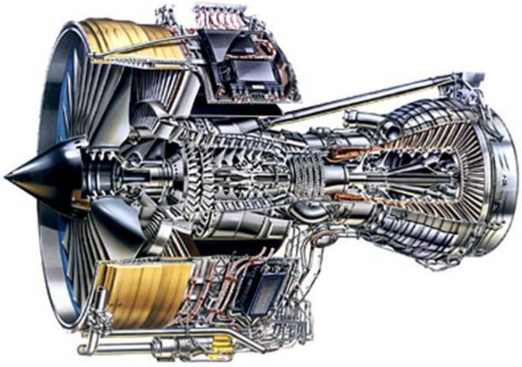

FIGURE 1.1 – The Rolls Royce Trent 900 aircraft engine.

to the aircraft is given by an increase of the momentum of the working fluid (air and burnt gases) leaving the system. In the case of the turbo-jet, this is achieved by a strong increase of the burnt gases velocity. On the contrary, the other two types operate with a small velocity increase of a large amount of air mass and only a part of the air flowing into the engine is involved in the thermodynamic cycle. The ratio between the mass flow rate of air drawn in by the fan and by-passing the engine core to the mass flow rate passing through the engine core is the $by-pass\ ratio$.

Anyhow the thrust is delivered, the gas turbine engines realise a Brayton-Joule cycle (Fig. 1.1). After the intake, the *compressor* increases the pressure and the temperature of the air before entering in the *combustion chamber* where the fuel is burnt, yielding to a strong augmentation of the gas temperatures (from 1100K to even 1800K). The ratio of the outlet to inlet pressure at the compressor is denoted as the *compression ratio* β. Then the burnt gases expand in the *turbine*, which produce a net shaft power to drive the compressor, if the engine is a turbo-jet or both the compressor and the fan (propeller) if it is a turbo-fan (turbo-prop) .

Aero-derivative gas turbine engines (Fig. 1.2) are obtained by simply replacing the fan with a mechanical load if the aircraft engine has a low by-pass ratio (≈ 2) or installing a power turbine if the by pass ratio is higher. Commonly, regardless of what the solution adopted is, the compression ratio is reduced, to allow a longer life-cycle and maintenance intervals. These power generation units are becoming widespread in land based applications and ship propulsion thanks to their ever increasing efficiency, reliability, and power-to-weight ratio.

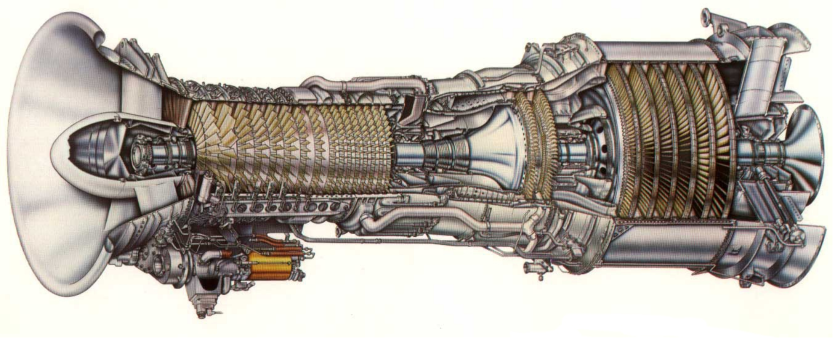

FIGURE 1.2 – The General Electric LM2500 Gas Turbine

Gas turbine efficiency

Figure 1.3 shows the cycle efficiency for different Turbine Inlet Temperatures (TIT) and compression ratios. The data show that an increase of the efficiency can be obtained either by increasing the compression ratio or either by increasing the TIT for a fixed β. An increase of β can be achieved with an higher aerodynamic load of the blades, but this usually comprises a decrease of the aerodynamic efficiency.

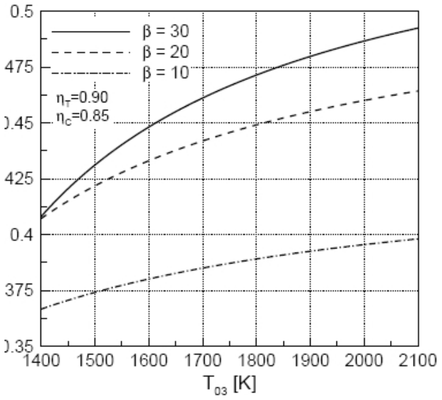

FIGURE 1.3 – Cycle efficiency of a Brayton-Joule cycle from [1]

Moreover, compressor blades must be carefully loaded to avoid blade stall. However, higher compression ratios can be achieved by inter refrigerated compressors at the cost of an increased size and weight.

In contrast an increase of the TIT requires the adoption of materials with high thermal resistance to realise the blades, which have to sustain temperatures that nowadays reach 1800K in the first two stages of a modern high pressure turbines, as well as high mechanical and thermal stresses. These requirements compel to the usage of a limited number of materials that can withstand these working conditions. Nickel based wrought and cast alloys were firstly used to manufacture blades with high resistance to thermal fatigue and to oxidation. Then, to obtain a higher resistance to creep and heat single crystal or directionally solidified blade manufacturing processes were developed.

At the present time, a melting point as high as 1300 K is achieved by employing of oxide-dispersion strengthened alloys and, where possible, ceramic thermal barrier coatings(Fig. 1.4). However, it is a matter of fact that the development of new and more resistant materials is not sufficient to guarantee the performances achieved by the aircraft turbine engines nowadays.

Thus blade cooling has become soon strictly necessary to allow the blades to withstand the severe working conditions they are exposed at. An efficient blade cooling system must keep the blade material temperature below its melting point without affecting the mechanical strength of the blade itself. However, it has to be noticed that only the first HP turbine stages require a cooling system, afterwards the energy conversion process yields to flow temperatures low enough to be withstand by un-cooled blades.

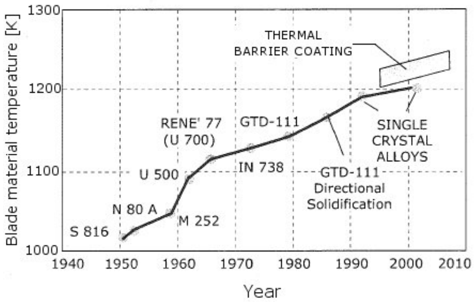

FIGURE 1.4 – Maximum temperatures allowed by blade material since 1940 [1].

Blade Cooling

The working principle is to use the feeding air coming from the compressor to cool the blades with an open fluid circuit. Nowadays, the as much as the 20 % of the mass flow rate delivered by the compressor can be used for this purpose. Three different cooling schemes have been introduced up to now :

- forced convection internal cooling (Fig. 1.5(a,b));
- film cooling (Fig. 1.5(c,d));
- transpiration cooling (Fig. 1.5(e)).

Internal Forced Convection Cooling

The forced convection cooling is obtained by realising ducts inside the blade during the casting process. The cooling channels can have different shapes (square cross-section, triangular...) and layouts (single pass, double pass) depending on which part of the blade they are designed for.

Furthermore they are often provided with turbulence promoters in order to improve the heat transfer rate as shown in Fig. 1.5 (a) . *Riblets* cause a periodic boundary layer tripping while *pin-fins* generate horse shoe vortices, thus enhancing the Heat transfer. It has to be noticed that the introduction of turbulence promoters increases also the total surface area involved in the heat exchange process.

A variation of convection cooling, *impingement cooling*, Fig. 1.5 (b), works by hitting the inner surface of the blade with high velocity air jets. This allows more heat to be transferred by convection than regular convection cooling does. Impingement cooling is often used on certain areas of a turbine blade, like the leading edge, while standard convection cooling used in the rest of the blade. The drawback is that the (Heat Transfer Coefficient) HTC distribution can be strongly non-uniform, therefore introducing significant thermal stresses in the blade as stated by Bunker in [22].

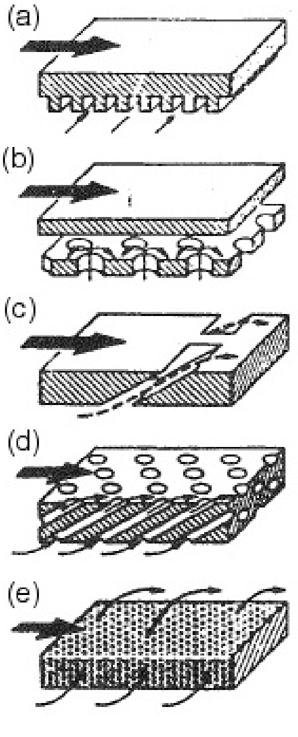

Figure 1.5 – Cooling schemes: (a) forced convection, (b) impingement, (c), (d) film, (e) transpiration from [1].

Film Cooling

Film cooling technology aims at obtaining a thermal barrier outside the blades by means of a film of coolant. The air coming from the compressor is convected inside the blade and then exhausted outside in the mean flow by a large number of small holes, thus creating a thin layer of fresh fluid near the blade wall. If the holes are properly positioned and shaped, and if the *bleed ratio* is correct, a maximum cooling effectiveness is achieved without compromising the aerodynamic efficiency of the blade profile. By contrast if the coolant ejection causes the free-stream boundary layer separation, the aerodynamic performance of the blade might be strongly penalised. Nowadays, in the top performance turbo gas engines film cooling is widely used to cool the blades as well as the end-walls.

Transpiration Cooling

Transpiration cooling is similar to film cooling in that it creates a thin film of cooling air on the blade outer surface, but, in this case, fresh air is leaked through a porous shell which surrounds the blade rigid body. The pore diameter is very small, typically from 10 to 50 *microns*, and therefore occlusion can occur due to dust or carbon residuals from the combustion process. It is a matter of fact that the cooling effectiveness achievable with this technique can reduce progressively during the operational life of the engine. Another problem is represented by the increased roughness of the blade surface, which determines higher skin-friction losses.

In modern applications, all of the aforementioned techniques are used simultaneously, with exception of the latter, to cool the blades. This is an obliged rather than a free choice in view of the higher and higher performances requested from the cooling schemes. HTC augmentation factors relative to smooth surface heat transfer coefficients of as much as 4, with even higher magnitudes possible under certain rotational conditions are nowadays commonly achieved. However, further increases in heat transfer coefficient magnitudes may be desirable, but these increases typically also come with an undesirable augmentation of the material thermal gradients [22]. Therefore, the peak magnitude of heat transfer coefficient is no longer so important as the gradients in coefficient and material temperature. Higher gradients lead to stress and strain barriers, either steady or cyclic, as well as greater levels of thermodynamic un-mixedness or inefficiencies. All these complexities strongly require a detailed knowledge about the involved flow features to understand the heat-transfer mechanisms and to guide the design process.

Trailing edge blade cooling

One of the most challenging issues is to guarantee adequate thermal protection to the TE region when the blade profile thickness is strongly reduced. Thin blade profiles allow an

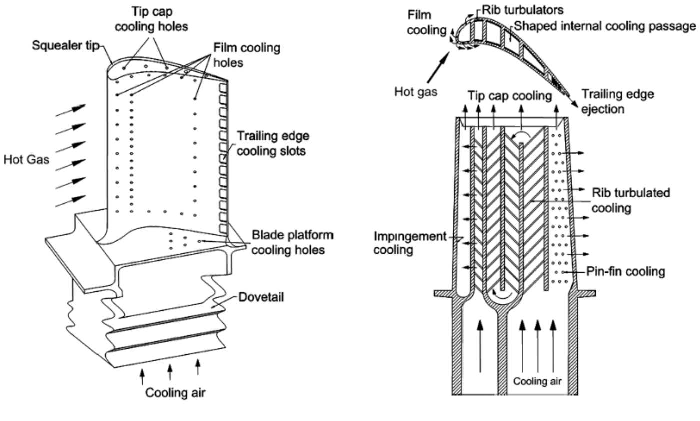

Figure 1.6 – Cooling system of a modern blade, from Han [2].

higher profile efficiency and load but introduce severe constraints to the cooling design. Therefore the internal cooling channels size and shape are different with respect to those used to cool the LE or the central body of the blade (Fig. 1.6). TE channels have an high aspect ratio, to accommodate inside the elongated profile. Sometimes the cavities are wedge shaped in the TE region, to fit in the blade profile. Turbulence promoters can be used as well, in particular elongated pin fins named *pedestals* are often employed to ensure mechanical strength and enhance the heat transfer process. The flow scheme is usually single pass, in fact, the coolant is commonly discharged by rectangular openings (*slots*) all along the blade trailing edge in the main flow expanding in the turbine.

When the blade thickness is further reduced on cutting material from the blade profile can be a solution to ensure thermal protection by a shield of coolant that protects the thin TE (Fig. 1.6).This solution requires even more care when designing the TE internal channel, in order to avoid unevenness of the coolant flow at the cut-back that can seriously affect the aerodynamic performance of the blade.

I

Background of the present work

2

A brief survey of the open literature

When looking at the available literature, it is possible to realise that the majority of the studies deal with cooling schemes normally used for blades central body, i.e. square or rectangular rib-roughened channels, in which the coolant flows along the main blade axis (i.e along the radial direction), eventually in multiple passages configurations.

Unfortunately, TE cooling channels have specific features and the knowledge gained on passages for the blade central body or the leading edge cannot be easily applied, thus specific investigations must be performed on the TE ducts.

2.1 Literature Review

2.1.1 Stationary channels

If looking at the open literature, a good point to start is represented by the work of Taslim et al. [3] for a channel with axial outflow. In the geometry analysed by Taslim, cooling air from an adjacent passage was impinged on a rib-roughened surface at the PS or at the SS via a series of race-track shape openings and than discharged at the blade trailing edge. A schematic of this cooling design is reported in Fig. 2.1. The Liquid Crystal Thermography (LCT) was used to study the effects of jet impingement on a rib-roughened surface. The experiments were performed for Reynolds Numbers ranging from 30000 to 50000. For what concerns the results, firstly, the rib-roughened channel showed a significant global HTC augmentation with respect to the baseline smooth case. Beside analysing the effects of different rib arrangements and height, the race-track shape openings were than tilted such in a way that the flow impinged on the test section wall in the vicinity of the rib root with more scrubbing action against the test section ribbed wall. Furthermore, it was proven that the rib arrangement is crucial to maximise the effects of impingement cooling, which benefits also extend to the opposite internal surface of the duct. More recently this author presented a numerical investigation on a similar geometry [23] concerning the optimum arrangement of crossover jets.

A complete experimental and numerical analysis of a channel geometry similar to

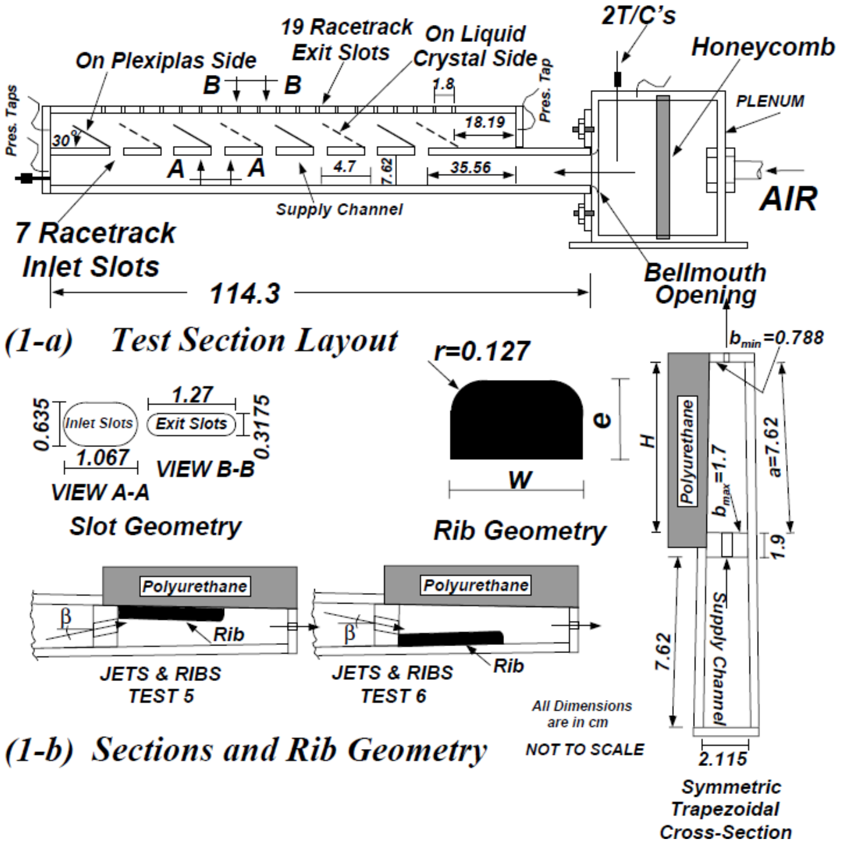

FIGURE 2.1 – Schematic of the test section from Taslim et al. [3].

the one in [3] was performed by Armellini et al. [4] and Coletti et al. [5] (Fig. 2.2). The 2-Dimensional Particle Image Velocimetry (2D-PIV) measurements provided a deep insight on the flow, which allowed a full comprehension of the thermal behaviour of the investigated geometry. In this case, the mid-wall slots had axes sloped down with an angle close to 30° with respect to the horizontal direction, in such a way that jets impinged on the bottom wall of the trailing edge cavity. Beside the smooth case, a rib-roughened configuration was investigated which was characterised by the adoption of squared cross-sectional *riblets* at the bottom wall angled at 30 °. The experiments were performed for a fixed Re equal to 67500 defined at the inlet section of the model. Preliminary surface flow visualisations performed without riblets depicted the flow impingement caused by the tilted jets, and the jet rebound towards the opposite wall due to the interaction of two consecutive impingements which determined a considerable scrubbing action on both the channel walls. A third impingement zone was found in-between the exit slots.
When the riblets were placed into the channel substantial modifications in the flow field were observed. The flow inside the cavity turned out to be driven by inclined crossing-jets originating from the mid-wall, causing a remarkable unbalancing within the jets. However, each crossing-jet could still penetrate inside the cavity up to the end of the

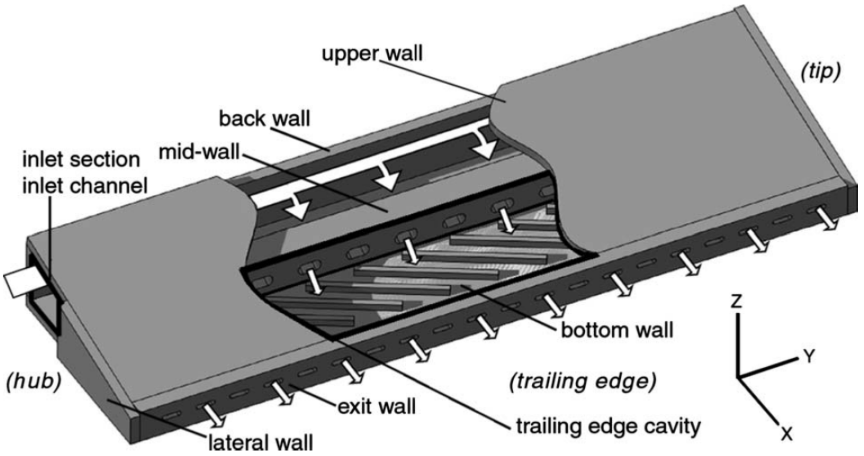

FIGURE 2.2 – Overview of the test section from Armellini et al. [4] and Coletti et al. [5]

ribbed part, producing three different impingements on the three turbulators in front of the slot. After the first and second impingements the coolant was redirected by the riblet along its length, and in view of the blockage caused by the adjacent on it was then forced to separated and deflected towards the opposite wall (Fig. 2.3, left), thus establishing two vertical structures. Armellini et al. showed that the first one impinged on the upper wall in the region between two slots and that in the corner between the mid and the upper walls the flow a recirculation region was established. At the same time the second up-ward structure produced another periodical impingement in between two slots approximately at the centre of the upper wall then, from this point, the flow spread in all directions. Two separation lines were found at the upper wall as a consequence of the interaction between consecutive impingements (Fig. 2.3 right). The thermal measurements showed the great

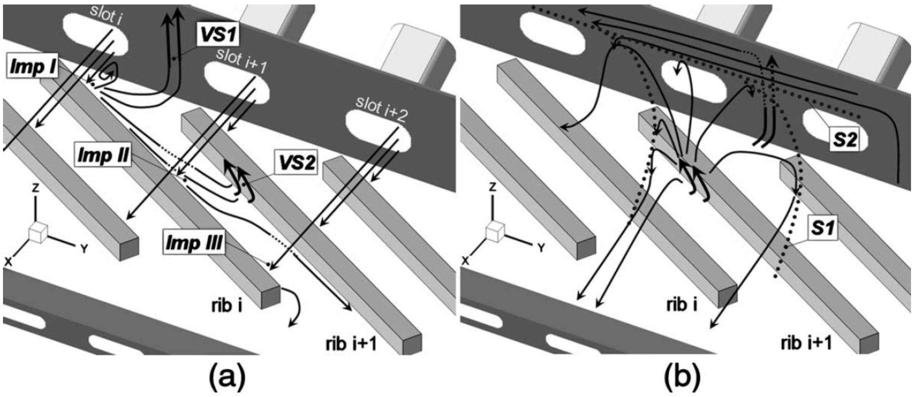

FIGURE 2.3 – Summary of the mean flow path model: (a): inter-rib region and vertical structures and (b): flow structures near to the upper wall (from Coletti et al. [5]).

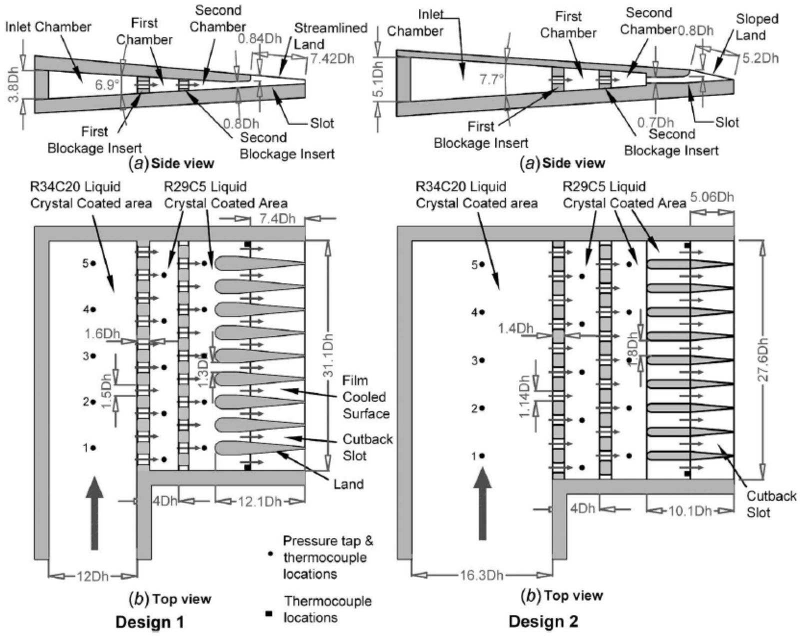

FIGURE 2.4 – Schematic of the test section designs investigated by Choi et al. [6].

impact of this complex flow field on the HTC distribution, on both the channel sides. Indeed the maximum Nu values were found in the impingement regions while the lowest in the recirculation region in the corner between mid-wall and upper wall. It was also proven that the turbulators concur to extend the positive effect of the impingements, by breaking and deflecting the jets. Indeed the ribs insertion was responsible for an average heat transfer enhancement of 25 % on the bottom wall and of 16% on the upper one. Furthermore in these works, the detailed aero-thermal analysis pointed out the limits of the numerical solver in predicting the very complex flow field that develops inside the channel. These works have been extended further on by the conjugate heat transfer measurements reported in Coletti et al. [24].

A TE channel geometry provided with coolant ejection through slots and lands has been investigated in the experimental work of Choi et al. [6]. In this work, the coolant enters in a radial channel of constant cross section and is forced through a 90° bend before to enter two rows of perforated blockage inserts used to generate flow impingement on the channel walls (Fig. 2.4). Finally, the coolant is discharged outside through a wedge-shaped TE section. The thermal field was measured by means of liquid crystal thermography at varying Reynolds number from 5000 to 30000 and blockage configuration. Beside valuable information about the effect of different geometries and working conditions on the heat transfer performance, their data show also a not uniform distribution of the heat transfer coefficient along the radial direction. The cause of this behaviour may be probably found in the design of the passage entrance, which configuration deter-

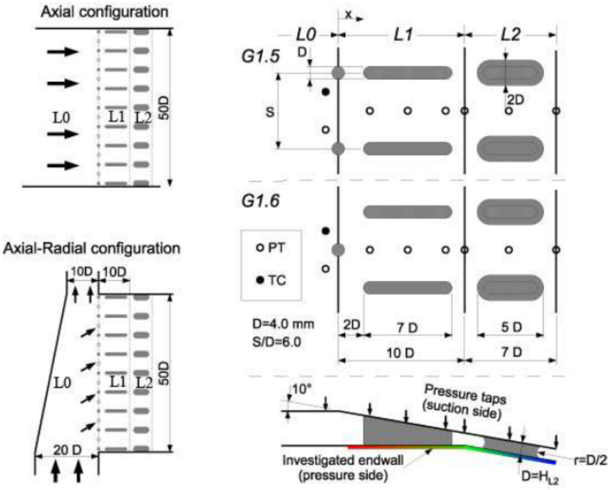

FIGURE 2.5 – Schematic of the test section designs investigated by Facchini et al. [7].

mines an uneven flow velocity distribution along the TE. A detailed flow field analysis would be useful to confirm these results.

All the works mentioned regard geometries with multiple cavities and where impingement cooling is often used to increase the heat transfer rate, however recently a certain interest in single pass schemes has growth as well. As an example, Facchini et al. [7] made use of a flow redirecting wall at the channel leading side, coupled with coolant purging at the blade tip in an attempt to provide a quasi-uniform flow along the TE exit of their wedge-shaped channel (Fig. 2.5). HTC distributions obtained by liquid crystal thermography are reported for channel configurations characterised by different turbulence promoters (pin fins and oblong pin-fins called pedestals) installed along the TE and for an outlet tip mass flow rate ranging from 0 (pure axial flow) to 25 % (axial-radial) of the inlet mass flow. The test were performed for Reynolds Number ranging from 9000 to 27000. The results are compared with those obtained for a channel without inlet turning flow, i.e. with an axial flow at the inlet of the trailing edge test section. It was proven that the axial-radial configuration determines an uneven HTC distribution between the obstacles, as a consequence of the non-zero angle of attack of the flow. The increase of the tip outlet flow rate turns in a higher radial velocity, and therefore enhances the asymmetrical Nu distribution. More in detail, the HTC peak at the leading edge of the first two rows of obstacles was addressed to the presence of horse-shoe vortices developing from the stagnation point. By contrast, on the downwind side, the coolant separates from the surface and recirculates with local low HTC values. In the region upstream of the TE exit, a quasi-uniform heat transfer field was found in particular when the 25% of the coolant is discharged at the tip. This region is weakly affected by the obstacle configuration or by the flow scheme. Concerning the channel friction factor, it was shown that this latter decreases for an increasing mass flow rate discharged at the tip.

At this point an issue regarding the experimental and the numerical methodologies has

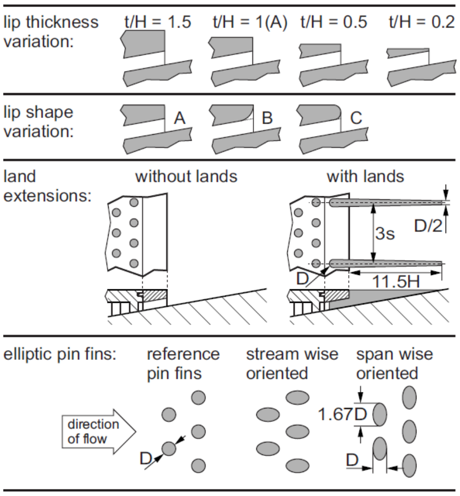

FIGURE 2.6 – Geometric variations investigated by Horbach et al. [8]

to be discussed. The key issue to provide useful information by means of laboratory scaled test models is to fulfil the flow similarity parameters, namely the Reynolds Number which ranges from 20k to 60k in real engines. If conjugate HTC measurements are performed even the solid-to-fluid thermal conductivity ratio has to be matched as in [24]. In the case of TE passages, it has to be noted that a perfect match with the engine conditions should take into account also for the pressure distribution found along the radial direction at the blade TE. Furthermore, the pressure radial distribution is far to be constant and depends upon the airfoil design [25]. However, in all the aforementioned contributions a constant pressure condition was imposed along the TE exit. This choice can be surely justified by the need to use simple and replicable conditions, but no mention is made about this point by all the cited authors.

Shifting the attention back to the open literature, beside the investigations conducted inside the ducts, a significant research activity was devoted to investigate the impact of the channel internal features on the external flow field, since the presence of TE outlets is always used in the TE ducts. Rehder et al. [26] provided an assessment of the profile aerodynamic losses yielded by a single cavity duct with three different discharge sections: with central trailing edge ejection, with pressure side cut-back & slot and with pressure side film holes. The analysis was performed in a wind tunnel for linear cascades with main stream velocities up to a Mach number at the blade outlet equal to 1.2 and by means of standard aerodynamic measurement techniques (blade surface static pressure measurements, wake traverses) and schlieren optical visualisation.

Horbach et al. [8], investigated the film cooling effectiveness of different internal pin-fins configurations at varying the blowing ratio the lip thickness to ejection slot height ratio and considering the effects of typical manufacturing imperfections and wear, Fig. 2.6. The infra-red thermographic measurement technique was employed, allowing to show a strong dependency on ejection lip thickness, and that significant improvements

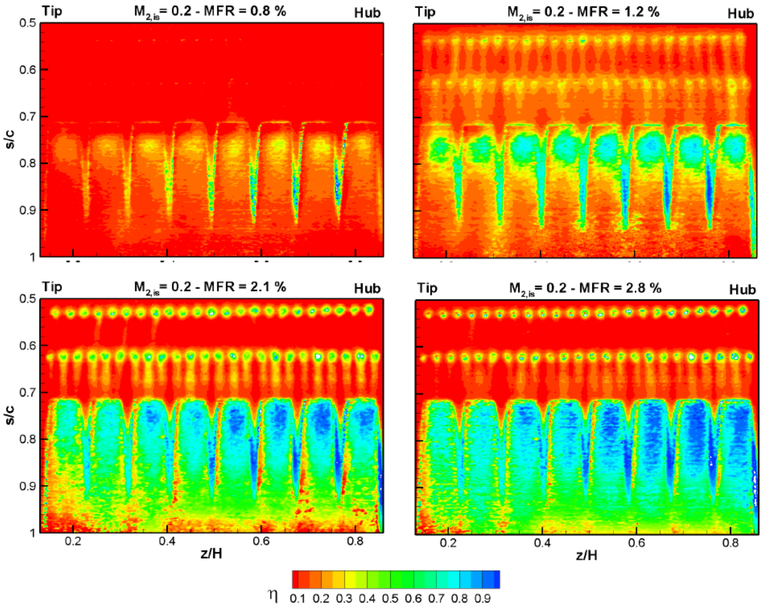

FIGURE 2.7 – Adiabatic effectiveness for η for $M_{2is} = 0.2$ at different coolant injection rates (MFR) values, from Barigozzi et al. [9]

are achieved using land extensions.

A thermal analysis of film cooling effectiveness where an internal channel resembling that of [27] and [7] coupled with cut-back openings can be found in the work of Barigozzi et al. [9]. This latter reports an analysis of the thermal field developing at the TE in a real first stage nozzle vane profile, shown in Fig. 2.7. The tests, performed in an high speed wind tunnel for linear cascades, allow to take into account even for the compressibility effects. Concerning the results reported, leaving aside valuable information on the film cooling effectiveness at varying the blowing ratio, and focusing on the internal channel, this latter may be the responsible for the non uniform cooling effectiveness distribution due to an uneven feeding of the cut-back openings and film cooling holes.

2.1.2 Rotating ducts

If rotor blade cooling channels are considered, the rotational effects on the fluid flow and on the heat transfer distribution must be taken into account as well. These latter are namely the Coriolis effects and the Centrifugal force. If the flow is isothermal with the channel walls, the centrifugal force acts as a positive pressure gradient in the radial direction, but in the case of non-isothermal conditions, as in internal cooling ducts, a rotational buoyancy effect rises. Thus the flow field, and in turn the thermal field, can be substantially modified by rotation, therefore pushing the researchers to gain a detailed knowledge on the relative flow field behaviour. In the following the TE cooling applications are leaved aside for a while to give a more general point of view about the

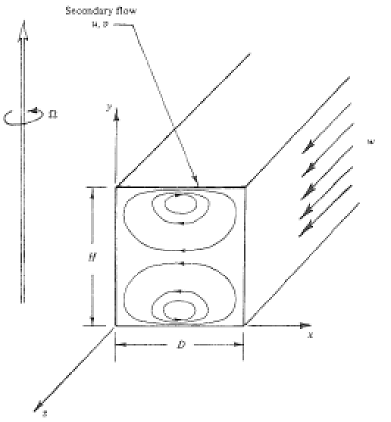

FIGURE 2.8 – Secondary flow in a rotating rectangular channel.

investigations on the flow field under rotation.

The stabilisation (de-stabilisation) and de-stabilisation (stabilisation) of an outward (inward) flow at the trailing or leading side of the channel and the development of counter rotating vortices in square or rectangular channels in both laminar and turbulent regimes is well documented in [12, 28, 29, 10, 30] in the case of orthogonal rotation.

In orthogonally rotating ducts with flow in the outward (radial) direction, the span-wise Coriolis component $Fc_y = 2\omega U$, (Fig. 2.9(a)) is balanced by a wall normal pressure gradient which is negative from the trailing side to the leading side of the channel. Since the Coriolis acceleration is $F_C = -2\vec{\omega} \times \vec{(C)}$, where $\vec{\omega}$ is the angular velocity and $\vec{C}$ the relative flow velocity, it is clear that F_C is maximum in the core flow and minimum in the boundary layers. This unbalancing is the trigger for the developing of the secondary, counter rotating structures, shown in Fig. 2.8.

As a consequence, in a fully developed flow[1] the resulting velocity profile in the plane orthogonal to the axis of rotation will show a maxima displaced towards the trailing side

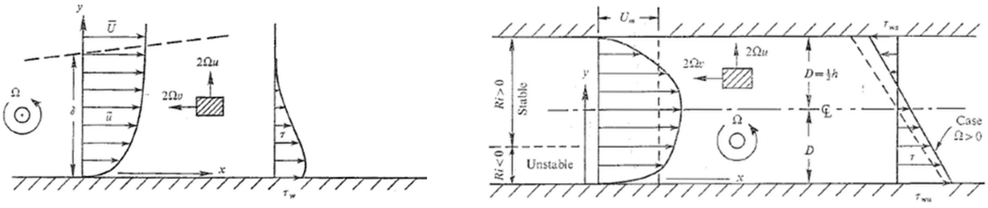

(a) Turbulent boundary layer [10].
(b) Mean velocity profile under rotation [10].

FIGURE 2.9 – Schematic of the effects of the span-wise Coriolis component ($Fc_y = 2\omega U$) on an outward flow in an orthogonally rotating radial duct, from Johnston et al. [10]

---

[1] i.e. irrotational with respect to the relative reference frame.

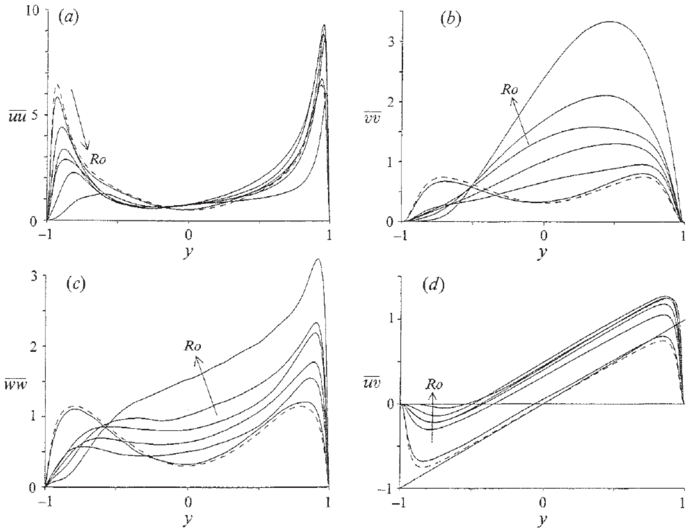

FIGURE 2.10 – Reynolds stress components in global coordinates from Kristoffersen et al. [11]. Dashed lines represent the static case, -1=leading side, 1=trailing side.

of the channel as shown in Fig. 2.9(b), for flow in the outward direction, or towards the leading side for an inward one.

The second effect of the span-wise component of the Coriolis acceleration is related to the effects on the turbulence levels. If the ratio of the back-ground vorticity to the vorticity associated to the boundary layer ($S = -2\omega / (\partial \bar{u} / \partial y)$) is greater than zero a stabilising effect, i.e. a decrease of the turbulent levels, occurs. By contrast, if $S < 0$ the turbulent activity is enhanced, as reported by the DNS performed by Kristoffersen et al. [11], Fig. 2.10.

Furthermore, different flow regimes, shown in Fig. 2.11, were identified at increasing the rotation rate. At weak rotation rates, the axial velocity profile along the direction of

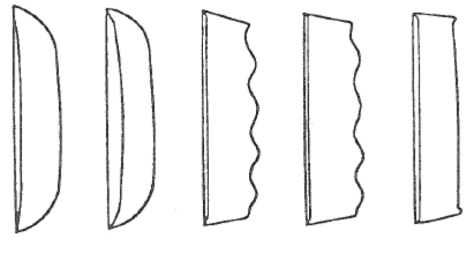

FIGURE 2.11 – Experimental stream-wise velocity profiles along the direction of the axis of rotation for a laminar flow [12] at increasing the rotation rate. (a) Static case, (b) with Coriolis induced counter rotating structures, (c,d) with multiple roll cells, (e) Taylor-Proudman regime from hart et al. [12].

rotation is quasi-parabolic and a double-vortex structure appears near the shortest walls of the duct. At intermediate rotation rates, an instability in the form of longitudinal roll cells was observed in [12, 28, 29]. In this case, the profile of the stream-wise velocity was distorted with a wavy structure by the presence of the rolls. At more rapid rotation rates, the re-stabilization of the flow to a Taylor-Proudman regime occurred i.e., the axial velocity does not vary along the direction of the axis of rotation. The roll cells disappear, and a stretched double-vortex secondary flow appears which is quite similar to the one previous to the onset of instability. This last effect is related to the radial (stream-wise) component $Fc_x = -2\omega V$ (Fig. 2.9(a)) of the Coriolis force as shown in the Appendix B.

Shifting back to the literature, Moore [31] presented one of the first experimental contributions on the Coriolis effect on the flow field from a turbo-machinery application perspective, while, more recently, Pallares et al [13] provided a meaningful analysis of Coriolis effects in a square channel by means of Large Eddy Simulations (LES). This latter work showed that the effect of low rotation rates in the square duct flow produce substantial changes in the turbulence-driven secondary flows developed near the corners, as depicted in Fig. 2.12. The Coriolis-generated velocity redistribution in the central part of the duct toward the trailing side enhances the stream-wise vorticity and the secondary flows, which convect this current toward the leading side, near the side walls, and than towards the central part of the duct. At moderate rotation rates, the cross-stream flow field consists of two large and two small counter-rotating cells. The large cells convect low momentum fluid from the stable side to the unstable side across the central part of the duct. This convective transport displaces the maxima of the radial velocity component towards the side walls and towards the unstable wall as the rotation rate is increased. Turbulence-driven secondary flows at moderate and high rotation rates occur on the unstable side below the corner bisectors. It has been found that, at moderate rotation rates, the stream-wise vorticity of these small secondary flows is increased by the presence of the stream-wise velocity maxima near the corners. At the highest rotation rate considered, the turbulence level on the stable side is considerably reduced owing to the stabilization of the flow to a Taylor-Proudman regime. This flow structure, which is characterized by the absence of stream-wise vorticity in the central part of the duct, is

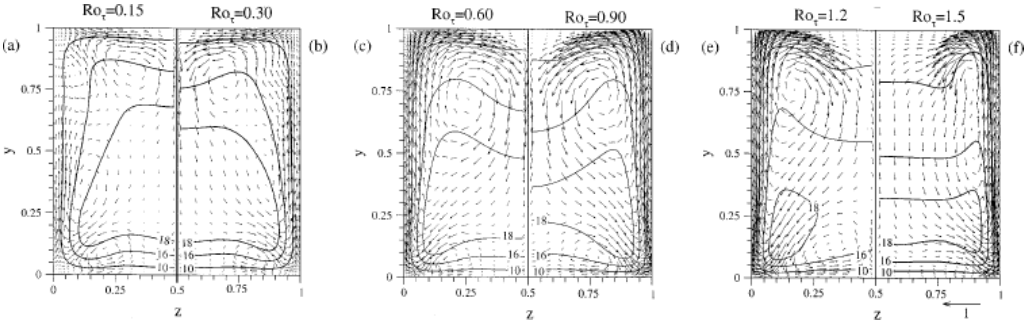

FIGURE 2.12 – Secondary structures in a square channel at increasing the rotation rate, from Pallares et al. [13]

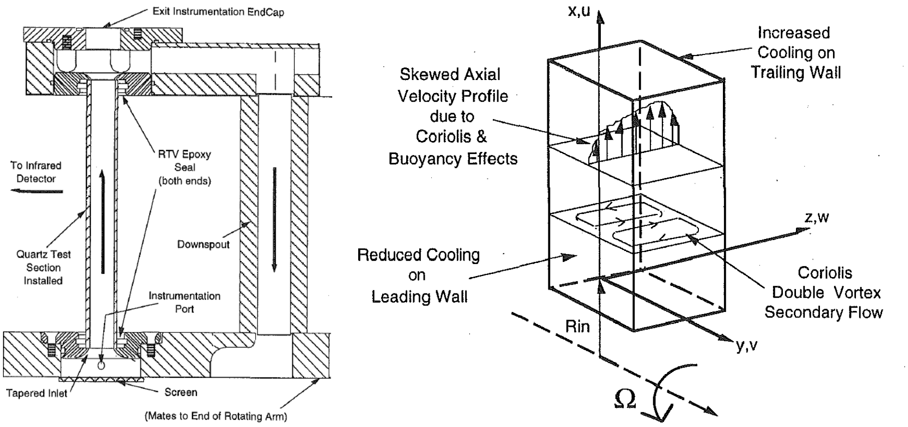

(a) Test section from Bons et al. [32]

(b) Flow model proposed by Bons for a rotating heated square duct.

FIGURE 2.13

produced by the intensification of the Coriolis-generated vertical stream-wise momentum convective transport.

Bons et al. [32] provided a simple numerical model of Coriolis and buoyancy effects on the outward flow field inside a rotating square duct presented in Fig. 2.13(a) The model turned out to compare fairly good with the experimental data obtained by 2D-PIV (Fig. 2.14) and Nusselt Number (Nu) distributions obtained by means of infra-red temperature measurements.

Thanks to the availability of flow and thermal field measurements, Bons showed that

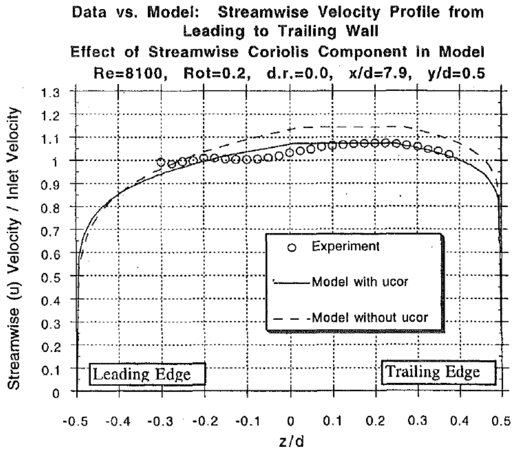

FIGURE 2.14 – Bons data versus model prediction of stream-wise velocity profiles with Ro= 0.2

the secondary flows induced by the Coriolis effect determine a decrease of the HTC performance of the ducts at the LE with respect to the stationary case. On the opposite, the heat transfer mechanism is enhanced on the TE wall of a smooth channel.

Coletti et al. [14] made use of the rotating facility developed by Di Sante et al. [33] to discuss in detail the flow-field behaviour of a square ribbed channel by means of PIV measurements in the wall-normal/stream-wise planes. The stabilizing and de-stabilizing effects showed a great impact on the boundary layer tripping and re-attachment induced by the riblets and on the release of the coherent structures at the ribs lip as a sketched in Fig. 2.15(a). Indeed, as shown in Fig. 2.15(b), if the rotation is stabilising with respect to the rib-roughened wall, the reattachment point is closed to the rib lip than in the static case, otherwise, it moves further in the destabilising case. At the same time the stream-wise turbulence intensity can be decreased or enhanced if the rotation is stabilising or de-stabilising Fig. 2.15(c).

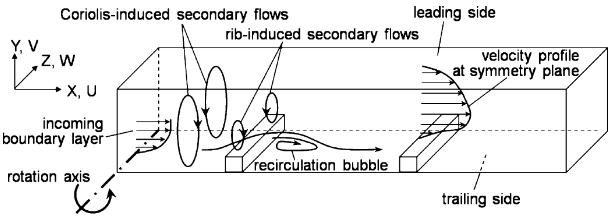

(a) Rib-flow model with rotation.

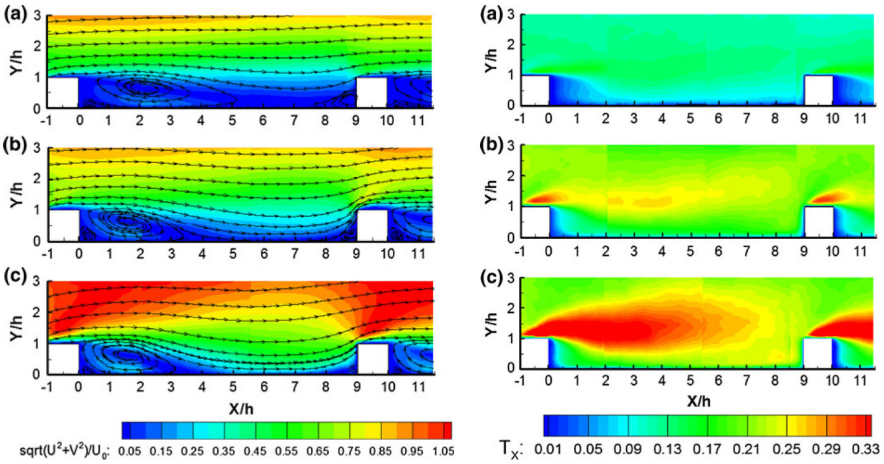

(b) Two-dimensional streamlines and contours of mean in-plane velocity: stabilizing rotation (a), non-rotating case (b) and destabilizing rotation (c).

(c) Contours of turbulence intensity along the radial-direction (x): stabilizing rotation (a), non-rotating case (b), and destabilizing rotation (c).

FIGURE 2.15 – Effect of rotation on the flow filed in a rib-roughened channel, from Coletti et al. [14].

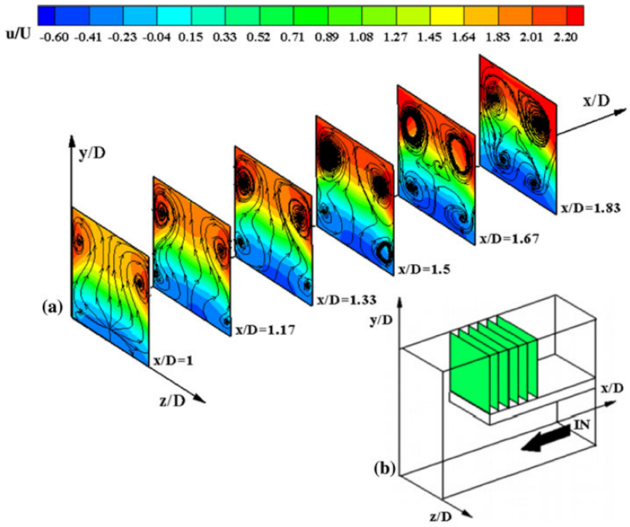

FIGURE 2.16 – Secondary structures in rotating "U" turn duct, from Gallo et al. [15].

In the case of two pass internal ducts the two passages are connected by means of a "U" turn. This latter, in the case of a stationary channel, induces the formation of secondary flows known as Dean vortices. If rotational effects are considered as well, a complex turbulent flow is promoted as shown by Gallo et al. [15]. These authors provided an exhaustive 3D reconstruction of the flow field inside the turn by means of 2D-PIV measurements across multiple cross-wise planes.

Another example of 2D-PIV investigations on a two pass rib-roughened square channel (Fig. 2.17(a)), or on a two pass leading edge (Fig. 2.17(b)) cooling channel in isothermal

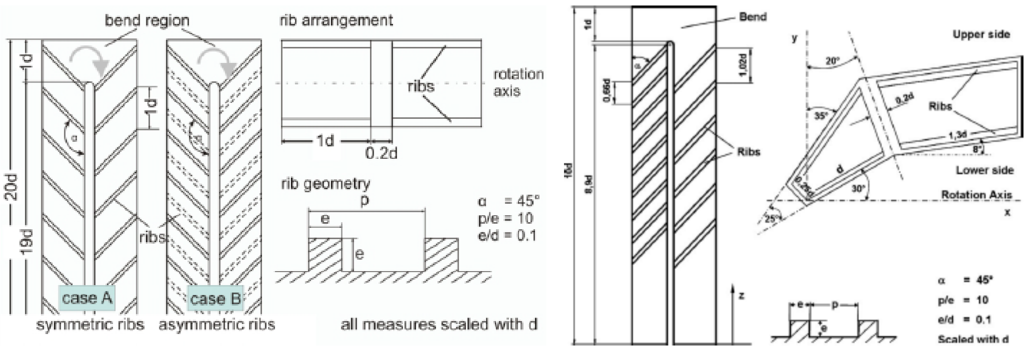

(a) Two pass square channel with angled ribs from ([34])

(b) Two pass leading edge channel with angled ribs from ([35]).

FIGURE 2.17 – Geometries investigated in the works of Elfert et al..

conditions subjected to orthogonal rotation can be found in the works of Elfert et al. [34] and [35], who also provided numerical simulations concerning the latter work in [36]. The measurements were performed with a fixed PIV chain, as done by Bons et al. and in contrast to the work of Coletti et al. [14]. In [34] the author has undergone trough serious problems in synchronizing the 2D-PIV chain with the channel motion, which limited the result accuracy. However an improved test rig allowed to acquire high resolution measurements, reported in [35], which will support the undergoing thermal analysis.

Iacovides et al. [16] performed LDA measurements on the flow field inside a two pass rib-roughened square channel depicting the mass flow redistribution due to secondary Coriolis structures and the turn effects, reported in Fig. 2.18.

All the aforementioned works represent the majority of the flow field investigations inside rotating ducts. In contrast thermal analysis on various geometries, single or multiple pass ducts with various aspect ratios and channel orientations with respect to the axis of rotation are widely diffused. Usually the experimental methodology comprises thermocouples or heat and mass measurements. Beside a Number of these works provide ready-to-use correlations, it should be noted that the flow patterns hypothesised by the

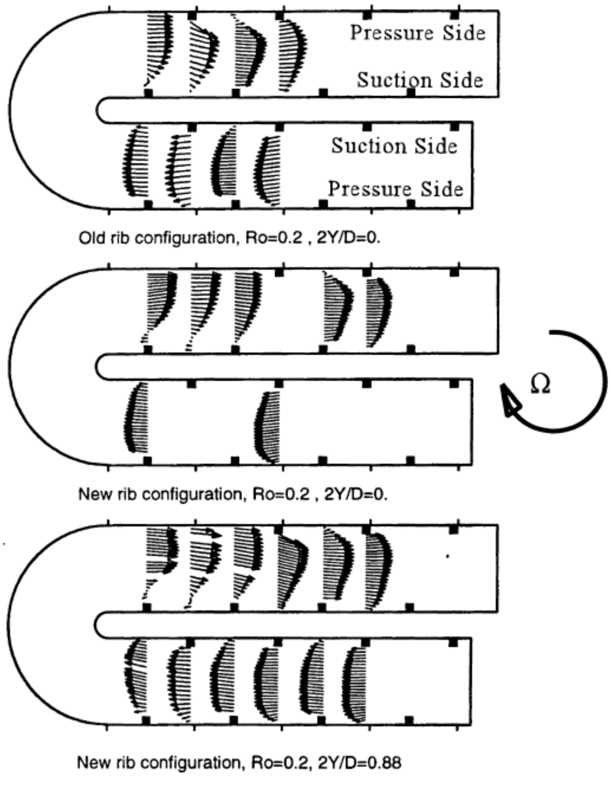

FIGURE 2.18 – Stream-wise velocity profiles along the span-wise direction from Iavocides et al. [16]

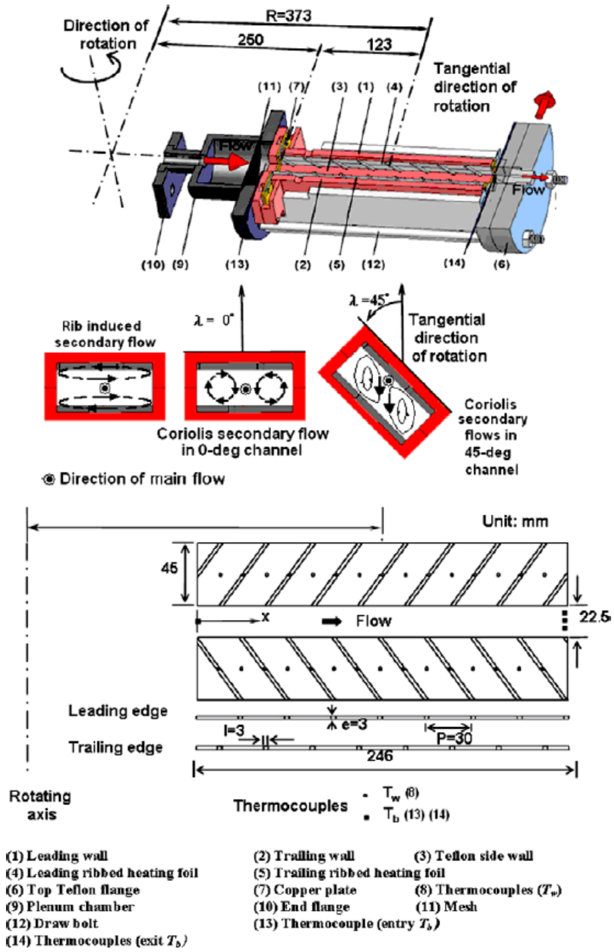

FIGURE 2.19 – Heat transfer test module and conceptual secondary flow patterns, from Liou et al. [17].

researches to justify heat transfer performances of models with complex geometries under rotation need an experimental confirmation.

A detailed experimental thermal analysis in a two-pass rotating ribbed duct can be found in the work of Chang et al. [37]. They show the influences of Reynolds, Rotation and Buoyancy Numbers on the local heat transfer.

On a similar geometry, Fig. 2.19, Liou et al. [17] investigated the effects of different channel orientations: the most uneven distribution between LE and TE side of the channel was found in the case of orthogonal rotation.

An attempt to simulate the effects of different entrance geometries, resembling the ones that can be found in real engines, is constituted by the work of Wright et al. [18]. Their investigation was focused on inlet conditions such as: fully developed flow, sudden

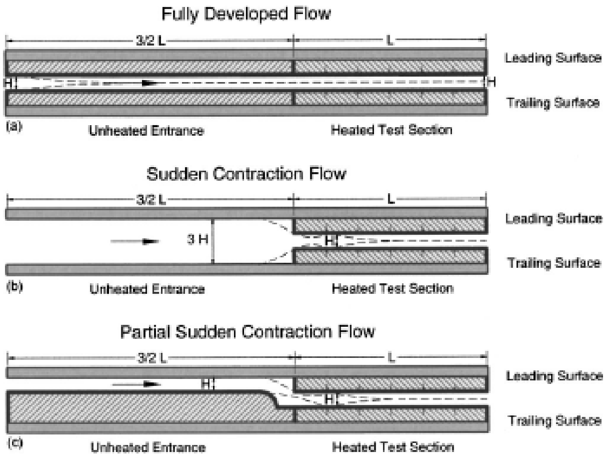

FIGURE 2.20 – Cross-sectional view of the various entrance configurations investigated in Wrigth et al. [18].

contraction, and partial sudden contraction, Fig. 2.20. The results showed that the influence of the inlet shape on the cooling performance is decreased by rotation. An high aspect ratio (AR= 10) cooling channel thermal performance was depicted by Willet et al [38] showing significant differences on the thermal field with respect to a square cross section duct.

Recently, a complete thermal analysis of a blade cooling system was achieved taking into account the different cooling schemes employed at the blade leading edge ([39]), central body ([40, 41]) and trailing edge ([19], Fig. 2.21) regions.

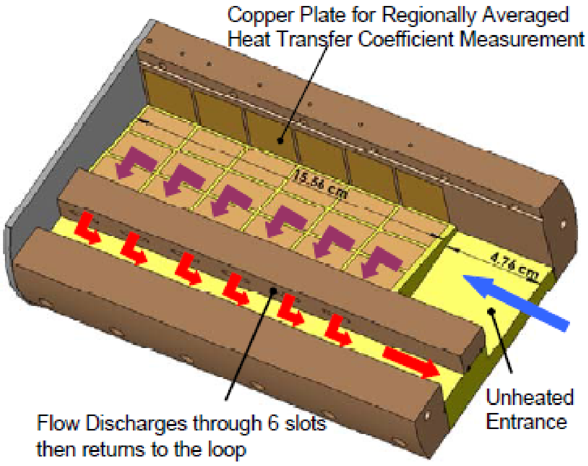

FIGURE 2.21 – Test section investigated by Liu et al. in [19].

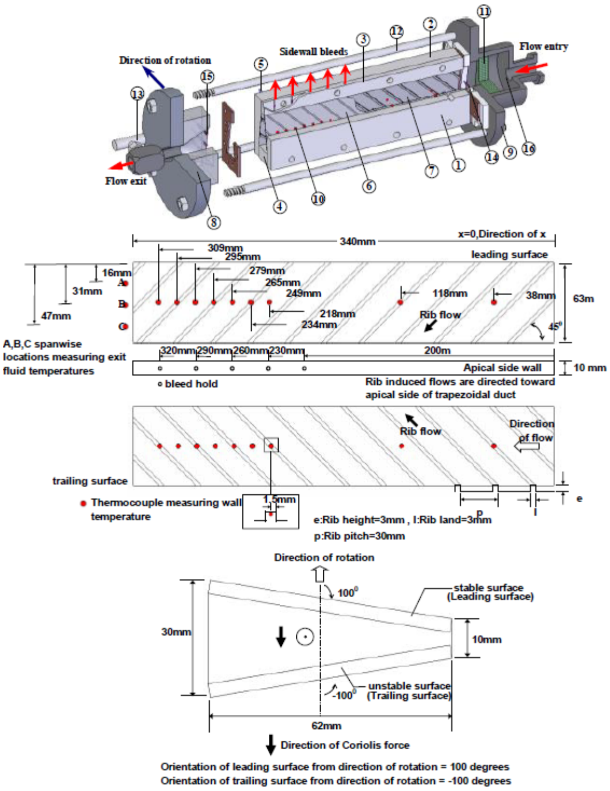

FIGURE 2.22 – Heat transfer test module and test section investigated by Chang et al. in [20].

This latter contribution, together with the works of Rallabandi et al. [42] and Chang et al. [20] (Fig. 2.22) are to the author's knowledge the only examples available in literature referring to cooling schemes with axial flow discharge, so resembling modern TE cavities as depicted in Fig. 1.6. In the aforementioned works, the thermal field investigations were accomplished inside a rotating channel of trapezoidal cross section with flow ejection at the TE through holes ([20]) or slots ([19] and [42]). The pressure boundary conditions were controlled by confining the outlet flow from the main channel in a radial duct used as return passage. It is clear that the centrifugal forces act similarly on the flow both inside and outside the main channel, therefore realising pressure conditions across the channel exits that can be fairly considered rotation independent. However, the adopted return passage, shown in Fig. 2.21, appears to be downsized in order to exclude a priori their influence on the flow developing inside the test section.

In conclusion, the reported review revealed that the experimental investigation on the flow field inside a TE cooling duct resembling the ones currently employed are few, and none of them takes into account for the rotational effects. To the author opinion this kind of activity is necessary since the knowledge gained on, for example, square ducts cannot be applied straightforward.

2.2 Motivation of the present work

Based upon the open literature review, the objective of the current work is to characterise in detail the flow field inside a TE cooling channel, sketched in Fig.2.23, under static and rotating conditions. A complete aero-thermal analysis has been obtained by means of heat transfer coefficient measurements performed at the University of Udine (in the static case) and Florence (in the rotating one).

The channel geometry resembles those of current interest, i.e. cross-section of high aspect ratio, radial inlet flow, and coolant ejection through outlet sections located at both the blade trailing edge and tip.

In the static case, three different channel configurations have been characterised, a basic smooth geometry and then two with *ribs* turbulators installed in different parts of the channel. After a detailed study of the performances, the flow field for the smooth channel and the most promising ribbed configuration was analysed under rotating conditions.

The tests were conducted under engine similar conditions with respect to the selected Reynolds (Re) number and rotation (Ro) numbers, while the flow was isothermal with respect to the channel walls (i.e. neglecting buoyancy effects). The channel orientation (namely the angle between the wall normal direction and the axis of rotation, γ) was equal 0°, in order to maximize the rotational effects coupled with the channel wide cross section.

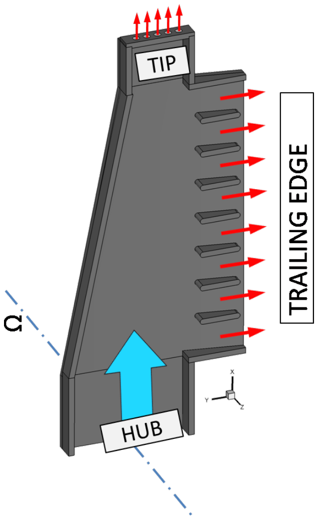

FIGURE 2.23 – Scheme of the channel investigated in the present work.

The aerodynamic flow field has been investigated by means of Particle Image Velocimetry (PIV). Furthermore, to retrieve the relative velocity fields from PIV data acquired in the absolute reference frame, a particular experimental procedure has been developed.

Concerning the HTC measurements under static conditions, these are the first results obtained by the Turbo Machinery research group of the University of Udine (site: *www.diegm.uniud.it/gmse/*) after the developing of the liquid crystal thermography measurement chain, which involved particularly with great efforts Alessandro Armellini. The aerodynamic analysis highlights flow features that are specific characteristics of modern TE internal cooling schemes and leads to a better understanding of the flow mechanisms responsible of the resulting heat transfer under static and rotating conditions. The availability of detailed informations about both the flow and thermal fields makes this work an all-around point of view on the trailing edge cooling problem.

II

Experimental Methodology

3

Particle Image Velocimetry

The PIV is an indirect measurement technique for retrieving the flow field. It is an optical (which read as non intrusive) and highly accurate measurement chain [43]. 2D-PIV provides the simultaneous measurement of two in-plane velocity components over a large number of point belonging to a plane defined by a laser sheet. This technique, developed in the 90' represents a milestone in the aerodynamic measurements class. The possibility of acquiring simultaneous and high accurate velocity data with high spatial and, nowadays, time resolution, allowed the researchers to deeply investigate the flow field as it has never been possible before. The improvement of the basic 2D-PIV lead to *S-PIV*, which measures all the three components of the velocity vector for a number of points laying on a plane, and more recently, the *TOMO PIV*, which provides three components for a cloud of points in a volume of fluid.

3.1 Principles

The principle at the basis of this technique is very simple. First, small tracers are dispersed in the fluid, and then illuminated twice by a light sheet generated by two laser pulses. The time lapse between the two pulses is the *separation time*, ΔT_{PIV}. The particles are imaged by low distortion lenses, and the light scattered is recorded by two exposures of an high sensitivity photo-camera (further information in 3.1.1). The optical layout (i.e. viewing distance, and focal length of the lenses) also determines the second main parameter of the experiment, that is the *Magnification Factor*, defined as $M = f/(f - S_1)$ where f is the lenses focal length and S_1 the distance of the imaged object from the lens plane. It turns that if $|M| > 1$ the image is larger than the object. An increase of M corresponds to higher measurement resolution but the imaged area is reduced, therefore multiple measurement window have to be acquired to span the whole investigation area. A careful choice of M and ΔT_{PIV} is mandatory for a successful use of this technique. A low magnification will turn in a low resolution, that does not allow to detect the flow structures.

Once the images have been acquired, the velocity field is statistically computed over a grid of points by means of a cross correlation procedure between the exposures on the basis of the particle displacement occurred during ΔT_{PIV} (further details will follow in 3.1.2).

In 2D-PIV the optical axis of the lenses is normal to the light sheet, as depicted in Fig.3.1, therefore the measurement plane (defined by the laser sheet), the lens plane and the image plane (defined by the CCD of the camera) are parallel to each other. Consequently, the image will enjoy a constant magnification factor over the camera field-of-view (f-o-v). It is immediately clear that a non uniform magnification factor determines a distortion of the flow field, therefore particular care has to be dedicated to the alignment of the set up or special correction algorithms have to be used for the correction of unavoidable aberrations (*image dewarping*).

A low separation time will turn in small displacement of the traces, determining therefore an high uncertainty. If the separation time is too long, the particle displacement will exceed the optimum value, which is commonly considered as 1/4 of the interrogation window size ([44], see 3.1.2), or will determine a high number of *lost particles*, if the out-of-plane[1] component of the particles is strong. This latter circumstance is detrimental for a correct cross-correlation of the image pair. Indeed the cross correlation requires a minim number of particle imaged in both the exposures to determine correctly the flow field.

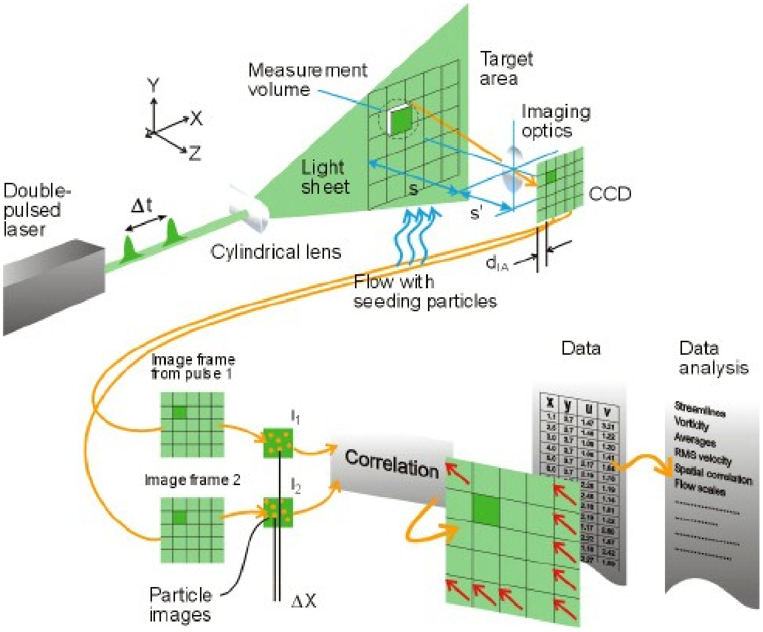

FIGURE 3.1 – Particle image velocimetry working principle

---

[1] i.e. normal to the light sheet.

3.1.1 PIV image recording

In the following some important aspects concerning correct PIV image acquisition are reported.

Firstly the velocity field is retrieved from the tracers displacements, it is important that these latter follow the fluid motion with the minimum possible velocity lag. Thus, the choice of particles with correct physical properties, in relation with the expected flow field is essential. Moreover, the particle size determines the amount of light scattered. The bigger is the diameter, the larger will be the amount of light scattered. It seems that bigger particles could be desirable, but the higher inertia will turn in an higher drift with respect to the fluid motion. Therefore it is clear that a trade-off between the requirements has to be achieved.

One of the crucial aspects of correct image recording is the light intensity of the images. For a given $f-number$ of the lenses [2] the resulting image intensity is proportional to the light intensity of the light source and to the exposure time. If the images are under-exposed, correct light intensity may be obtained by a longer exposure time, but the drawback is a decrease in the particle sharpness (blur) in view of the particle motion. The exposure time has than to be as short as possible. In standard PIV applications, any shutter device is adopted to properly control the integration time: this latter is controlled by the laser pulse duration. At this regard Nd:Yag double cavity lasers can generate high energy pulses with a duration in the order of some ns [3].

A specific mention has to be regarded to the synchroniser used to drive the measurement chain. If the user selected separation time does not fully match the effective ΔT_{PIV} an error in the determination of the velocity components will rise. Moreover, the trigger input to Nd:Yag lasers is followed by a light pulse emission only after a specific time delay, that is the laser $Q - switch$ delay. This compel to the synchronisation of the lasers pulses with the camera operation to allow image acquisition with the correct ΔT_{PIV}. Fortunately, nowadays precise synchronisers with an accuracy of $1ns$ are currently available.

At this point it should be clear that the basic principle at the basis of the PIV technique required a noteworthy technical effort to obtain concrete applications.

3.1.2 PIV Image Processing

The 2D cross correlation consists essentially in the spatial convolution of the signal related to the light scattered by the tracers in a 2D-PIV image pair. More in detail, the flow field imaged by the cameras is divided in sub-zones, called interrogation windows (i.w.) and each i.w. of the first image of the pair is cross-correlated with its correspondent in the second one. The correlation map will show a correlation peak at the location of the most likely displacement of the particles contained in each i.w. The detailed description of the cross correlation algorithm can be found in [44].

---

[2] *Focal-length to lens-diameter* ratio. The higher f-numbers correspond to a low light intensity exposures and the to the maximum depth of field. The lowest f-numbers correspond to full lens aperture, therefore to the maximum light intensity reaching the CCD.

[3] However, there are some applications which made use of a continuous light source as the test rig developed by Di Sante [33] .

In order to better resolve complex flow features (as velocity gradients and vortex structures) more complex cross correlation algorithms have been developed since 2D-PIV has been introduced, allowing to improve the spatial resolution and accuracy of the technique.

The most important one is surely the window offset displacement described in the following, which most representative implementation is surely the well-known Window Displacement Iterative Multi-grid (WIDIM) algorithm developed by Scarano [45]. First, a predicted displacement is obtained by a first cross correlation of the image pair, then the i.w. pertaining to the second frame are moved on the basis of the predicted displacement. By doing so, a second cross correlation will be applied in a region where the particles have more probably moved. The described process is iterative and can be repeated several times. This procedure is coupled whit a grid refinement: the predicted displacement is computed on a coarse grid (large i.w.) at step i and it is used as a predictor for a finer grid at step $i + 1$, allowing to improve the spatial resolution and the dynamic range.

With the same purpose of improving the accuracy on the flow field, other refinements on the method can be adopted: window distortion, sub-pixel interpolation and overlapping. The window distortion consists in using a distorted second window to find a better matching between particle locations, as window displacement does . The i.ws. are distorted on the basis of the local velocity gradient computed in the predictor step.

The sub-pixel interpolation is crucial to improve the spatial accuracy beyond the images limit that is 1 *px*. In fact, since the camera sensors have a finite number of pixels, the cross correlation will display a discrete correlation peak. Therefore, the true displacement will have an estimated value rounded to integer values. This occurrence is commonly referred as *peak locking* effect. However, an interpolation scheme can be adopted to avoid peak locking: the most used is a Gaussian interpolation on a pixel stencil of 3×3 *px*.

Finally, everything that stays stagnant in the image (e.g., image background and light reflections from stationary objects) concurs to decrease of the signal-to-noise ratio of the images and yields to a displacement bias towards 0 *px*. To avoid this, a reference image, usually referred as *background image*, is subtracted to the images before the cross-correlation.

If all the issues here described are adopted, an error of 0.05 *px* on the velocity field is nowadays commonly assumed as the upper-bound uncertainty pertaining to the cross correlation procedure.

3.1.3 Stereoscopic Particle Image Velocimetry

The limitations of 2D-PIV mainly consist in the impossibility to measure the tracers out of plane motion and in the strong augmentation of the parallax error with the increase of the out of plane component magnitude.

The S-PIV employs two cameras to image the same portion of the flow field but from two different off-axis positions. The additional information provided by the additional camera can be used to solve the three dimensional velocity field. This situation can be sketched as solving a linear system for three unknowns (U,V, and W) with two equations given by each of the two cameras.

According to the viewing configuration, S-PIV systems can be broadly divided in translational or rotational (also known as angular displacement) systems [46].

Translational systems

In translational systems the image axes of both cameras are parallel to each other and orthogonal to the light sheet (Fig. 3.2(a)). The primary advantage of this method is its simplicity: because image and lens planes are parallel to the measurement plane, the image field has a constant magnification factor and consequently, no image dewarping process is required prior to the cross correlation and displacement reconstruction. Moreover the camera depth-of-field requirements and image focussing are similar to standard 2D-PIV.

However, the limitations inherent to this configuration are:

- the "common area" imaged by the cameras is small;
- a lower upper bound limit of the off axis angle θ.

The latter yields to the main drawback of this configuration, that is a low accuracy on the out of plane component [47, 48]. For these reasons the translational configuration has found limited applications, in favour of the more diffused angular displacement systems.

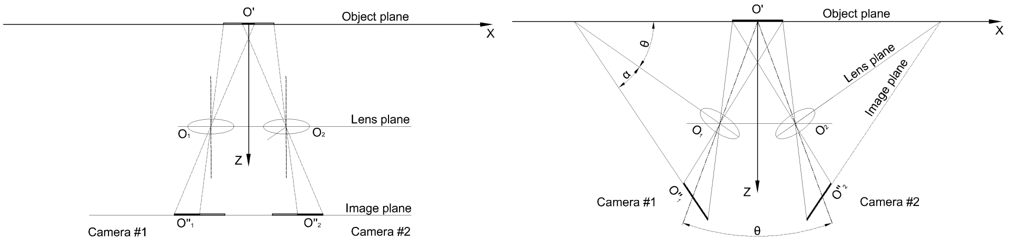

(a) (b)

FIGURE 3.2 – Stereo configurations: translational configuration (a), angular displacement(b).

Angular systems

In angular displacement systems, Fig. 3.2(b), the camera axes are not parallel, but they intersect each other inside the object plane: this solution compensates to the angular limitation of the translational systems, allowing an increase of the out of plane accuracy.

On the other side, the angular displacement requires to deal with some aspects of imaging a plane through an angled direction:

- the focused area is small with respect to the camera f-o-v;
- the magnification factor is not constant over the f-o-v of each camera.

To overcame the first issue the image plane (i.e. the CCD) has to be tilted in such a way that image plane, lens plane and object plane are collinear (Sheimplfug condition). Fig. 3.3) shows the two-axis Sheimplfug adapter realised at the University of Udine.

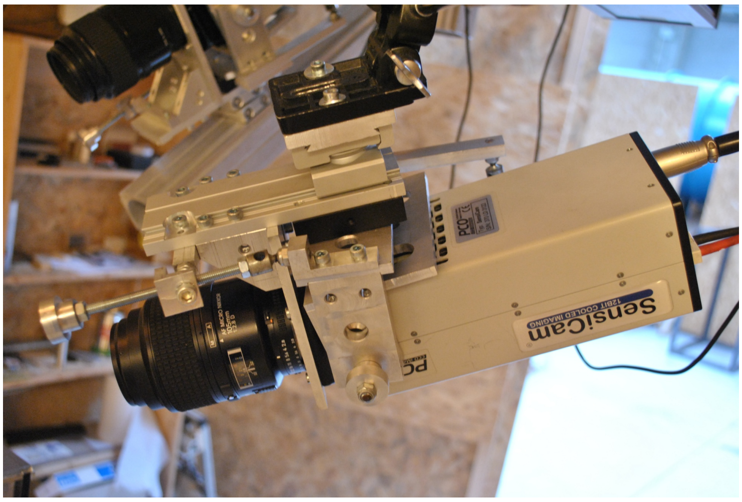

FIGURE 3.3 – The Sheimpflug adapter to realize the Sheimpflug condition, realised at the University of Udine during this research project .

The outcome of the second issue, namely the prospective distortion, is that proper image manipulation is mandatory prior to combine the informations provided by the two cameras. This can be referred as the *stereo reconstruction* procedure.

The stereo reconstruction

The reconstruction process is basically the processing of mapping the displacements measured by each camera onto the object plane and combining them to obtain the three dimensional data. Stereo reconstruction can be performed in two ways:

- geometric;
- calibration based.

Geometric reconstruction is possible only when the geometry of the recording configuration is completely known and can be mathematically modelled. Mathematical modelling may not be possible in presence of non-linearities such as lens distortion or a misaligned CCD array. For these reasons Geometric reconstruction algorithms are scarcely used.

Calibration-based reconstruction may be further classified into 2-D or 3-D calibration methods. In the former, a mapping function is determined to relate each of the two 2D image planes to the 2D object plane. The optical configuration parameters are still necessary to compute 3D displacement field starting from the two 2D camera ones. The latter method, instead, provides a direct relationship between the particle location in a

3D space with its position on each of the image planes, therefore any knowledge about the optical set-up is no longer needed.

Whatever the selected approach is, all the calibration based methods require the placement of a target on the object plane[4]. This latter is a plate where a regular pattern with known spacing is drawn. The grid can be made of dots, crosses, or lines. Anyhow the target looks like, the calibration process requires the acquisition of multiple exposures of the target placed at different and known off-axis (z) positions. The exposures are then cross correlated with an appropriate sample signal to retrieve the grid positions on the image plane, an then the image mapping can be performed following the aforementioned approaches.

2D calibration methods

Briefly, 2D calibration methods require to obtain the calibration data necessary to relate each of the two cameras image plane with the object plane and then to determine the mapping function to perform image dewarping. Once the target is removed and the data acquisition is performed, the raw images are dewarped and cross correlated on a cartesian grid in the image plane. Then the same mapping function is used to project the two displacement fields over the object plane, where they are further interpolated to a common grid. At this point stereo reconstruction can be performed to obtain Δx,Δy and Δz as it follows:

$$\Delta x = \frac{dx_2 \cdot \tan(\alpha_1) - dx_1 \cdot \tan(\alpha_2)}{\tan(\alpha_1) - \tan(\alpha_2)} \tag{3.1.1}$$

$$\Delta y = \frac{dy_2 \cdot \tan(\beta_1) - dy_1 \cdot \tan(\beta_2)}{tan(\beta_1) - tan(\beta_2)} \tag{3.1.2}$$

$$\Delta z = \frac{dx_2 - dx_1}{tan(\alpha_1) - tan(\alpha_2)} = \frac{dy_2 - dy_1}{tan(\beta_1) - tan(\beta_2)}. \tag{3.1.3}$$

where α and β are the viewing angles and the subscripts indicate the cameras. It is important to note that the calibration data is used also to compute the optical configuration parameters which are still necessary to perform stereo reconstruction, as required by eq. 3.1.1 - 3.1.3. The complete process is described in [44, 49].

3D calibration methods

In contrast to 2D calibration, the 3D approach, followed by [47], does not require the detailed knowledge of the system geometry at any stage. The off plane exposures are used to retrieve the relationship between the three dimensional position on the object plane and the two 2D dimensional image fields.

If the 3D reconstruction is more simple than the approach followed by Willert [49] the drawbacks of the methodology proposed by Soloff et al. [47] are a more complex algorithm of the cross correlation procedure and the impossibility of performing the misalignment correction.

---

[4] Since it is impossible to place the target at the exact position of the laser sheet, an additional source of error has to be considered (*misalignment error*). However, as described in the following, several methods are available to diagnose and correct this error source.

Misalignment error and its correction

In section 3.1.3 it has been observed that the practical impossibility of placing the target at the exact position of the laser sheet turns in the misalignment error. To overcome this drawback, Willert in [49], proposed a methodology to minimise this error source. This procedure is commonly referred as the disparity correction. This latter is based on the fact that the images from the two cameras are back projected to a plane [5] which is not the one where the particles lay, in view of the misalignment. Thus, the same particles will have a different position in the two views. This occurrence can yield to an high bias error. Indeed, when performing the stereo reconstruction velocity vectors pertaining to different portions of the flow field will be combined together.

However, it should be noted that the cross correlation between the two first frames of the image pair will show a non zero value, in view of the misalignment. Willert proposed to use this disparity map to correct the back-projection coefficients, the same approach has been followed followed by Astarita et al. [50]. A more sophisticated approach was proposed by Scarano et al. in [51] and Wieneke [52] where the disparity map was used not only to correct the image de-warping by also the viewing angles.

3.2 The PIV system of the University di Udine

The PIV system of the turbo-machinery research group of the University of Udine, shown in 3.4 includes:

- $125mJ$ double cavity $Nd : Yag$ laser (SOLO PIV, New Wave Research) operated at a wavelength of $532nm$;
- two PCO-SENSICAM 12-bit CCD cameras with a resolution of 1024×1280 px and 4,1 Hz acquisition frequency at the maximum resolution;
- a 16 TTL output channel externally triggerable sequencer from PIVTEC GmbH;
- a Laskin nozzle type seeding generator operated with vegetable oil, which guarantees a very narrow particles size distribution with a mean diameter of $1.2\mu m$;
- two set of low distortion NIKKOR lenses, f=60 mm and f =105 mm both with f/d=2.8.

3.3 Technical details

The separation time ΔT_{PIV} was set trough tests to obtain the maximum allowable mean in plane displacements (equal to 8-9 px 1/4 rule [44]) with the minimum loss of particles due to the out of plane motion of the flow region under investigation. A mean value of

---

[5] It should be remembered that the back projection coefficients are computed with respect to the calibration plane defined by the target.

FIGURE 3.4 – The complete Stereo-PIV measurement chain with the exception of the data acquisition system.

$100 \mu s$ was used for xy planes [6] while the cross wise measurements planes required ΔT_{PIV} ranging from 10 to 35 μs in view of the strong cross-plane velocity.

In order to compute time the averaged velocity field and the related statistics, 1000 image couples have been recorded for each acquisition at a frequency of $4 Hz$, ensuring to have an uncorrelated set of samples for a correct averaging.

2D-PIV

All 2D-PIV images were processed using the commercial software PIVView (PIVTEC GmbH), with a first interrogation window of $64 \times 64 \quad px$, a single step of window size refinement and 50% of window overlapping. Two steps of window distortion-displacement were used for each step of the refinement procedure. Finally, a Gaussian peak-fitting on a 3×3 px stencil was adopted to perform the sub-pixel interpolation.

With these settings, a field of 80×64 displacement vectors was defined in each measurement area with a spatial resolution of 0.5-1.5 mm, depending on the magnification factor. Coarser measurements correspond to $M = 10000$ px/m, while a magnification factor of 30000 px/m was set for the higher resolution ones.

Vector validation was performed with tests based on a normalised median filter and on criteria of primary to secondary correlation peak and minimum signal-to-noise ratio. The percentage of invalid vectors was typically low, less than 3 %, and only the valid vectors were sampled to obtain the time averaged vector fields.

Background subtraction was performed to remove background light noise to enhance

---

[6] See 6.4 for the measurement planes position.

the cross correlation peak. The background image was obtained as the point-by-point minimum of the light intensity of each image series.

The investigated area has been divided in small windows to obtain the correct resolution with respect to flow features. Successive acquisitions have been then non-dimen sionalised with respect to the bulk velocity at the channel inlet (U_b).

S-PIV

The stereo images were processed performing image back-projection and then stereo reconstruction (PIVView, PIVTEC GmbH). The nominal magnification of the images was $30px/mm$.

The measurement chain calibration was realised by means of 6 exposures of a calibration target acquired at different off-plane positions. The target was made of an orthogonal grid of black dots of $0.8mm$ diameter on white background. The grid spacing was $2 \times 2mm$, which resulted in more than 200 dots on each exposure, sufficient for an accurate image dewarping.

As suggested in [49], a disparity correction was used to minimise the misalignment errors. At this regard, the disparity map was obtained by means of the ensemble correlation of the first image of 100 image pairs, instead of a single image couple, to increase the accuracy on the disparity map, as proposed by Scarano et al. [51].

The cross correlation of the images followed the approach of 2D-PIV image processing reported above. The spatial resolution of the S-PIV measurement was equal to 0.5 mm.

4

PIV in rotating channels

Dealing with flow field under rotation is a though challenge. In order to obtain the relative velocity field, the choice is between an on-board measurement chain, whose direct output is the relative velocity, or a fixed one, which requires an additional data processing to retrieve the desired informations. The following section describes the state of the art of rotating PIV measurements and presents the methodology used in the present work. This latter has been published in Armellini et al. [53]

4.1 Survey of PIV applications in rotating channels

In the last years, LDV and more recently PIV have been widely applied to study the relative flow field inside rotating test sections. Turbomachinery research has played a driving role for this development, requiring detailed analysis of rotational effects on the flow field inside centrifugal impellers or internal ducts used for gas turbines blades cooling.

When the target is to measure the relative flow field, two opposite strategies can be followed: either a direct methodology that makes use of a measurement chain rotating integral with the test section and therefore able to directly measure the velocity in the relative reference frame, or an indirect method where the measurement system is kept fixed and synchronised with the periodical passage of the test section (phase-locked mode). In this latter case, the absolute velocity field is measured and the relative one is obtained only after a proper data processing. A direct measurement of the relative velocity allows to keep the uncertainty at the same values of a standard/non-rotating measurement but produces a strong growth of both costs and complexity of the measurement chain. Therefore the choice of a direct or indirect method is mainly based on a trade off between accuracy and cost of the experimental setup. For this reason the majority of the experiments that can be found in literature used standard, fixed, LDV pr PIV systems operated in a phase-locked mode.

Concerning PIV applications, examples of relative flow field investigations inside centrifugal impellers are found in [54–61]. In these studies the authors made use of standard PIV chains that in almost all cases were synchronised with the impeller in order to perform phase-locked acquisitions of the absolute flow velocity in a blade-to-blade plane. The relative flow field was then computed through a post-processing procedure of the PIV data, i.e. performing a vectorial subtraction of the local peripheral velocity, $\vec{U} = \vec{\omega} \times \vec{R}$, from the measured absolute one, $\vec{C}$. A description of how this procedure was applied, for instance about the definition of the centre of rotation position ($\vec{R}$), is not available in [55–60]. Only Westra et al. [61] reported the use of an image calibration based on the measured value of the rotational speed and on the known coordinates of a marker placed on the impeller, while Wuibaut et al. [54] adopted a post-treatment procedure to locate the centre of rotation in the image frame but did not provide any detailed information about it. Assessments of the uncertainty associated to the determination of the peripheral velocity and of the over-all accuracy of the post-processing procedure might have been also useful, but they are not provided in the works previously mentioned. The only attempts of a direct measurement of the relative velocity field inside radial flow impellers are found in [62–64]. In the first two cases, [62, 63], the authors performed PIV investigations with a CCD camera rotating with the test section itself, while Stickland et al. [64] used a fixed camera combined with an image de-rotator realised by means of a mirror system rotating at half the speed of the test section.

A first example of PIV investigation of the relative flow field inside cooling channels for gas turbine blades is presented by Bons et al. [32]. They used a fixed PIV system synchronised in phase-locked mode with the test section. In order to increase the results accuracy, they adopted a pre-processing procedure of the raw PIV data. It consists to de-rotate every second frame of a PIV image pair of an angle equal to that swept by the test section during the elapsed time between first and second frame acquisitions. This approach allows to compute directly the relative velocities from images acquired in the absolute reference frame, nevertheless the authors estimated that this reference frame transformation can lead to a bias error up to 5%. This bias derives from errors in the determination of the centre of rotation and from the image manipulation itself and it should be summed to the uncertainty usually associated to a standard PIV measurement. Further examples about experimental analysis of relative flow fields inside rotating cooling ducts are the contribution of Servouze et al. [65], Gallo et al. [66] and Elfert et al. [34, 67]. All of them used a fixed PIV system, phase-locked acquisition and different synchronisation approaches, nevertheless none provided a detailed analysis of the actual uncertainty of the reported relative velocities. Direct measurement of the relative flow field have instead been attempted by Bharadwaj et al. [68] and Iacovides et al. [69]. In both cases the laser beam was aligned with the channel axis of rotation and successively deflected inside the test section by a rotating mirror, the image acquisition was obtained by means of either a fixed camera combined with a rotoscope, [68], or a camera rotating integral with the test section, [69]. The strong technical complexity of these experimental set-ups may have likely spoiled part of the expected advantages and, indeed, only preliminarily results, [68], or flow visualizations, [69], are presented under rotating conditions.

A totally different experimental approach has been recently adopted by Visscher et al. [70]. They conducted Stereo-PIV measurements of a fully developed flow inside a rotating rectangular duct mounted on a 14 m diameter turntable that is able to house the whole test section, the PIV measurement chain and the control and acquisition systems. Thanks to their noteworthy technical efforts the authors were able to get highly accurate and spatially resolved relative flow measurements. A similar approach was also followed by Di Sante et al. [33] that presented the first time-resolved PIV measurements inside a boundary layer of a diverging rectangular channel under both static and rotating conditions. High accuracy, spatial and temporal resolution were obtained by means of a new facility made of a 2.5 m rotating disk on which both the test section and the PIV system were mounted. In their paper, [33], the authors also provided a comparison between the measurement accuracy attainable with their approach (which is simply the accuracy of the PIV cross-correlation algorithms, that usually leads to an uncertainty of about 1-2% with respect to the measured value) and the one that should be expected if an indirect measure would be used. By following the error propagation theory, [71], Di Sante et al. [33] concluded that the error associated to an indirect measure shows a quadratic growth at increasing the ratio between the absolute and relative velocity modulus so providing completely unreliable data in those cases where the peripheral velocity is much higher than the relative one. However the error analysis by Di Sante et al. [33] suffers by the approximation that the uncertainty on the determination of the peripheral velocity was completely neglected, and they do not consider the possibility to pre-process the data in the way adopted by Bons et al. [32].

The present analysis of the current literature shows that for the investigation of the relative flow field inside rotating test section by means of PIV techniques, the indirect approach is widely preferred with respect to the more accurate but by far more complex direct approach. However, despite the numerous examples of applications, a comprehensive report about the uncertainty of the indirect method is not available.

4.1.1 Approach followed in the present work

In the present application the choice was to go for a fixed measurement chain. In the case of 2D-PIV the relative flow field has been retrieved after a proper image manipulation before image cross-correlation. The careful implementation of the methodology allowed to obtain outstanding results in therms of accuracy and flexibility of the 2D-PIV measurement chain. The details of the procedure and its accuracy assessment can be found in [53]

4.2 Image De-rotation algorithm

In concrete terms, the image pre-processing consists of rotating the second frame (frame B) of every PIV image pair by an angle equal and opposite to the one swept by the test section (2β in Fig. 4.4) during the elapsed time, ΔT_{PIV}, between the two frames (frames A and B) as suggested by Bons et al.[32]. However, some improvements were introduced to enhance remarkably the accuracy of the measurements.

A calibration procedure has been developed on purpose, allowing to determine the centre of rotation position with respect to every pixel of the PIV image by means of an indirect measurement with high precision. Once the acquisition is accomplished, for each image pair, the de-rotated frame, say B*, is reconstructed from the raw second image of the PIV image pair (FRAME B). In the present case the image reconstruction is performed by means of the SINC-8 interpolation scheme.

4.2.1 Determination of the Centre of rotation

In the indirect method here proposed a target made of N_p black dots on a white background (markers) is aligned with the measurement plane and two images, respectively frame A and B, are acquired at two different angular positions of the test section. A picture of the calibration target is presented in Fig. 4.2. Successively, the coordinates of each *i-th* marker center in the two frames ($x_{i,A},\ y_{i,A}$ and $x_{i,B},\ y_{i,B}$) are determined through a cross-correlation with a sample signal (Fig.4.3). Finally, the geometrical relationship represented in Fig. 4.1 is used to write the following equation for each *i-th* markers pair:

$$x_C(x_{i,A} - x_{i,B}) + y_C(y_{i,A} - y_{i,B}) = \tag{4.2.1}$$

$$= \frac{x_{i,A}^2 - x_{i,B}^2 + y_{i,A}^2 - y_{i,B}^2}{2} \tag{4.2.2}$$

where $x_C,\ y_C$ are the unknown terms.
A priori, the coordinates of the centre of rotation could be obtained with only two equations of the same type as eq. 4.2.2 (i.e. by using two markers). However, since the markers' positions are affected by the errors $\delta x_i,\ \delta y_i$, a better accuracy can be obtained with N_p much bigger than 2, therefore through the solution of a overdetermined linear system.

It should be noted that this methodology allows to determine the centre of rotation position in a very simple manner. Indeed, since the measurement of the angular velocity is not necessary, it is possible to perform the calibration by simply acquiring exposures of

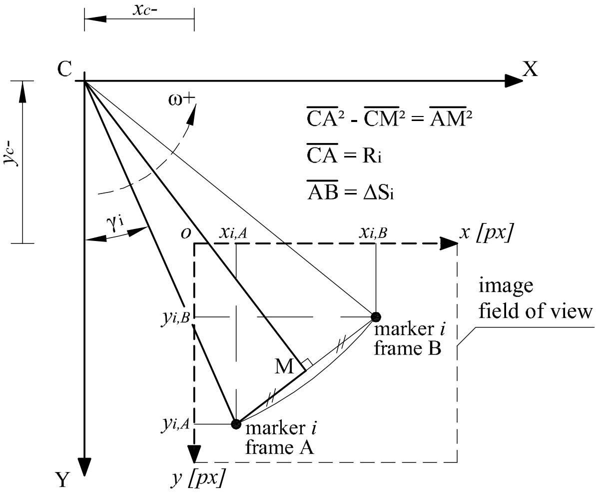

FIGURE 4.1 – Geometrical reconstruction of the calibration markers peripheral displacement used to derive eq. 4.2.2.

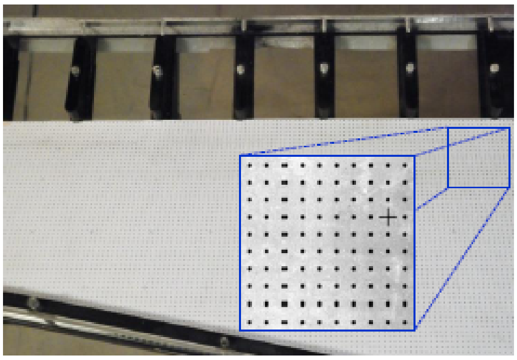

FIGURE 4.2 – Calibration target for centre of rotation determination.

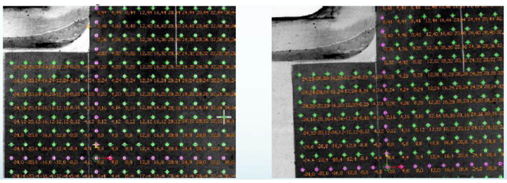

FIGURE 4.3 – Two exposures at different angular position for centre of rotation determination.

the calibration target with the channel at two different angular positions not necessary under rotation.

4.2.2 Measurement of angular velocity

To obtain the angular velocity there are two methods: to use an incremental encoder to get a measure of the instantaneous value of Ω or to sample a once-per-revolution signal to measure the mean value of Ω during each round. If this last approach is implemented by means of high frequency counter boards ($> 20MHz$), the mean value of Ω can be measured with a very high accuracy, i.e. well below 0.1% even for a rotational speed of about 10^4 rpm. The uncertainty analysis for the two methods can be found in [53]. A problem can rise instead from the assumption of steady conditions during a revolution. Hence, the uncertainty $\delta\Omega/\Omega$ has to be evaluated on the basis of the amplitude of the Ω fluctuations during each revolution. In practice, this is an approach that can be successfully used only if the momentum of inertia of the test section is quite high.

In the present work the test section moment of inertia was considerably high, as confirmed by the evidence that the $r.m.s.$ of the angular velocity fluctuation was $0.0025 rad/s$. This allowed to use and incremental encoder to sample the angular velocity and to assume that the mean angular velocity was a meaningful estimate of the instantaneous one in a small interval close to the measurement point. This assumption was later confirmed by a good image acquisition stability: the channel wall position between the first frames of different image pairs showed a difference of less than 1 px.

4.2.3 Determination of the peripheral displacement field

Once the Ω and the position of the centre of rotation are known, the peripheral displacement, ΔS, of a point P that during a temporal interval ΔT_{PIV} moves around a centre of rotation C with angular velocity Ω (Fig. 4.4), can be expressed by means of a simple geometrical relationship:

$$\Delta S = 2Rsin(\beta). \tag{4.2.3}$$

The radius of rotation R and the semi swept angle β are computed as it follows:

$$R = \sqrt{X_P^2 + Y_P^2}, \tag{4.2.4}$$

$$X_P = x_P - x_c, \quad Y_P = y_P - y_c, \tag{4.2.5}$$

$$\beta = \omega \Delta t_{PIV}/2. \tag{4.2.6}$$

The angular position of the point P with respect to the global reference frame is defined as:

$$\gamma = atan2\left(\frac{X_p}{Y_p}\right), \tag{4.2.7}$$

so that the x and y components of the peripheral displacement can be computed as:

$$\Delta S_x = \Delta Scos(\beta + \gamma), \tag{4.2.8}$$

$$\Delta S_y = -\Delta Ssin(\beta + \gamma). \tag{4.2.9}$$

Therefore the knowledge of Ω and the position of point P with respect to the centre of rotation R is required to determine the peripheral displacements field.

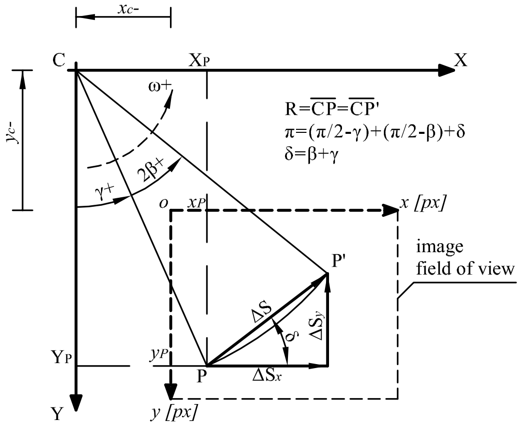

FIGURE 4.4 – Determination of the peripheral displacement field in the image reference scheme.

4.2.4 Image De-rotation

Once all the parameters are known the image de-rotation is a quite simple task. Briefly, ΔS_x and ΔS_y define the points of frame B from which the light intensity signal must be interpolated to reconstruct the intensity value of the pixel belonging to frame B*.

However the choice of a suitable interpolation scheme is a key point for the accuracy of the procedure. Indeed, a too simple interpolation scheme, such as a bi-linear or a cubic one, will introduce a reconstruction error comparable to the one of the cross-correlation procedure, therefore spoiling the advantages of this methodology. In the present case the image reconstruction is performed by means of the SINC-8 interpolation scheme, which performs the interpolation of the light intensity signal on 8x8 *px* stencils based upon the SINC filter. This method ensures accurate image reconstructions with associated errors of less than 0.01 *px* as showed by Astarita et al. [72]. A schematic of the interpolation scheme is reported in Fig. 4.5.

In the following an example of the results of the present methodology are reported. Fig. 4.6 shows a raw image pair. The channel wall clearly show the peripheral displacement occurred during the separation time. On the other hand, in Fig. 4.7 the de-rotated image pair is presented. In this latter, the particle displacement due to rotation have been subtracted, thus the cross correlation software will then determine directly the relative displacement filed (Fig. 4.8 (b)). By contrast, if the image de-rotation is not performed the output of the PIV image processing is the absolute displacement field (Fig. 4.8(a)),

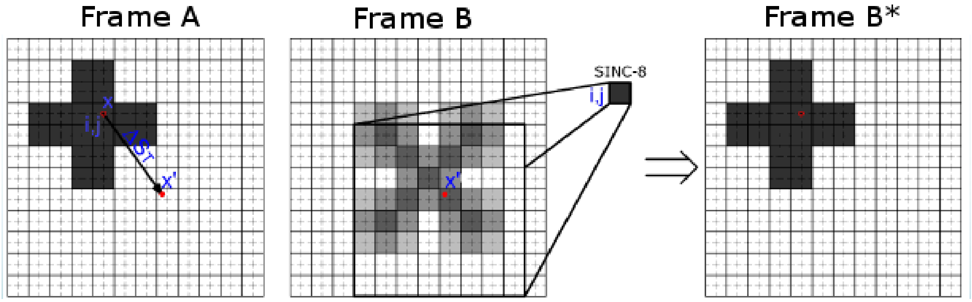

FIGURE 4.5 – Scheme of the de-rotation method.

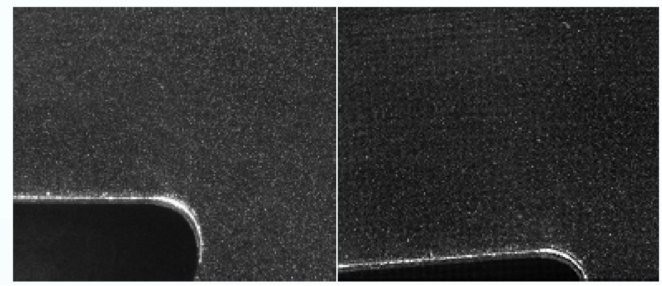

FIGURE 4.6 – Raw image pair.

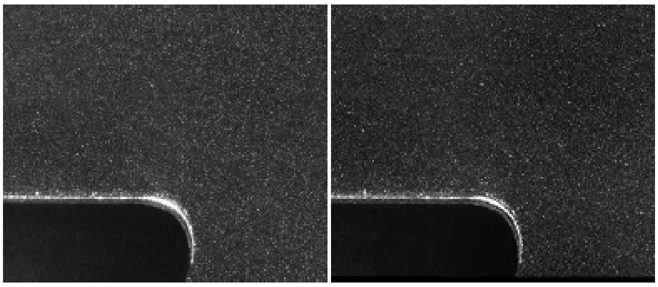

FIGURE 4.7 – De-rotated image pair.

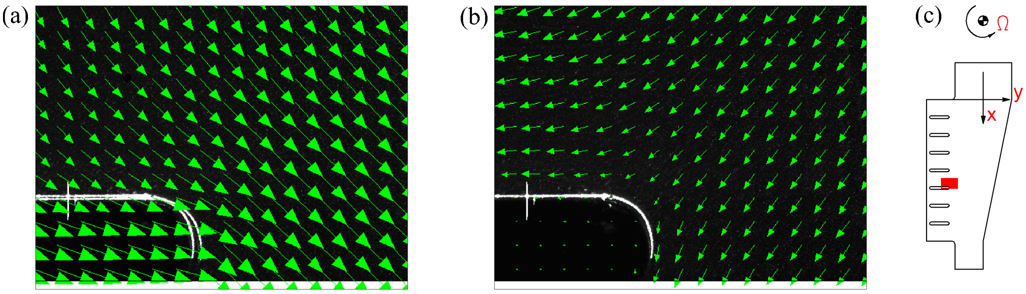

FIGURE 4.8 – Cross correlation results for a raw image pair (a) and a post-processed one (b). $M = 10px/mm$, $\Delta T_{PIV} = 100\mu s$. Vector resolution equal to 1/2 the effective one. (c): sketch of the measurement window position.

then the relative one has to be obtained by subtracting the peripheral velocity field.

4.2.5 Methodology for S-PIV measurements

The previous section presented the procedure used in the case of 2D measurements in planes orthogonal to the axis of rotation, which made use of the image de-rotation. On the other hand, the relative velocity field for S-PIV measurements was determined through a standard post processing of the data sets, i.e. the subtraction of the instantaneous peripheral velocity before averaging the samples to take into account of small drifts in the angular velocity. Indeed a de-rotation pre-processing for stereo PIV images would be more complex and less accurate. To understand this statement the reader should keep in mind that the de-rotation would be performed taking into account of the viewing angles. Since the calibration of S-PIV can be considered as its major weakness due to the misalignment error (see chapter 3), it easily follows that the same bias error source will affect two times the measured values, once in the calibration and once in the de-rotation. This compelled to retrieve the velocity field by means of the subtraction of the peripheral velocity. However, the comparison with 2D-PIV data showed anyway a satisfactory result as reported in A.2.

5

Thermal measurements

As stated in 2.2, HTC measurements for the present channel geometry have been performed by the research groups of the University of Udine and Florence. In the following the description of the detail of the Liquid Crystal Thermography (LCT) measurement chain developed by the turbo-machinery research group of the University of Udine is reported. This technique was recently achieved thanks to the efforts of Alessandro Armellini.

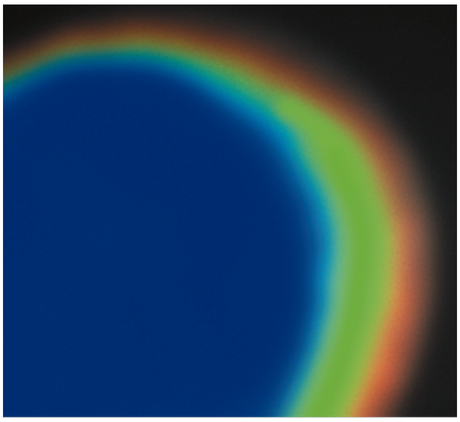

FIGURE 5.1 – An example of a LCT picture.

5.1 Liquid Crystal Thermography

The LCT allows to measure the HTC distribution on a wall due to the forced convection heat exchange that takes place at the wall under investigation. More in detail the heat balance for a surface of an internal cooling channel model can be expressed as:

$$\dot{q_{fc}} = \dot{q_f} + \dot{q_{disp}} + \dot{q_{irr}} \tag{5.1.1}$$

where $\dot{q_{fc}}$ is the heat exchanged between the fluid and the surface by means of forced convection, $\dot{q_f}$ is a uniform heat source properly generated, $\dot{q_{disp}}$ is the heat lost to the ambient and $\dot{q_{irr}}$ is the radiative heat rate exchanged with the other surfaces of the model.

The heat exchanged by forced convection can be described by the well known relationship:

$$h = \frac{\dot{q_{fc}}}{T_w - T_b} \tag{5.1.2}$$

where T_w is point wise temperature at the wall, T_{bulk} is the bulk flow temperature. T_{bulk} is a reference temperature of the flow and can be defined as, for example, the temperature of the fluid at the channel inlet. The idea at the basis of the technique is that T_w can be measured through the relationship between this latter and the colour of the light scattered by the liquid crystal layer.

For what concerns $\dot{q_{fc}}$, a thin layer ($25\mu m$) of Inconel 600 was placed at the SS of the channel, and the dissipation of DC power into this heating foil allows to generate an heat flux used as a thermal boundary condition. This latter can be considered uniform over the Inconel surface and it can be varied changing the DC power, thus enabling to control the surface temperature inside the operational range of the liquid crystals.

The radiative heat exchanged with the other surfaces of the model (Fig. 5.2) can be considered negligible, since the PPMA walls can be considered opaque to infra-red light. With the aim to minimise the heat exchange with the environment, a 2 mm air gap between the channel external surface and glass sheet provided an additional insulation.

In the present experimental campaign, the measurements were performed on the SS wall. With the aim to simplify the viewing configuration it was chosen to imagine the liquid crystal painted surface through the external wall, as sketched in Fig. 5.2). A thin film of SPN-R40C5W liquid crystals from Hallcrest (operative range 40-45 °C) was sprayed with an air brush onto the channel SS internal surface. Subsequently, it has been

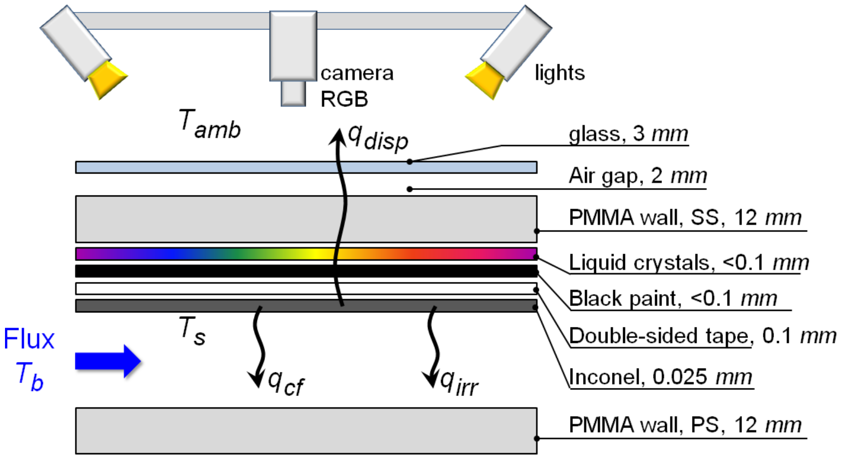

FIGURE 5.2 – Sketch of the set-up used for the LCT measurements.

applied a layer of opaque black paint (SPBB-G1-Hallcrest) and a thin double-sided tape where the heating foil was placed.

The image acquisition was performed by a colour digital camera P83B-GIGE-AR with a resolution of 1034x779 *px*. The lens used was a Schneider KREUZNACH f#1.4-f12 *mm* which allowed a resolution of 5.5 *px/mm*, thus the measurement area has been divided in a number of sub-zones. The lighting system comprised two SoLux halogen lamps mounted on props fixed whit the camera mount. The lamps were chosen because of their low UV emission [73] and a uniform light intensity and spectra over the camera f-o-v.

Pictures of the target wall were acquired at different heat flux settings once the thermal equilibrium is established. The procedure was described by Cakan [74]. A MATLAB code developed by Alessandro Armellini has been used to extract the isothermal lines.

The LCT measurement chain was calibrated by means of the conversion from the RGB (Red, Green, Blue) space to HSI (Hue, Saturation, Intensity) which was then related to the surface temperature with a device developed on purpose as proposed by Akino et al.[75]. This latter is able to generate a known temperature gradient on a aluminium slab painted with the Liquid crystals. Particular care was devoted to perform the calibration with the same viewing arrangement used for the measurements. Finally, T_{bulk} was measured by means of thermocouples placed inside the settling chamber, upstream of the honeycomb filter (Fig. 6.6).

The HTC measured with the LCT has then used to characterise the thermal field referring to the Nu defined as:

$$Nu = \frac{h\ Dh}{\lambda} \tag{5.1.3}$$

where λ is the thermal conductivity of air, and Dh is the hydraulic diameter at the channel inlet.

6

Set up and instrumentation

The following chapter can be divided in two parts: the first one concerns the set-up while the second part describes in detail the test section and conditions. More in detail, the test rig (designed and realized during the present thesis work), the flow circuit and the synchronization strategy of the measurement chain are firstly reported (section 6.1). Then, in 6.2 and 6.4 a description of the test section configurations and of the measurement planes position is provided.

6.1 Test Rig

As previously mentioned, a rotating facility has been developed during this thesis work to perform the experimental campaign. A picture of the test rig is reported in Fig. 6.2. As reported also in Fig. 6.1, the test section and the counterweight frame are sustained by the settling chamber. This, in turn, is connected to the slow shaft of a gear reduction

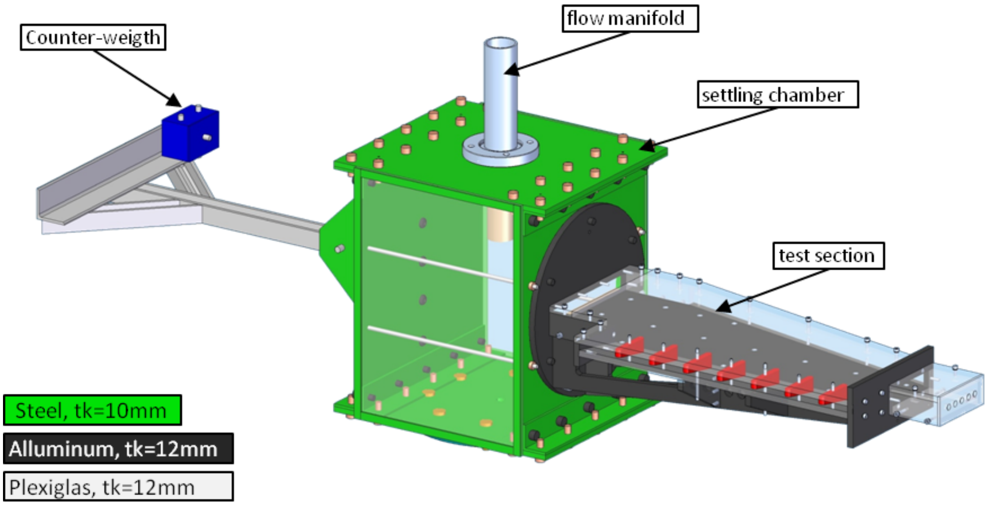

FIGURE 6.1 – Overview of the test rig.

unit. An electric motor coupled with an inverter allows to control the angular velocity with ∓ 0.5 rpm. The nominal rotational speed during the experimental campaign was about 215 rpm.

The test section is composed by an aluminium frame onto which the test section is realised by means of PMMA plates. The aluminium frame ensures the structural solidity of the test section assembly whereas the the PMMA construction allows almost a full optical access. The test section is connected to the settling chamber by means of a flange, which allows the modification of the channel orientation with respect to the axis of rotation. The overall weight of the model is 25 kg. Further description of the test section will follow in sect. 6.2.

The non neglecting weight of the test section and the required counterweight (≈ 8 kg) compelled to use 10 mm thick steel plates to build the rotating settling chamber. However, two lateral walls were made in PMMA to allow visual inspections inside the settling chamber. The settling chamber plus the test section and the counter weight exceed the noteworthy weight of 150kg. All the rotating equipment is hold by the gear

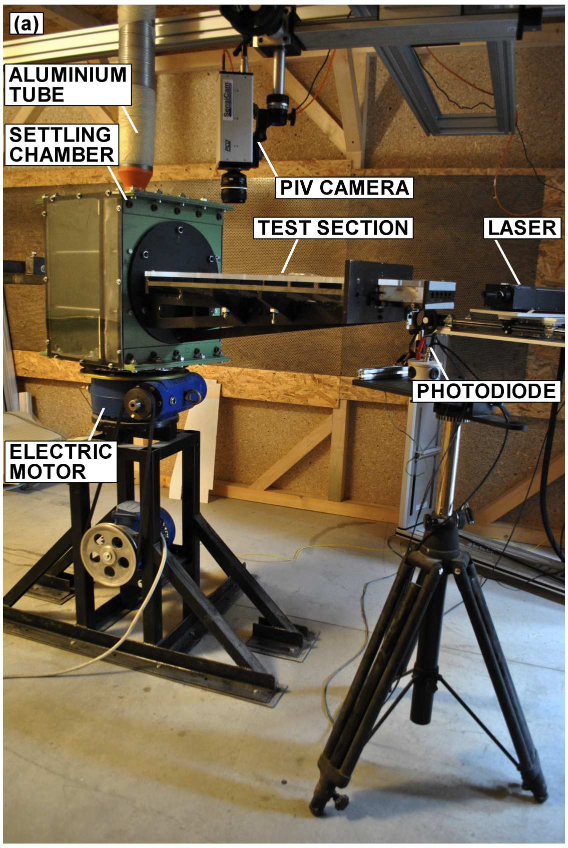

FIGURE 6.2 – Picture of the test rig realised at the University of Udine.

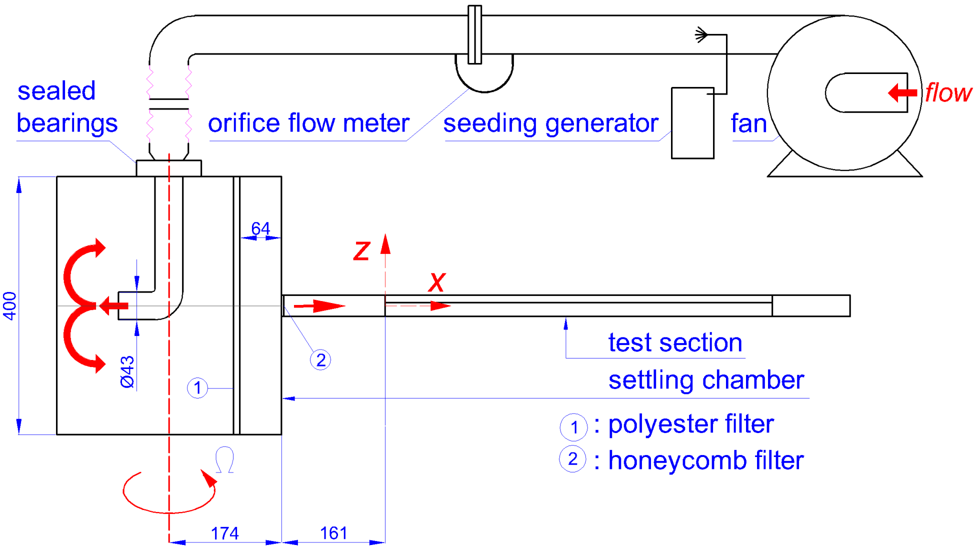

FIGURE 6.3 – Schematic of the test rig developer for the present experimental campaign, xz-projection with the piping circuit.

reduction unit which is mounted on a metallic chassis.

For which concerns the flow circuit, the test section, Fig. 6.3, is fed by means of a 4kW centrifugal fan, which delivers the required mass flow ratio to ensure the selected Reynolds Number at the channel entry (about 0.05 Kg/s). The flow is seeded by the Laskin seeding generator just downstream the fan outlet. Flexible aluminium tubes link the fan to a 3 m long, 97 mm Internal Diameter steel pipe. In the middle of this latter, an orifice flow meter is installed. This latter meets the UNI specifications [76].

The diameter of the orifice is equal to 35 mm, which turns in a pressure drop of about $3,3 \cdot 10^3 Pa$ at the specified mass flow ratio, slightly varying depending on the ambient condition during the tests. The pressure drop is measured by a pressure transducer, while a water-column provided the pressure signal just upstream the orifice flow meter. The air temperature for air density correction was measured upstream the orifice meter by means of a thermocouple.

Afterwards a 4 m long piping circuit of the same internal diameter allows to reach the top of settling chamber. Sealed bearings connect the rotating settling chamber to the aluminium tube (Figs. 6.1, 6.3). The sealed bearings on the top face of the settling chamber are connected to a 45 mm internal diameter pipe. At the settling chamber middle height, a 90 °bend turns the flow towards the settling chamber's wall opposite to the test section. Furthermore, at 65 mm upstream of the test section inlet, a polyester fibre filter is installed. This latter produces the pressure losses necessary to ensure uniform flow conditions at the test section entry, Fig. 6.1. Any effect of flow separation due to the sudden contraction of the flow has been avoided by placing a 3 mm honeycomb filter at the channel inlet (Fig.6.3). The total pressure drop of the circuit is equal to $4356Pa$, slightly varying with the tests conditions. The distance between the axis of rotation and the origin of the channel coordinate system (see Fig.6.3) is equal to 5.75 Dh, computed on the model inlet cross-section.

6.1.1 Phase-locked Synchronisation

In the rotating tests, the measurements of the velocity field have been acquired in *phase-looked* mode, as described in chapter 4. Therefore the data acquisition must be synchronised with the channel rotation, because:

- the PIV measurement chain has a certain time delay between the *trigger input* and the *data acquisition* (Q-Switch delay (QSD), chapter 3);
- the angular velocity Ω of the channel is not constant.

In order to perform the synchronisation, the TTL signal originated by a photo-diode (Fig. 6.4) periodically screened by a target integral to the test section, was sampled with a National Instruments NI-PCI-6601 counter board.

The NI-PCI-6601 has 4 counters at 32 bit with a maximum frequency of 20 Mhz. However, only two of them were used in the present application. In the following we will refer to the two counters of the pair as *counter* 1 and *counter* 2.

Counter 1 was deputed to the continuous measurement of the mean angular velocity over one revolution: the time lapse occurred between two successive rising edges of the photo-diode signal was used to get the measured value of Ω. Once the angular velocity is known, a variable delay for PIV trigger signal can be computed as it follows:

$$\Delta T_{Delay} = \frac{\Delta\alpha}{\Omega} - QSD. \tag{6.1.1}$$

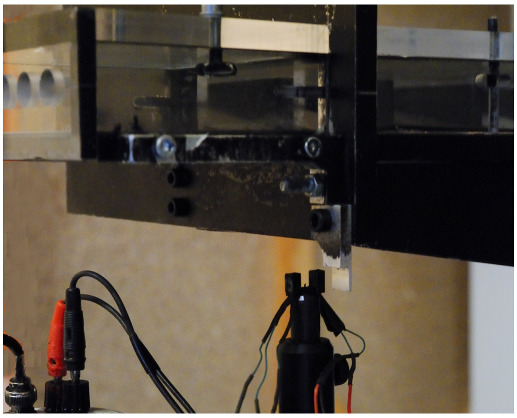

FIGURE 6.4 – Photo-diode and target used to synchronise the channel with the PIV measurement chain.

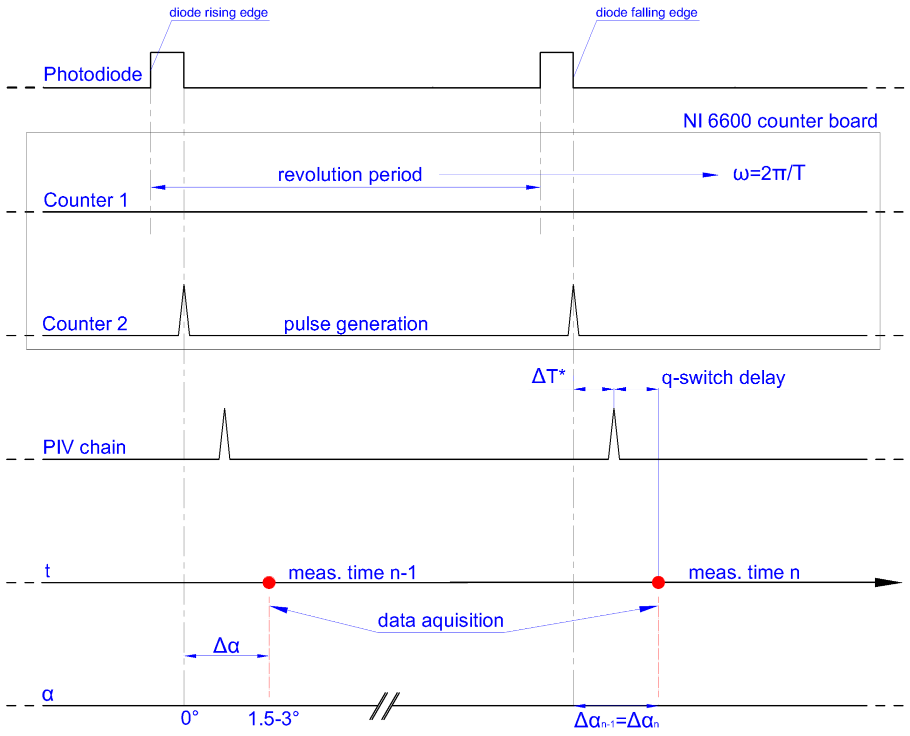

FIGURE 6.5 – Pulses diagram for the synchronisation of the measurement chain with the rotating channel by means of single photo-diode signal.

Where $\Delta\alpha$ is the angle included between the photo-diode and the channel at the measurement position and QSD is equal to $192ns$. On the basis of the computed delay Counter 2 was used to generate a trigger pulse for the PIV measurement chain.

Figure 6.5 reports the impulse time diagram for the measurement chain used in the rotating test for a clearer understanding of the synchronization method.

One last thing has to be addressed: the described procedure can be successfully adopted if the angle included between the photo-diode position and the measurement position $\Delta\alpha$ is kept as small as possible (equal to few degrees). If so, the mean angular velocity over one revolution, that is precisely measured, can be reasonably assumed as constant over $\Delta\alpha$ and, therefore, equation 6.1.1 can be correctly applied to compute ΔT_{Delay}. Thus, thanks to the highly accurate measurement of Ω and to the high momentum of inertia of the test rig that limits its the angular velocity fluctuations between successive revolutions ($\approx 0.0018 rad/s$), the data acquisition can be performed practically always at the same circumferential position. Indeed a shift of less than 1 *px* of the channel walls between successive acquisitions was found at the model tip, which was the worst case.

6.2 Test Section

In the present thesis work, three different channel configurations were investigated:

- G0;
- G1;
- G2.

In the following, the details of each configuration are reported.

Configuration G0. G0 refers to the basic geometry, i.e. the one without turbulence promoters, as sketched in Fig. 6.6.

The inlet section is rectangular with high AR (equal to 7.25), the corresponding Dh is equal to 58mm (Fig. 6.6(d)). In order to provide an almost uniform flow at the entrance of the TE exit section, the channel width is reduced progressively from hub to tip by means of a redirecting wall. This latter deviates the flow towards the wedge shaped TE outlet section at the trailing edge (Fig. 6.6(a,d)). At the model tip, a short channel with rectangular cross section (having the same height of the main channel but AR=3.625) guides the flow towards the tip exit made of five equally spaced holes of 7 mm radius (Fig. 6.6(e)). Inside the TE section, seven elongated pedestals are installed to ensure structural rigidity and to promote flow turbulence (Fig. 6.6(a,b)). Finally, the channel wall at $z = 16.55$ mm is intended to be the PS, whereas the opposite is the SS.

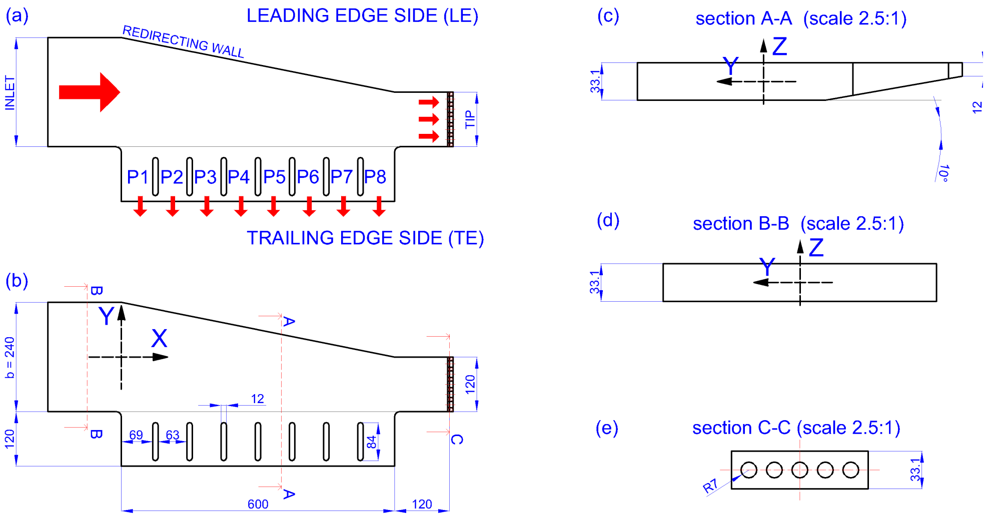

FIGURE 6.6 – (A), (B) Schematic of the test section (configuration G0), (C) channel cross section, (D), Inlet cross section, (E) Tip cross section.

Configuration G1. The adoption of seven inclined *riblets* turbolators in the central part of the channel at the suction-side of the blade defines the configuration G1. The riblets have a 5 *mm* square cross section, which turns in a *blockage ratio* (defined by the ratio of the height of the obstacles with respect to the channel height in percentage) is equal to 15%. Bunker [77], reports that TE ducts can have a blockage ratio of even 25%, therefore the selected rib height is representative of real configurations.

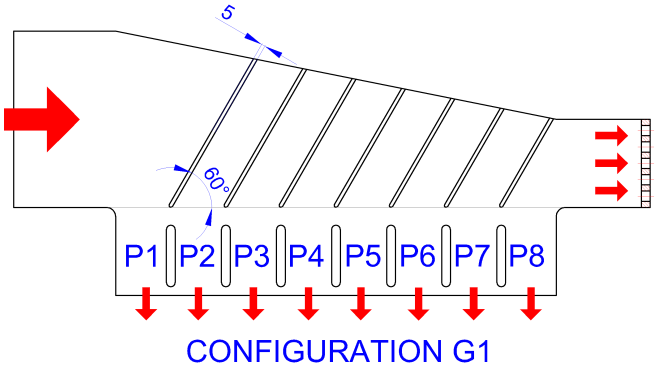

FIGURE 6.7 – Schematic of the test section (configuration G1).

Configuration G2. As for configuration G1, the configuration G2 is obtained by adding to G0 three *riblets* at every *inter-perdestal* discharge channel. The turbulence promoters have a squared cross section and the corresponding blockage ratio of 10% is referred to the channel height at the model inlet. Also, configuration G2 differs from G0 by the fact that the diameter of the five tip holes is reduced to 12.5 *mm*, in order to keep the mass flow ratio distribution constant between the trailing edge discharge region and the channel tip.

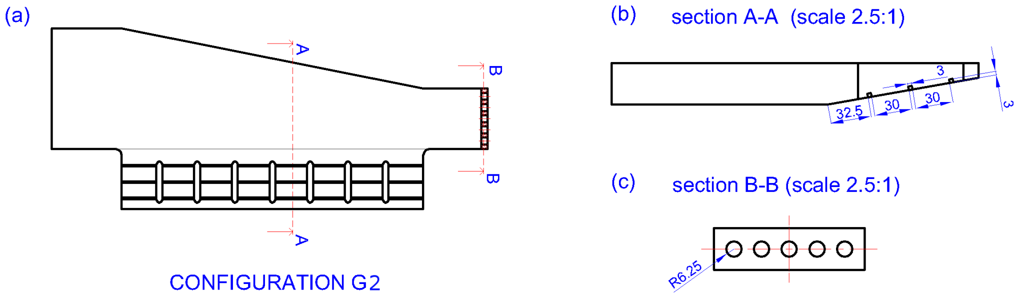

FIGURE 6.8 – Schematic of the test section (configuration G2).

6.3 Test conditions

The experiments have been performed at $Re = (U_b Dh)/\nu = 20000$ and $Ro = (\Omega Dh)/U_b = 0, 0.23$ defined on bulk velocity and hydraulic diameter (Dh=58.18 mm), both computed at the channel entry section. The non-dimensional parameters Re and Ro can be considered representative of real engine conditions. The working fluid was air at ambient temperature and the outlet pressure was equal to the ambient one, as it was in [4], [3], and [5]. As reported in the literature review, this condition, although distant from real engine conditions, allows to perform the experiments in a simple manner and, moreover, ensures that these latter are surely replicable.

Mach number similarity does not need to be fulfilled, since the Mach number is normally below the value for air compressibility effects, as also demonstrated in the work of Facchini and Tarchi [78].

For what concerns the rotating tests, some details of the experimental approach followed have to be discussed.

Channel orientation. The tests under rotation have been conducted with the channel y axis aligned with the direction of the peripheral velocity, as depicted in Fig. 6.6, i.e. in orthogonal rotation. This channel orientation does not differ substantially from a real application, where the blade metal angle at the TE can be as low as 30°, and it has the definitive advantage to simplify the results analysis. Indeed, it maximizes the effects on the flow field due to the channel AR and Coriolis forces in view of the orthogonality between the axis of rotation and the flow principal directions (x and y axis). However, the effect of channel orientation has been numerically investigated in Pascotto et al. [79], showing that for a channel orientation (γ) of 22.5° with respect to the peripheral velocity the flow field does not vary significantly, whereas some differences were found at $\gamma = 45°$.

Outlet pressure. An important observation about the pressure field inside the duct when rotation is taken into account has to be made. Indeed, it should be noted that when the channel is put into rotation the centrifugal forces will act on the coolant flow determining a positive radial pressure gradient from hub to tip. The experimental evidence of this is the variation of the static pressure signal acquired upstream of the orifice flow meter when switching from static to rotating conditions. Under system rotation, a drop of about 180 Pa is observed in that pressure value at Re=20000. Since the mass flow rate is the same for both Ro=0 and 0.23 conditions, the experimentally observed pressure drop is only due to the centrifugal forces. Further support to this observations comes from an estimation made by applying the momentum equation to the PIV data obtained in plane xy. The positive excess pressure from hub to tip turned out to be about 160 Pa, in good agreement with the measured value. This centrifugal pressure gradient turns in a non-uniform delta-pressure at the TE outlet along the radial direction. Moreover, as reported by Armellini et al. [21], in view of the small pressure losses of the channel (about 60 Pa), the attempt to keep the mass flow rate constant at the channel inlet requires to lower the static pressure upstream of the inlet. The outcome is that the pressure drop at the inter pedestal discharge channels close to the hub turns to be opposite with respect

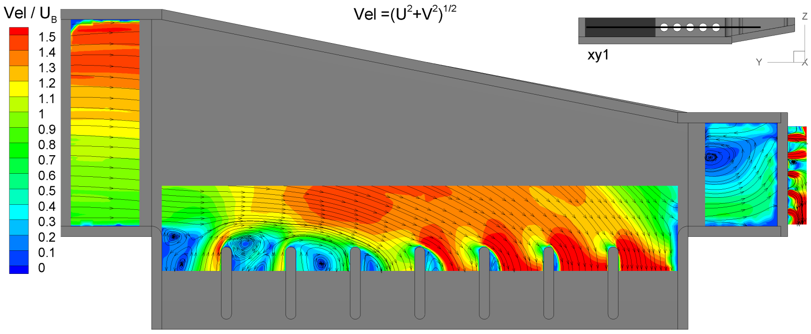

FIGURE 6.9 – Contour of time averaged in-plane velocity modulus C_{xy} and stream-tracers in the symmetry plane xy, from [21]. The stream tracers clearly show the flow ingestion that takes place at the hub.

to the static case and a flow ingestion from outside the channel is observed, as shown in Fig. 6.9. In order to avoid the flow ingestion and more important, to guarantee a meaningful comparison between the data acquired under static and rotating conditions, a polyester fibres filter is placed at the channel outlets (Fig. 6.10) to control the pressure boundary conditions as it follows. The filter produces a pressure drop of about $1200 Pa$ at the outlets at Ro=0, i.e the duct relative pressure is almost uniform with a mean value of about 1200 Pa with respect to the ambient one. When the channel is put into rotation, whatever the outlet conditions are, the centrifugal pressure gradient determines the same delta-pressure between the hub and the tip, i.e. $\approx 180\ Pa$. At this point it has to be observed that the centrifugal excess pressure is only about 15% (180 over 1200 Pa) of the filter pressure losses. This situation is sketched in Fig. 6.11, as it can be seen, the radial pressure ratio distribution between inside and outside the channel can be fairly considered the same between static and rotating conditions, although still different from real engine applications.

Nevertheless, the selected strategy used to control the pressure boundary conditions

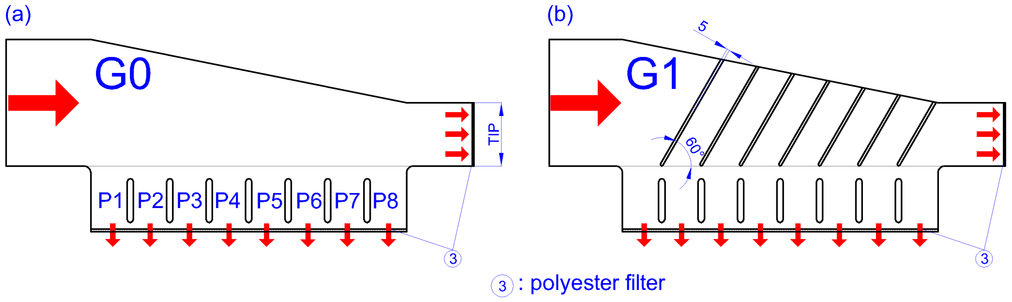

FIGURE 6.10 – G0 and G1 configurations with the polyester filter at the outlets.

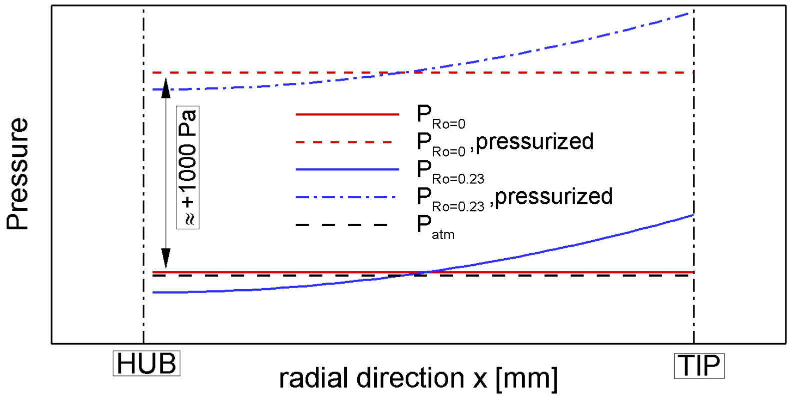

FIGURE 6.11 – Sketch of the internal pressure distribution along the radial direction at Ro=0 and Ro=0.23 with and without the polyester fibre filter applied.

has the definitive advantage to be of easy implementation, it can be well reproduced both numerically and experimentally and it assures almost comparable conditions at varying the Ro number with a negligible effect on the channel fluid dynamics. Therefore, in the present comparison between static and rotating data, the effect of the pressure boundary conditions can be neglected and, conversely, other rotational effects will be put in greater evidence.

Channel eccentricity. Finally it has to be noticed that, being the experiments run in isothermal conditions,the channel eccentricity (namely Rm/Dh, where Rm is the mean radius of rotation) is not a significant similarity parameter since it appears only the Buoyancy parameter Bo. Thus, being the experiments run in isothermal conditions, $Bo = 0 \, \forall R_m$. Further informations on the flow dimensionless parameters can be found in the appendix B. For completeness in the present case $Rm = 700mm$, thus $Rm/Dh \approx 12$.

6.4 Measurement planes

The nomenclature and position of the flow planes selected for the PIV measurements are illustrated in Fig. 6.12, while Tables 6.1-6.4 report the plane positions accordingly with the reference frame adopted in Fig. 6.6.

The inlet conditions were provided by measures in planes xy and xz_{IN}, Fig. 6.12 (a). Then, the flow field investigation was conducted firstly in the xy measurement plane located at z=0. This allowed a preliminary study of the flow field in the symmetry plane referred to the channel region with constant height. Then, to obtain some informations concerning the mass flow rate at the channel outlets, 2D-PIV measurements were acquired in xy_2, which is found at half the TE exits height and in $xz - F1...F5$ at the model tip (Fig. 6.12(d)).

A detail description of the flow field in the Inter Pedestal (IP) passages has been proposed by means of data acquired in planes close to the PS (xz_3, $z/H = 0.44$) and

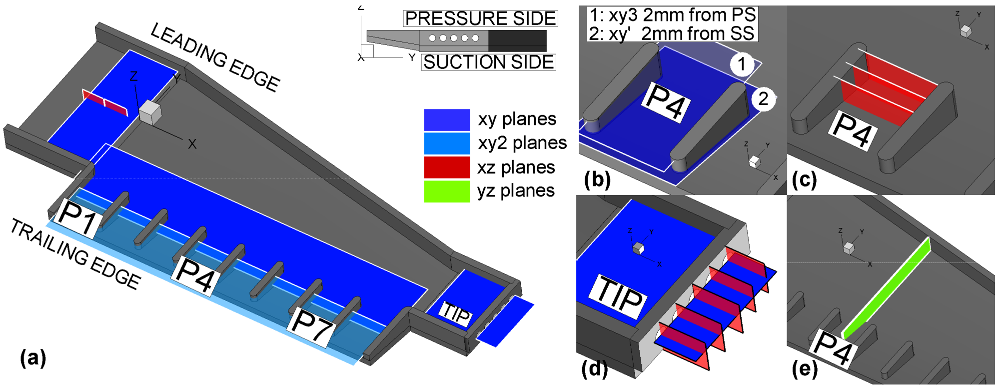

FIGURE 6.12 – Overview of the position of the measurement planes: xy (a), xy and xz in the IP passages (b,c), xy and xz planes at the model tip, and the cross-wise plane yz_{ip} (e).

to the SS (xy'), Fig. 6.12(b) and in the cross-stream planes xz_1, xz_2, and xz_3, these latter by means of S-PIV(Table 6.2, Fig. 6.12(b,c)). For clearness, the IP passages are intended as the channel portions enclosed by two consecutive pedestals. The boundary layer thickness of the flow approaching the TE outlet channel P4 was assessed by means of data acquired on plane yz_{ip}, located at $x = 262.5mm$, Fig. 6.12(e)), which, in the rotating test was extended towards the LE side of the channel. Concerning the rotating tests additional informations were retrieved by 2D-PIV measurements performed in xy_4, $2mm$ close to the SS .

The flow field between the two successive ribs 3^{RD} and 4^{TH} (configuration G1) was described by means of high resolution 2D-PIV measurements in planes xy_{4-G1}, located at mid rib height, and $xz - A$ 2 mm parallel to the LE of the channel, $xz - B$, orthogonal to the ribs and at mid-length of rib 3, and $xz - C$ orthogonal this latter at 10 mm from the 3^{RD} rib head (Fig. 6.13 (a) and Table 6.3).

Furthermore, in G2, the measurement planes xz_1 and xz_3 are located at half the rib thickness, therefore their position is slightly different than the one for G0 and G1 as reported in Table 6.4 and showed in Fig. 6.13 (b). Also the position of plane xy' should be lowered to $1.5mm$ from the SS, since it is located at mid-height of the ribs similarly to xy_{4-G1}.

TABLE 6.1 – xy measurement planes positions.

plane	z position $[mm]$	z/H
xy	0	0
xy_2	10.55	0.31
xy_3	14.55	0.44
xy_4	-14.55	-0.44
xy'	2 mm from SS	n.a

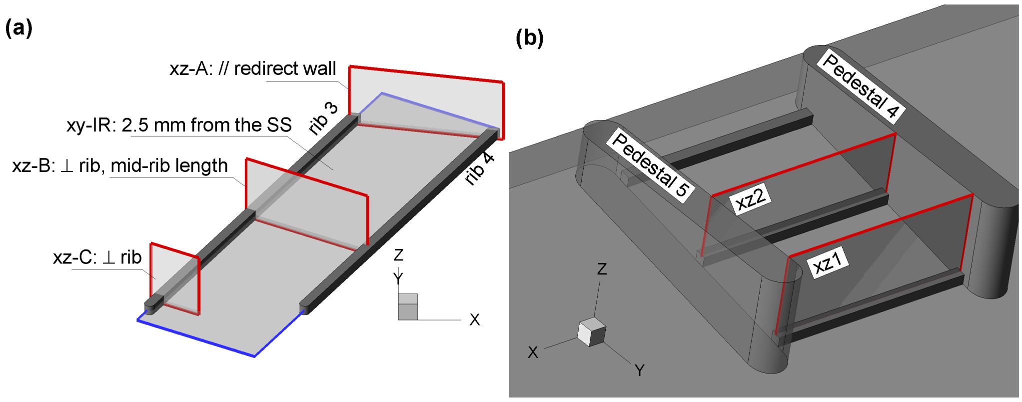

FIGURE 6.13 – Overview of the position of the measurement planes: (a), xy_{4-G1} and xz planes for G1, (b) xz_1 and xz_3 for G2.

TABLE 6.2 – xz and measurement planes positions.

plane	y position $[mm]$
xz_{IN}	0
xz_1	-150
xz_2	-165
xz_3	-180
xz-F1...F5	-104.64,...,-16.36

TABLE 6.3 – xz and measurement planes positions for G1.

plane	position $[mm]$
xy_{4-G1}	at mid rib height z=-14 mm
$xz-A$	2 mm parallel to the LE
$xz-B$	orthogonal to the 3^{RD} at mid-length
$xz-C$	orthogonal to the 3^{RD} 10 mm from the rib head

TABLE 6.4 – xz and measurement planes positions for G2.

plane	y position $[mm]$
xz_1	-153.5
xz_3	-186
plane	position $[mm]$
xy'_{G2}	2 mm from SS

III

Results

7

Performance analysis of the stationary channel

In the following chapter the flow field for the smooth channel configuration is described in detail. The identified flow features will be related to the Nu Number distributions on the suction side wall of the channel (located at $z = -16.55\ mm$). Then the analysis of the HTC enhancements obtained by placing riblets in the radial development region of the channel (G1) and inside the TE outlets are presented and motivated on the basis of the modifications they induce in the flow field. For a clearer reading of the manuscript it should be noted that the flow filed data has been non-dimensioned with respect to the bulk velocity computed at the channel inlet.

7.1 Basic configuration G0

7.1.1 Aerodynamic Behaviour

Inlet conditions

Before reporting the description of the aerodynamic flow field, the inlet flow conditions for the smooth channel are briefly discussed. Figure 7.1 allows to describe the inlet flow by means of velocity and velocity fluctuations profiles extracted at $x = -69.8mm$ from measurement planes xy and xz_{IN}. The y velocity profile is slightly unbalanced towards the TE as a consequence of the blockage caused by the redirecting wall (see Fig.7.2). The related turbulent fluctuations are uniform and equal to 4% of $U_b$with exception of the boundary layers regions ($y < 1.9Dh$ and $y > 1.9Dh$). Figs 7.1 (a) and (b) report the velocity profile and the *r.m.s.* fluctuations along wall-normal direction z, which are typical of a developing flow in view of the short channel entry. The small local perturbations that are measured in the profiles reported in Fig.7.1 are due to the honeycomb filter placed at the channel entry section, which use is however essential to prevent flow separation and to promote flow turbulence. Since the PIV profiles intersect each other at $x = 0$ and $z = 0$, it is possible to compute the local turbulence intensity

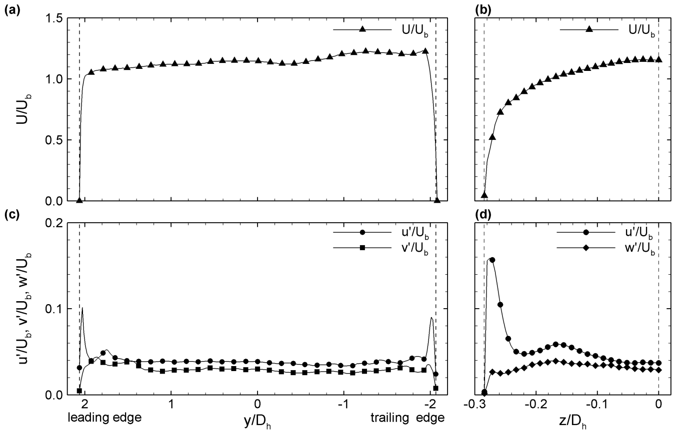

FIGURE 7.1 – Stream-wise U velocity and u', $v'$and w' $r.m.s.$fluctuations profiles at $x = -1.2Dh$ along y (7.1(a),(C)) and z (7.1(b),(d)) directions extracted from measurement plane xy and xz_{IN}.

defined as:

$$T_I = \sqrt{\frac{u'^2 + v'^2 + w'^2}{3}} \tag{7.1.1}$$

which turns to be equal to 3.28%.

Flow field in plane xy

Figure 7.2(a) shows the time averaged contours of the in-plane velocity modulus ($C_{xy} = \sqrt{U^2 + V^2}$) and stream-tracers for the velocity field in the symmetry plane xy. It can be clearly seen that the flow velocity decreases along the radial direction (x), as a consequence of the gradual coolant discharge at the trailing edge. Moreover, at the blade tip and close to the leading side of the channel, a region of separated flow is observed. This latter is a consequence of the geometrical discontinuity between tip and redirecting walls coupled with flow diffusion evidenced by the diverging path of the stream-tracers.

Finally, inside the TE region, flow separation occurs downstream of every pedestal, generating recirculation bubbles which dimension reduces progressively from hub to tip. Indeed, as the fluid flows towards higher radii, it is more aligned towards the direction denoted by $y < 0$ and there-

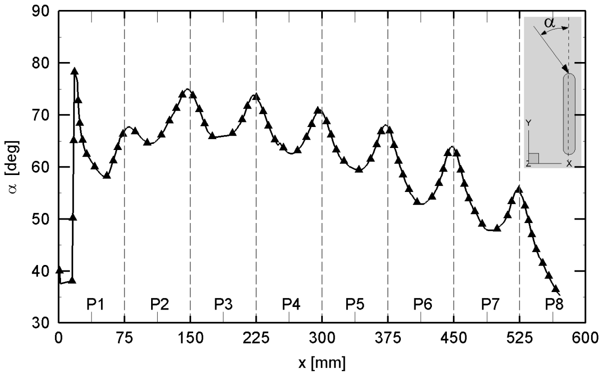

FIGURE 7.3 – Flow angle of attack (α) to the pedestal along a line at $y = -132mm$ in plane xy.

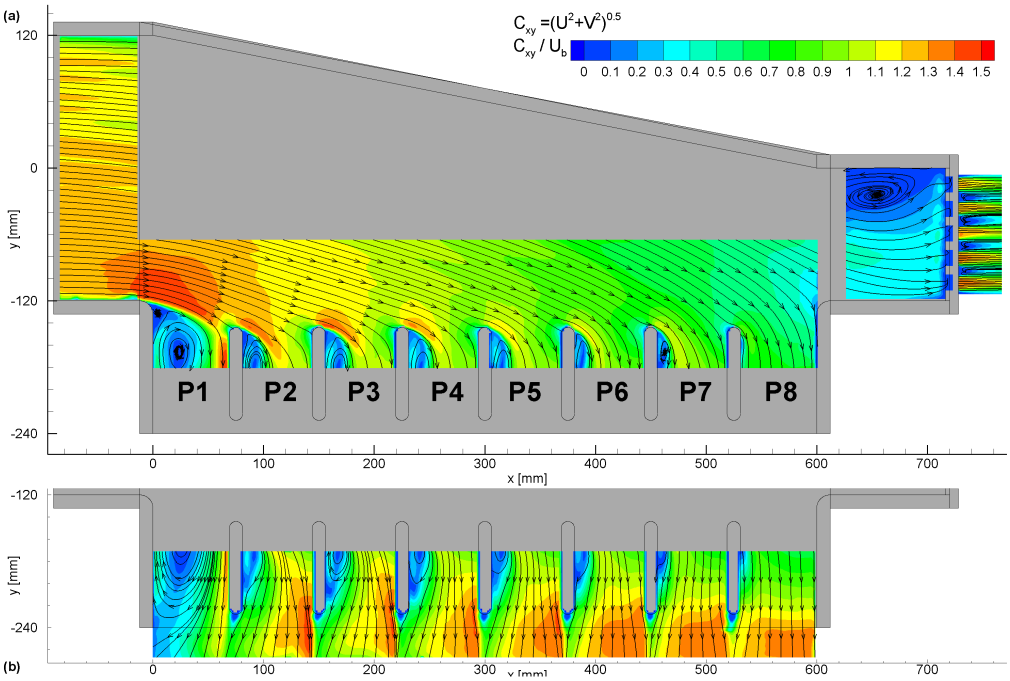

FIGURE 7.2 – Time averaged flow-field on the symmetry plane xy(a) and xy_2(b): contours of in-plane velocity modulus $C_{xy}= \sqrt{U^2+V^2}$ and stream-tracers.

fore it reduces its angle of attack to the obstacle, as shown by the stream-traces path in Fig.7.2(a) and, more clearly, by the plot in Fig.7.3. The flow angle α with respect the y axis, reported in Fig.7.3, has been computed by the velocity components extracted from plane xy, along a line at $y = -132mm$. This location has been selected because it is half way between the pedestals leading edges ($y = -144mm$) and the beginning of the inclined wall ($y = -120mm$). More in detail, it is close to the pedestals but sufficiently upstream that the flow does not feel the deviation imposed by the obstacles, as it is possible to observe from the stream-tracers paths in Fig.7.2(a).

Mass flow distributions

In order to evaluate the mass flow rate discharged at the model tip, the stream-wise velocity maps across each of the five discharge holes have been reconstructed from the velocity profiles (Fig.7.4(a,b)) extracted from measurement planes $xzF1, .., xzF5$ and xy, and then numerically integrated. The working fluid discharged at the tip turned out to be $q_{TIP} 9.9 \mp 0.6\%$ of the total one entering the channel (q_{IN}).

Concerning the TE discharge section, an estimate of the mass flow rate discharged by each IP channel (P1,...,P8 Fig.7.6) can be obtained by analysing three different V velocity profiles, P_{TE1}, P_{TE2}, P_{TE3} extracted from plane xy and xy_2 along x direction for different y positions.

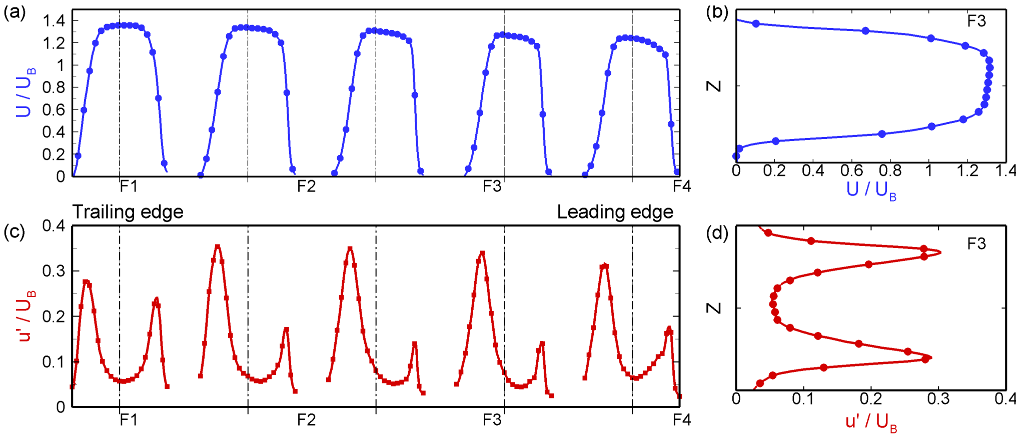

FIGURE 7.4 – Time averaged stream-wise velocity U and rms profiles at the discharge holes for F1-F5 along y axis extracted from measurement plane xy(Fig.7.4(a,c))and for F3 along z axis extracted from planes $xzF1, .., xzF5$ (Fig.7.4(b,d)).

Each profile in Fig.7.5 has been numerically integrated over each inter pedestal channel, and then normalised by the integral of the whole profile, which has been obtained excluding the line segments pertaining to the pedestal walls. Afterwards a scaling factor equal to $1 - q_{TIP}$ was used to refer the results to the mass flow rate at the channel inlet q_{IN}.

The results of the former analysis are presented in 7.6 where the mass flow rate flowing out from each discharge section is plotted. Before commenting the distribution it

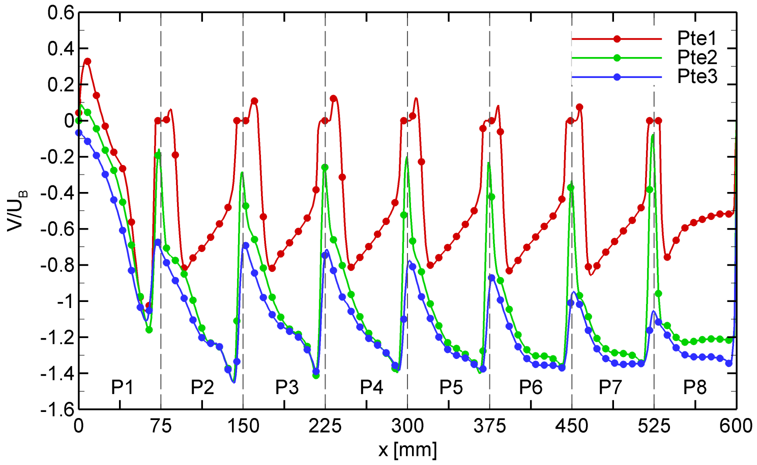

FIGURE 7.5 – Time averaged V velocity profiles at the TE discharge sections along $x$direction extracted from measurement plane xy)and xy_2.

is important to note that the validity of the analysis is sustained by the coherence of the results of the numerical integration of profiles extracted at different y positions. Indeed P_{TE1}, P_{TE2} and P_{TE3} pertain to different channel regions, namely at the beginning , at half way and just outside of each IP channel.

Nevertheless the coherence of the numerical results suggests that the V velocity is rather uniform in the z direction with the exception of the boundary layers. In contrast, an uneven z distribution would turn in computed mass flow shares strongly different depending on the profile position. The flow uniformity in the z direction was moreover confirmed by PIV measurements conducted on plane yz_{ip} located at x=262.5 mm at the TE channel exit of passage P4, which are reported in Fig. 7.7. Ponting the attention to the stream-tracers it is clear that the flow is uniformly aligned towards $y < 0$ and no separation is found. Moreover the time averaged in-plane velocity C_{yz} contours are uniform along the IP channel height, with exception of the boundary layers at the walls. These latter observations allow to consider the numerical integration of P_{TE1}, P_{TE2} and P_{TE3} as a meaningful estimate for the mass flow sharing between the IP channels.

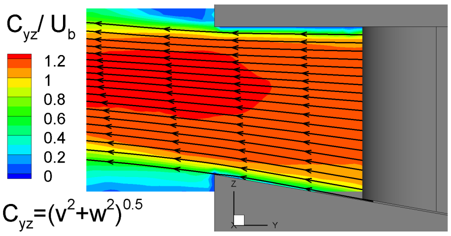

FIGURE 7.7 – Time averaged flow-field on plane yz_{ip} at the TE exit and mid-width of passage P4: contours of in-plane velocity modulus C_{yz}= $\sqrt{V^2 + W^2}$ and stream-tracers.

Once the methodology used has been discussed it is possible to analyse to the computed mass flow distributions, of which two main aspects have to be put in evidence:

- The mass flow rate at the the TE outlets can be considered almost uniform and equal to $12\% of q_{IN}$, with the exception of passage P1.
- The uniform distribution means that the redirecting wall has been properly shaped.

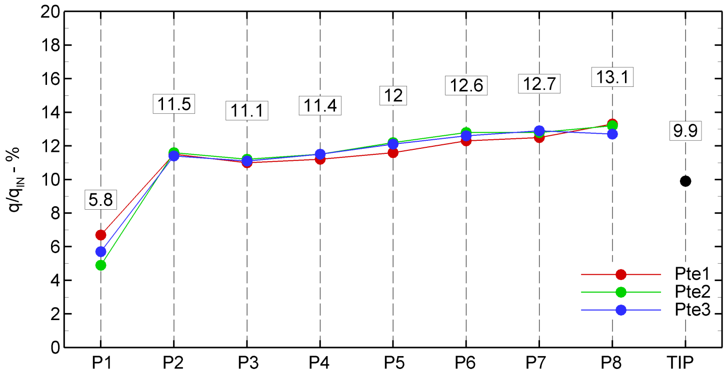

FIGURE 7.6 – Mass flow rate distribution at the different discharge sections of the model for the smooth channel.

This latter issue is not a second order one: obtaining a uniform mass flow rate along the TE region and even inside each IP passage is crucial to ensure uniform flow conditions at the TE exits which is mandatory if the blade is provided with cut-back cooling, as in [80, 9].

3D flow features in the IP outlets

As presented in the following, a 3D flow region was found in the IP passages. With the aim to provide an exhaustive description of this complex three-dimensional flow structure, Fig. 7.8 reports the time-averaged stream-tracers and contour plots of the flow velocity acquired in planes xy', xy_3, xz_1, and xz_3 inside passage P1 (Fig. 7.8(a-d)), P4 (Fig. 7.8(e-h)) and P7 (Fig. 7.8(i-n)).

Considering passage P4, the mean flow path in plane xy_3 highlights a behaviour of the near wall flow substantially different from the one of the core flow. The deviation of the stream-tracers path found in plane xy_3 (Fig. 7.8(f)) near the upstream face of the pedestal at $x = 300\ mm$ suggests the existence of a horse-shoe vortex branch. This latter derives from the deviation of the boundary layer at the junction between pedestal and channel upper wall, and afterwards it is advected by the main stream towards the exhaust. Indeed horse-shoe structures tend to divert the stream-tracers in the xy planes as it can be clearly observed in Fig.7.8 (e, f). A detailed desciption of these 3D flow structures can be found in Devenport et al. [81].

A similar structure must develop also at the opposite pedestal/wall junction at the SS ($z < 0$). The data in the xz_1 and xz_3 planes (Fig. 7.8(g,h)) allow to localise and to size up these vortical structures. On the lower channel side ($z < 0$), the time averaged footprint of the horse-shoe vortex appears as a single structure that extends approximately over half of the passage height. In contrast, on the upper side ($z > 0$) the stream-tracers path suggest a horse-shoe structure made of more than one vortex cell. Indeed, a visual inspection of the instantaneous flow fields revealed that a horse-shoe made of a single and steady primary vortex is found in the majority of the samples at the lower junction (SS). Conversely, an unsteady vortex system made of multiple cells characterises the flow at the upper junction (PS), so that the time averaged stream-tracers in Fig. 7.8(g) are less representative of the actual flow topology. The contour plot of the in-plane velocity in Fig. 7.8(g) suggests that the inter pedestal flow structure can still be considered fairly symmetric with respect to the x axis. Moving towards the channel TE, the time averaged flow path Fig. 7.8(h) is further complicated by the flow acceleration imposed by the narrowing of the channel. The horse-shoe structures are bigger in size and flow exchange between pressure and suction sides regions takes place. Conversely, on the suction side of the pedestal at $x = 225mm$, the strong flow separation that leads to the large recirculating structure does not allow the horse-shoe vortices to develop inside the inter-pedestals passage.

Inside the other inter-pedestal passages, a similar flow behaviour has been observed, with differences only in the dimensions of the separated flow structures as can be observed in Fig.7.8. Considering passage P7, the stream-tracers path in planes xy' and xy_3 presented in Fig.7.8 (i,l) show a weaker deviation imposed by the pedestal upstream face, therefore suggesting a weaker horse-shoe branch. This observation is further con-

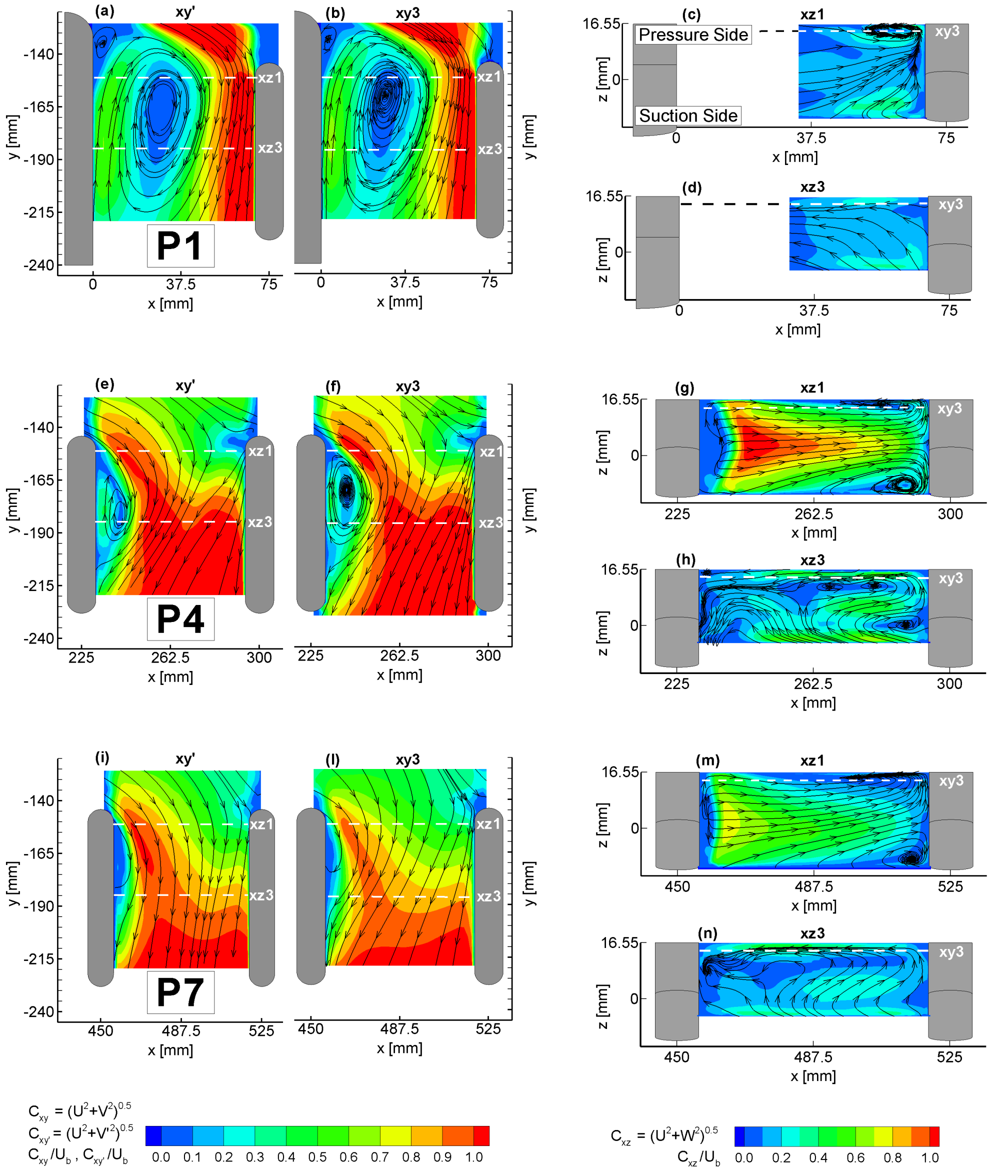

FIGURE 7.8 – Time averaged flow-field in plane xy'(a,e,i), xy_3(b,f,l), xz_1(c,g,m) and xz_3(d,h,n) contours of in-plane velocity modulus and stream-tracers for IP passage P1(a-d) P4(e-h) and P7(i-n).

firmed by the stream-tracers path in plane xz_1 and xz_3, reported in Fig.7.8 (m,n): the secondary structures size is effectively smaller. The reduction of the horse-shoe strength is consistent with a lower flow angle to the pedestal, as shown in Fig. 7.3 and with the lower flow velocity of the flow approaching the pedestal in passages P6-P8 (see. Fig. 7.2).

The same conclusions can be drawn for passage P1, but the motivations are different. Indeed the size of the horse-shoe vortex is related to the characteristics (boundary layer thickness, momentum thickness, turbulence levels...) of the flow approaching the obstacle, as shown by Devenport et al. [81], Fleminget al. [82], and Ballio et al. [83]. For example, passage P1 shows a flow angle to the pedestal comparable with P7, but the velocity levels are much higher. A higher velocity should turn in bigger structures, but the stream-tracers in planes xy' and xy_3 presented in Fig.7.8 (a,b) are almost aligned with the pedestal upstream face as it was in passage P7. Furthermore, the xz_1 and xz_3 measurement planes presented in Fig.7.8 (c,d) let the reader to notice that the horse-shoe size is actually smaller. This behaviour has to be ascribed to the lower momentum thickness in the flow approaching the obstacles as shown by Fleminget al. [82]. This observation is confirmed by Fig. 7.9, where velocity modulus profiles extracted from measurement planes xz_{IN} and yz_{ip} along z are compared. The sense of this comparison relies in the fact that these latter can be reasonably considered representative of the flow conditions at the inlet of passage P1 and P4 respectively. If the momentum thickness θ defined as:

$$\theta = \int_{z=SS}^{z=0} \left[\frac{u}{U_{z=0}} \left(1 - \frac{u}{U_{z=0}} \right) \right] \mathrm{d}y \tag{7.1.2}$$

is computed for the velocity profiles shown in Fig. 7.9 and then the values are compared, it turns out that the momentum deficit for the black line is roughly 20% smaller than the one associated to the green line. This difference is consequent to the flow developing that takes place inside the channel. Considering the velocity profiles in fig Fig.7.9, one thing it has to be addressed: the lower wall position (SS) is different for the two profiles. Indeed the one related to the inlet conditions is extracted from a region where the wall position is located at $z = -16.55$. By contrast, the wall position for the velocity profile extracted at $y = -128mm$ (green line), is located inside the wedge-shaped region of the channel, therefore the SS at this position is located at $z = -15.1mm$. Nevertheless the

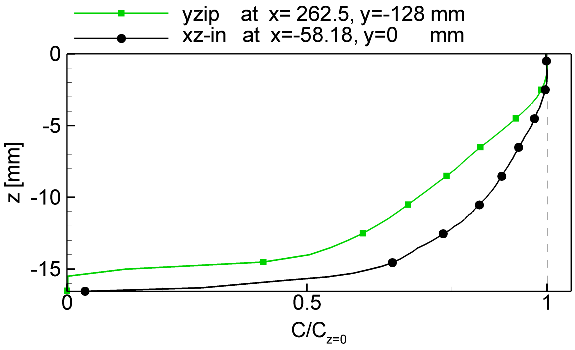

FIGURE 7.9 – Comparison of boundary layer thickness at the channel inlet (black line) and at the IP passage P4 (green line).

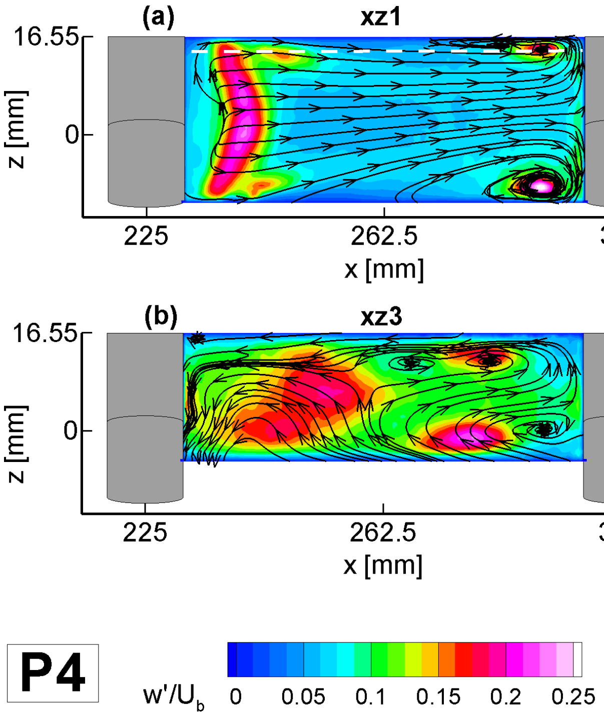

FIGURE 7.10 – w' *r.m.s.* fluctuations and mean stream-tracers on planes xz_1 and $xz_3$for the IP passage P4.

profiles presented can be used to obtain a useful indication about the flow conditions upstream the pedestals number 1 and 4.

From a thermal behaviour point of view, the former analysis allows to hypothesise that existence of the horse-shoe vortices on the pedestals upstream[1] faces should guarantee an efficient flow renewal on the channel walls so determining high heat transfer rates. This hypothesis is sustained also by the the high values of the wall normal fluctuations w' found in in plane xz_1, as depicted in Fig. 7.10(a).

High W *r.m.s.* fluctuations are detected not only in the shear layer of the separation bubble (7.10(a), left) but also in correspondence of the cores of the secondary structures, where w' values greater than 0.25 $U_b$are found. Downstream the IP channel inlet, the w' turbulent fluctuations are increased by the complex interaction of the 3D structures observed (plane xz_3 in Fig. 7.10(b)).

In contrast, inside the recirculation regions, the heat and mass transfer mechanisms should be less effective. Consequently, the development of a non-uniform heat transfer field is expected to be found. This behaviour will be confirmed by the thermal analysis presented in the next section.

---

[1] Upstream denotes the side towards $x < 0$ while downstream the one towards $x > 0$

7.1.2 Thermal behaviour

In the following section the results of the LCT measurements performed by the turbo machinery group of Udine are presented.

Nusselt Number distribution in the main channel

In Fig. 7.11 the Nusselt Number distribution on the SS wall of the channel is reported. The radial development channel region is characterised by a fairly uniform thermal field, with Nu ≈ 50, slightly decreasing in the radial direction. Indeed in this part of the channel the heat exchange mechanism is due to simple forced convection, therefore the reduction of the flow velocity in the radial direction previously observed determines the decreasing Nu Number values. As expected, in the blade tip region a low heat exchange region is found in correspondence of the recirculation region depicted in Fig. 7.2.

Inter pedestal thermal field

For what concerns the TE region, Fig. 7.11, shows that regions with high heat exchange are found on the upstream side of each pedestal, whereas low heat exchange areas are found on the downstream side. This strong thermal non-uniformity, detrimental for the blade integrity in view of the thermal stress, is justified by the flow features previously commented.

The unmistakable correspondence between the horse-shoe branch and high heat exchange is more clear in Fig. 7.12 at page 75. Focusing the attention to passage P4 Fig.

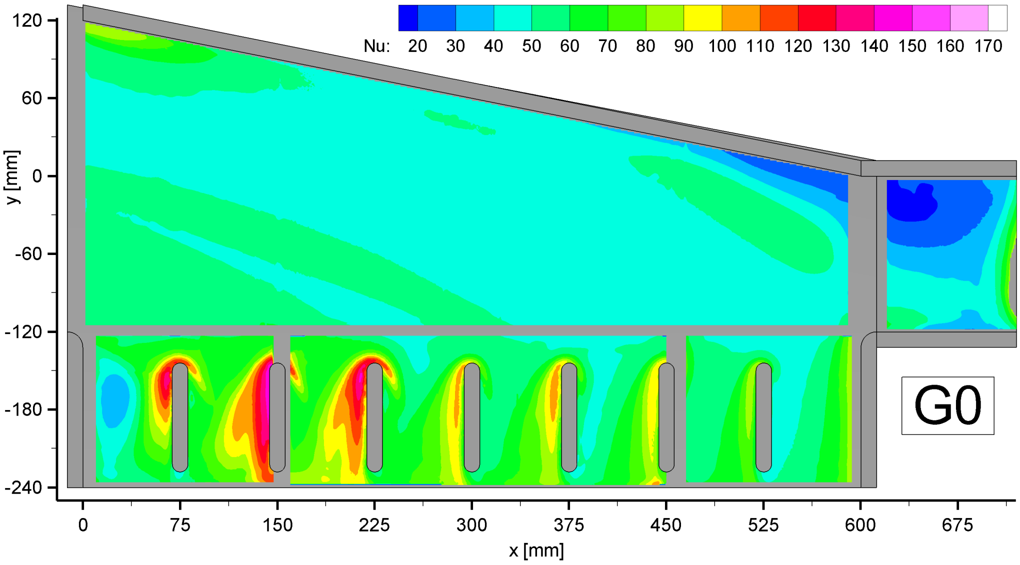

FIGURE 7.11 – Nusselt Number distribution on the channel suction side for configuration G0.

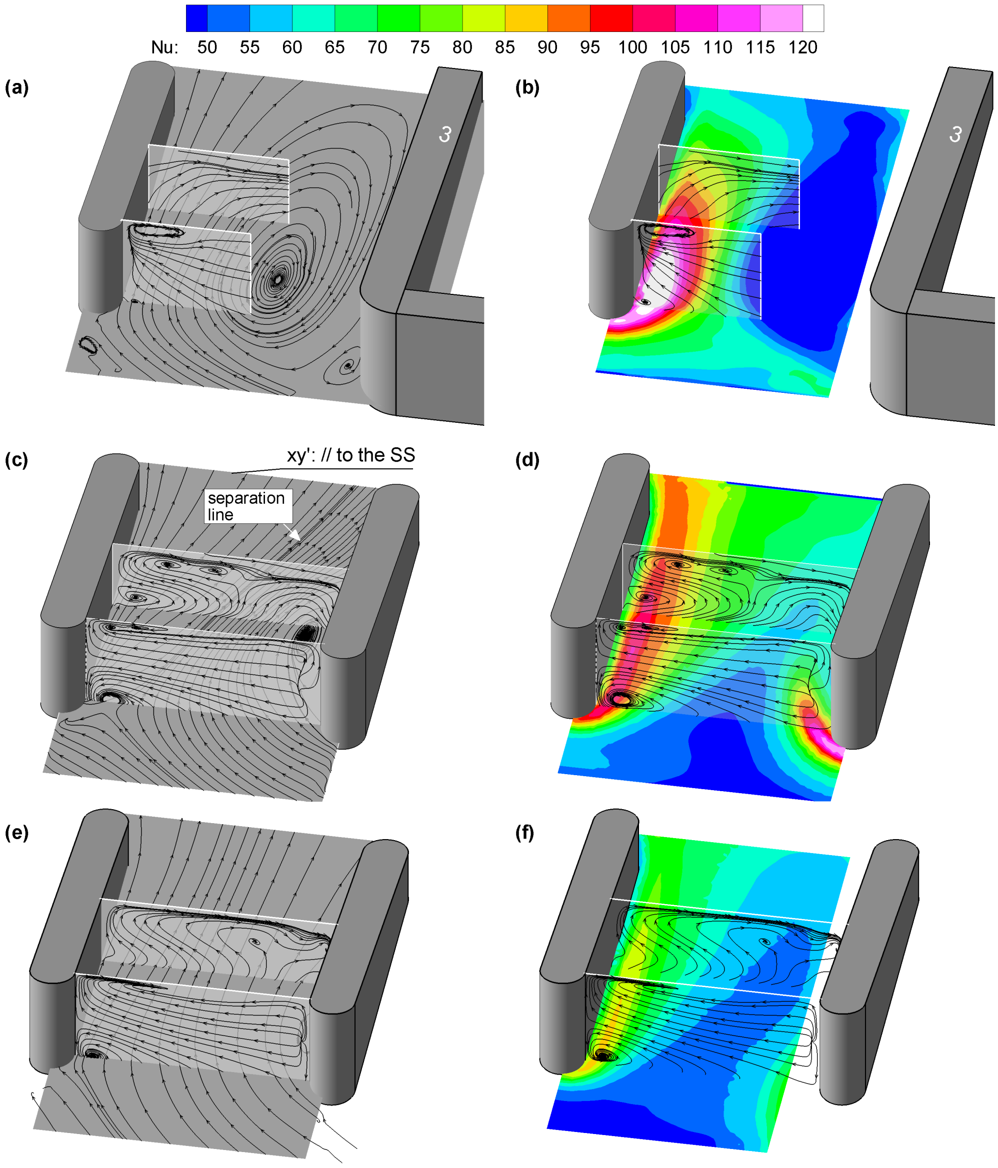

FIGURE 7.12 – Nusselt Number distribution ad the channel suction side for the G0 channel (b,d,f) and time averaged stream-tracers on measurement planes xz_1 and xz_3(a-f) and on xy' (a,c,e) for passage P1 (a,b), P4 (c,d) and P7 (e,f).

7.12(c,d), it is clear that the three dimensional structures, beside increasing the mean turbulence intensity, as observed in sect. 7.1.1, determine an efficient flow renewal mechanism on the upstream side of the obstacles. The maximum HTC values are found near the upstream side of the pedestal, where the vortical structures are deflected towards the channel wall. On the opposite, the lowest HTC values are detected on the IP downstream side, where the recirculation bubble resides, and in correspondence of the separation line that extends across the central part of the passage. These features are specific of each IP passage, however, as commented previously, the extension of the separation bubbles and the horse-shoe strength are different between the passages, so determining similar HTC distributions but with different HTC levels, as it can be observed in Figure 7.11.

Inside passage P1, Fig. 7.12(a,b) reveals an even higher degree of thermal nonuniformity. In fact, the large extension of the dead-water zone implies low HTC values for the most part of the passage. On the other hand, high Nu Number values are found on the upstream side of the pedestal. This condition is more probably due to the higher in-plane velocity C_{xy} (Fig. 7.2(a)) and w' (Fig. 7.8(c,g,n)) than to the strength of the horse-shoe branch, which, as commented in section 7.1.1, can be considered fairly weak.

In contrast, passage P7 Fig. 7.12(e,f) shows a less intense Nu peak as a consequence of the weaker horse-shoe branch, as observed in section 7.1.1. In fact, at the model tip the flow velocity is lower than at the hub (Fig. 7.2(a)), which turns in a less effective convection mechanism and smaller 3D structures.

Highlighted features of configuration G0

In conclusion the analysis performed for configuration G0 highlights that:

- a separation bubble, which size is decreasing in the x direction is found on the down stream side of the pedestal;
- a dead water zone at the blade tip is generated by the geometrical discontinuity between the channel walls;
- the flow shares at the different outlets turned out to be almost uniform, with the exception of passage P1;
- the Nu Number levels in the radial development region of the channel decrease in the x direction in view of the decreased flow velocity;
- low and high HTC values are found in the IP outlets on the down-stream and up-stream regions, respectively, as a consequence of the 3D features of the flow field;
- the dead water zone at the model tip implies low Nu Number levels.

7.2 Configuration G1

In the following the aero-thermal behaviour of the rib-roughened channel is presented.

7.2.1 Mean flow field on symmetry plane xy

Figure 7.13 reports the contour plots of the time averaged in-plane velocity C_{xy} and the stream-tracers in plane xy for configuration G1.

The presence of the ribs does not substantially alter the mean flow field in plane xy: dead water zones are still found on the down-stream side of each pedestal and at the model tip as previously observed for G0. Moreover, the in-plane velocity C_{xy} has comparable modulus and direction with respect to the smooth channel, as it can be observed from the comparison of Figs. 7.13 and 7.2. The angle of attack to the pedestals measured for the two configurations is also fairly the same: it increases from passage P1 to P3 and than decreases in the radial direction.

However, a more careful insight on the data set reveals some small differences. The comparison of the angle of attack to the pedestal along a line at $y = -150\ mm$ for G0 and G1 , Fig. 7.14, reveals that an appreciable lower angle of attack is found in the IP channels at the hub.

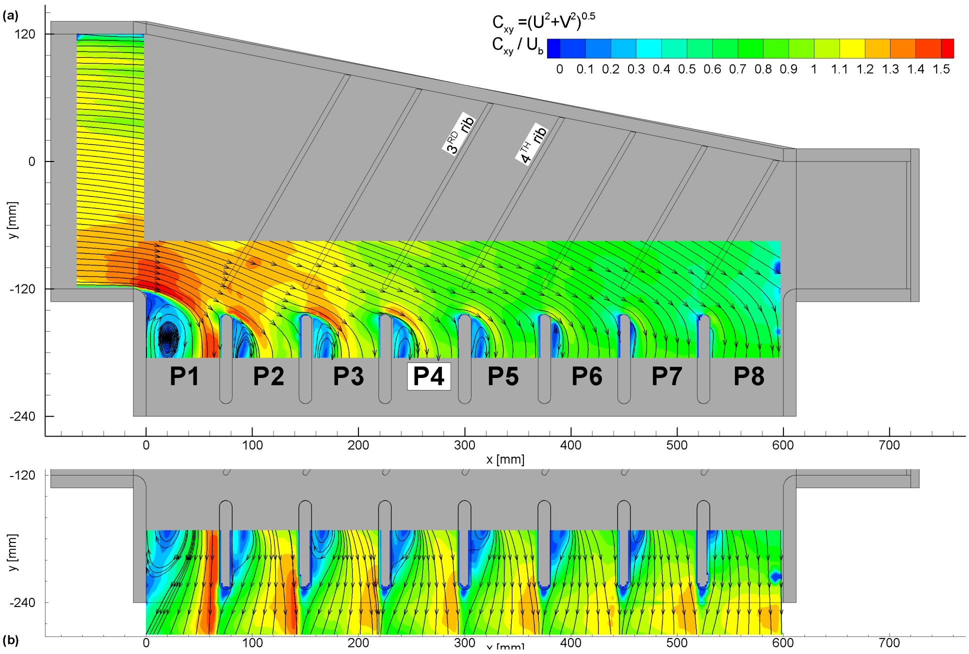

FIGURE 7.13 – Contours of time averaged in-plane velocity C_{xy} and stream-tracers on plane xy for G1 configuration.

Consequently the separation region in passage P1 is reduced in size, with respect to G0, as it can be observed by the comparison of the V velocity profiles in passage P1 at $y = -150mm$, Fig. 7.15. This latter has to be ascribed to the blockage caused by the 1^{ST} rib that redirects the flow towards $y < 0$ at the IP passage P1. Now, if the mass flow ratio distribution for G1 is computed as it has been done for G0 in section 7.1.1, a higher mass flow ratio pertaining to P1 has to be found, as shown in Fig. 7.16. Moreover, the analysis revealed that about the 8% of the total mass flow ratio (q_{IN}), flows out from the 5 holes at the model tip. Keeping in mind that the diameter of these latter is equal to that in G0 and that the turbulence promoters increase the blockage in the x direction in favour of the TE outlets, the changes in the mass flow ratio shares can be straightforward justified.
Another observation can be addressed to the $r.m.s.$ fluctuations of the in-plane velocity components, reported in Fig. 7.17. A significant increase of the turbulent fluctuation has been observed, although the time averaged flow field in the symmetry plane showed little changes between G1 and G0. Indeed, the release of coherent structures that takes place in correspondence of the shear layer developing downstream each rib, as shown by Casarsa et al. in [84], turns in an higher turbulent activity in the symmetry plane xy as well.

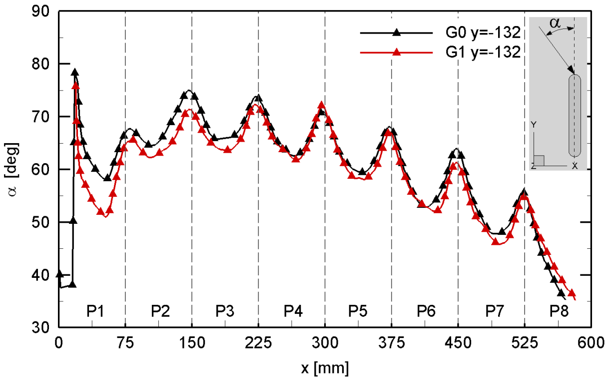

FIGURE 7.14 – Comparison of the angle of attack to the pedestals along a line at $y = -132\ mm$ between G0 and G1 configuration.

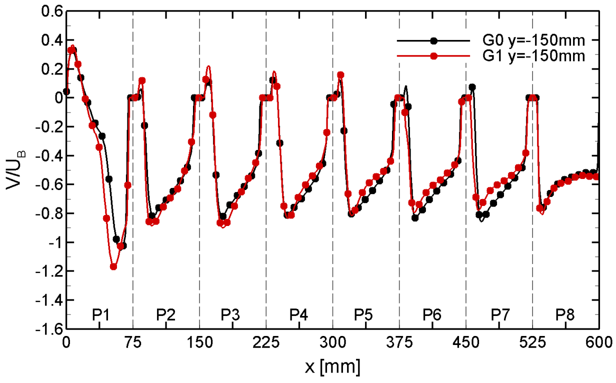

FIGURE 7.15 – Comparison of time averaged v̌elocity profiles extracted along a line at $y = -150\ mm$ from plane xy for G0 and G1.

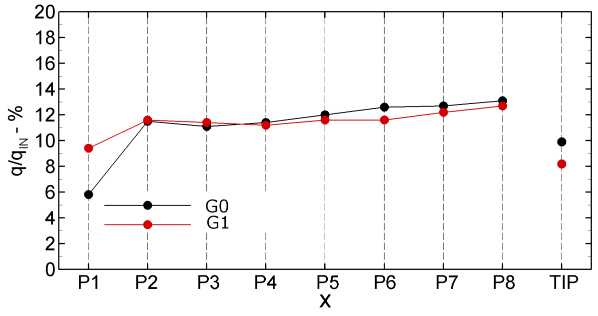

FIGURE 7.16 – Percentage of q_{IN} at the different exhaust section for G0 and G1 configurations.

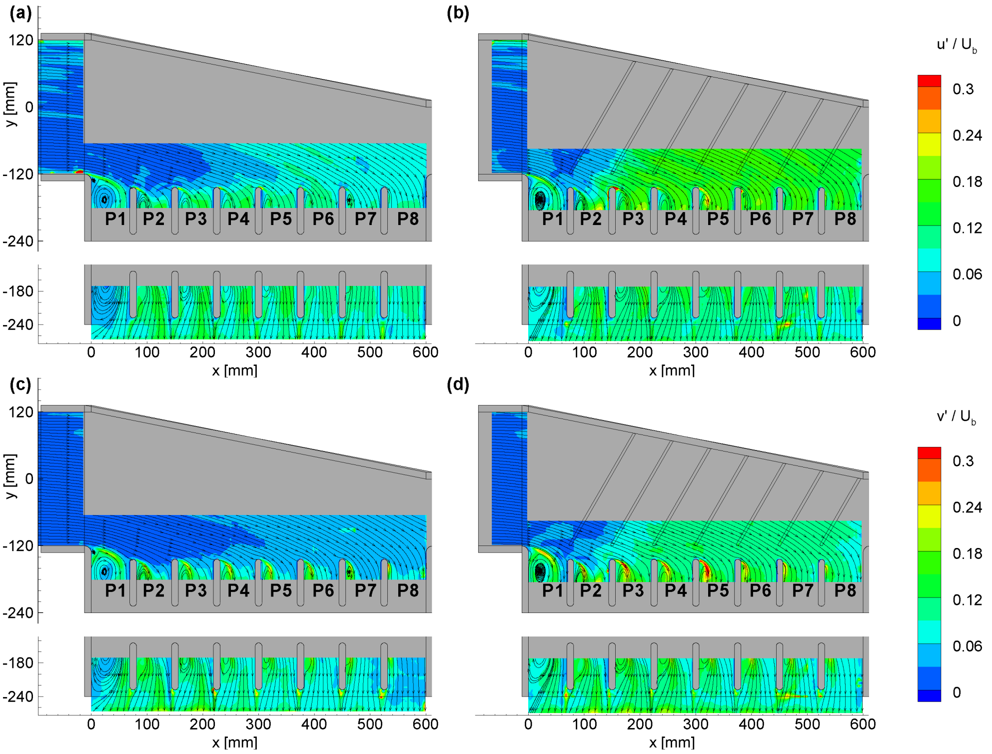

FIGURE 7.17 – Comparison of $u'$and v'on measurement planes xy (a,c) and xy (b,d) for G0 (a,c) and G1 (b,d) configurations.

7.2.2 Thermal field

Although the time averaged flow field at middle channel height turned out to be similar to the one of G0, the LCT measurements revealed a significant increase of the Nu Number values on the SS wall, as reported in the following.

Radial development channel

Figure 7.18 reports the Nu distribution on the SS for configuration G1. The effect of the-rib-roughened surface is clear: a significant augmentation of the heat transfer is found with respect to the smooth wall (Fig. 7.11), with high Nu values found in the regions downstream of each obstacle. The position of the Nu maxima corresponds to the reattachment point, as clearly shows Fig. 7.19. This latter reports the Nu number distribution on the SS wall of the channel between the 3^{RD} and 4^{TH} rib and the time averaged stream-tracers from 2D-PIV measurements conducted on planes *xy-IR*, $xz - A$, $xz - B$ and $xz - C$. Lower Nu number values are found close to the upstream rib (i.e. rib 3), where the sudden expansion downstream of the rib and the consequent flow separation lead to the appearance of a strong shear layer and a recir-

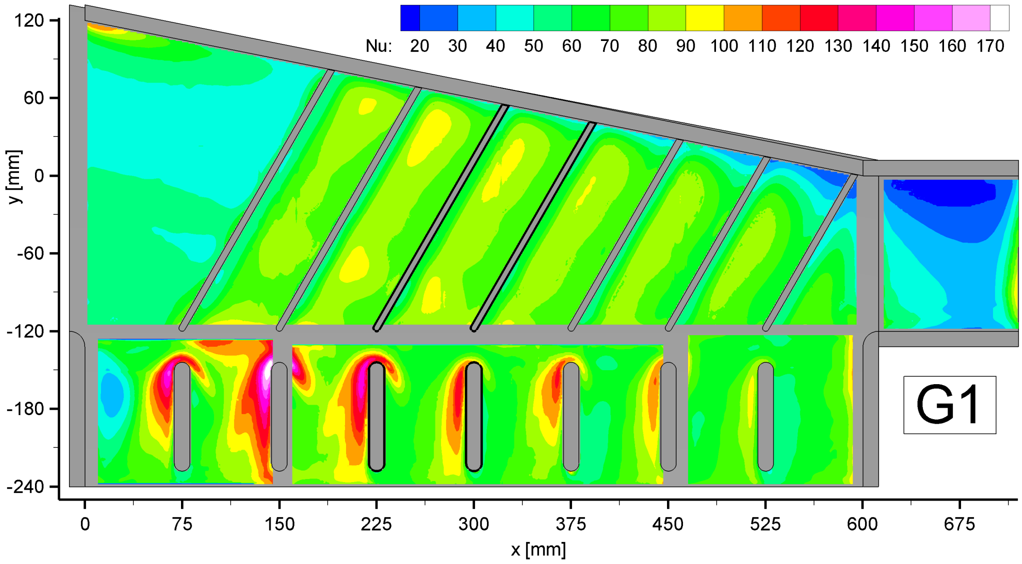

FIGURE 7.18 – Nusselt Number distribution ad the channel suction side for G1 configuration.

culation region. After the reattachment point, a new boundary layer develops determining lower Nu number values than the maximum detected, but still far above the ones pertaining to the smooth wall (Fig. 7.11). A clear description of the flow field in a square rib-roughened duct has been made by Casarsa et al. [84], who found a correlation between $<u',w'>$, i.e. the cross component of wall-normal and stream-wise fluctuations, and the Nu number normalised with respect to the one of the smooth wall. The correlation was justified by the fact that the Reynolds stress component $<u',w'>$ is strictly related to the development of coherent structures with mean vorticity aligned with the flow direction. These latter are originated by the separation in correspondence of the ribs and then convected down-stream, ensuring a constant mass exchange between the flow layers and, consequently, increasing the HTC. Figure 7.20 compares the Reynolds stresses component $<u',w'>$ extracted along a line at $1mm$ from the SS from measurement plane $xz - B$ and the normalised Nu number at the wall on the same direction. The two quantities

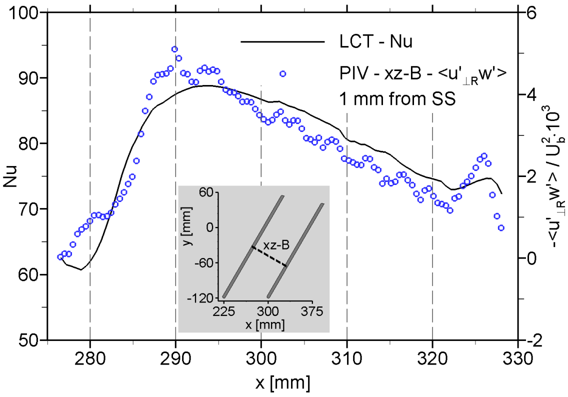

FIGURE 7.20 – Comparison with the normalised Nusselt Number profile at the SS and $<u',w'>$ profile extracted at $z = -15.55\ mm$ from plane $xz - B$.

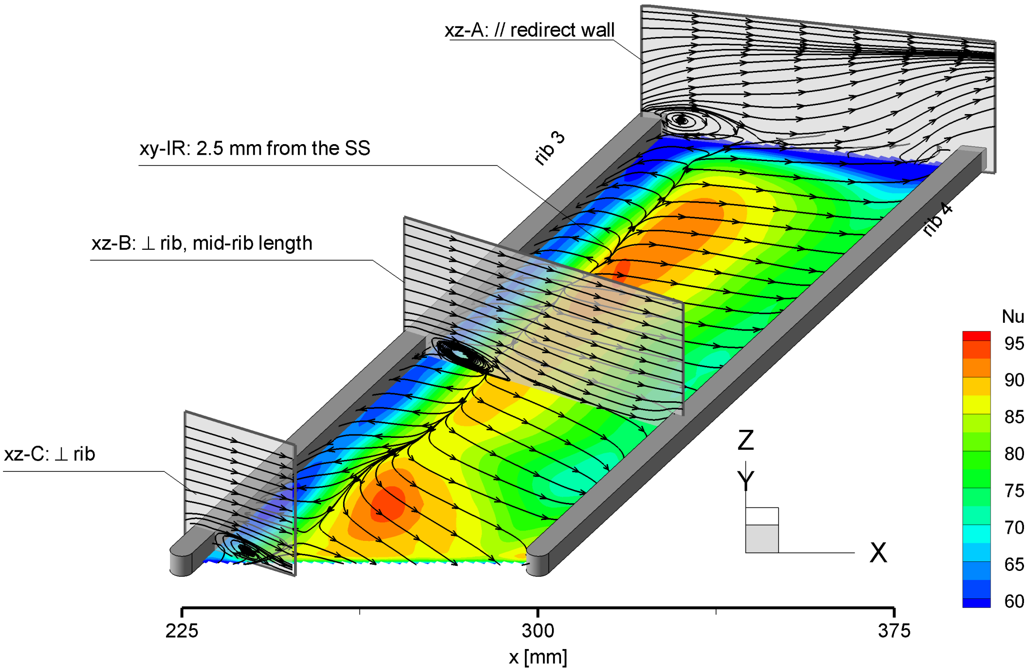

FIGURE 7.19 – Nusselt Number distribution detail at the SS between the 3^{RD} and 4^{TH} rib and time averaged stream-tracers on planes xy-IR($2mm$ from SS), $xz-A$, $xz-B$ and $xz-C$, respectively $10mm$ from the beginning of the 3^{RD} rib, at the middle of the 3^{RD} and $2mm$ from the redirecting wall.

show a similar trend, with a maxima in correspondence with the reattachment point, as found by Casarsa et at. [84]. However, in the present case, a slight mismatch is observed. This latter has to be ascribed to the channel geometry: indeed, the gradual discharge along the TE outlets determines a variable Re Number, which in turn does not allow to easily determine an unambiguous value for U_b along the radial direction used for data normalization.

TE region

The comparison of Fig. 7.21 (a) and (b) reveals that the adoption of ribs in the main channel also has a positive effect on the TE outlets: an increase of the Nu number levels over the central portion of the passage P4 (i.e. at around $-180 < y < -120$) can be noticed. A the same time the Nu peak in correspondence of the pedestal upstream face is enhanced as well. These features can be explained only with a deep view on the flow approaching the pedestals, and is not just with the increase of U' and V' shown in Fig. 7.17. More in detail, the global increase of the heat transfer mechanisms has to be related to an augmentation of the cross component of wall-normal and stream-wise fluctuations, i.e. $<v',w'>$[2], as reported previously. This observation was confirmed by

---

[2] It should be remembered that the flow in the IP sections is roughly aligned with the y direction.

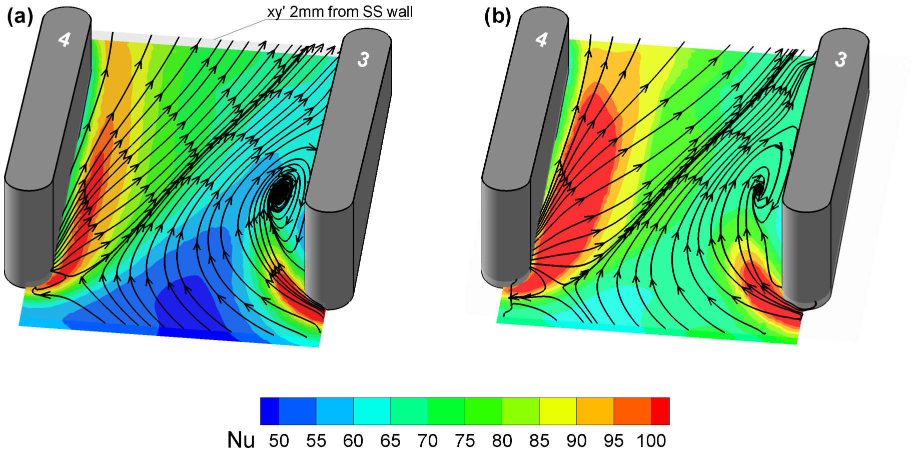

FIGURE 7.21 – Contours of Nu number on the SS wall and time averaged stream-tracers in measurement plane xy' for G0 (a) and G1 (b) across IP passage P4.

dedicated STEREO-PIV measurements in plane yz_{ip} which lays in the middle of passage P4: the z profiles at $y = 128\ mm$ reveal indeed a significant increase of $<v',w'>$, Fig. 7.22(b).

Besides this, the motivation of the Nu peak enhancement has still to be addressed. In section 7.1.1 the connection between the Nu maxima and the presence of an horse-shoe branch has been described. Following that analysis, if higher Nu values are found an increase of the strength of the coherent structures could have occurred. This hypothesis can be proven observing that stream-tracers in plane xy' are more diverted in the region towards the up-stream face of the 4^{TH} pedestal in G1 (Fig. 7.21(b)) than for G0 (Fig. 7.21(a)).

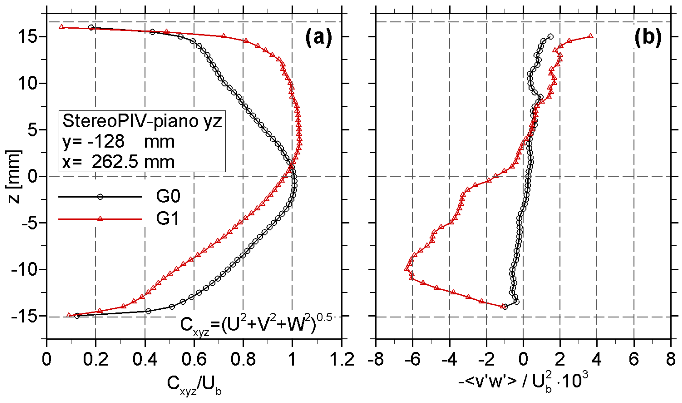

FIGURE 7.22 – Velocity (a) and $<v',w'>$ (b) profiles for G0 and G1 extracted along a line at $y = -128\ mm$ from yz_{ip}.

Furthermore, Figure 7.23 reports the mean stream-tracers and the *r.m.s.* of the in-plane vorticity ω in measurement planes xz_1 and xz_2 for the two configurations, showing that the horse-shoe branch is without doubt bigger in size for G1 than for G0. Once again, the motivation of this behaviour has to be referred to the presence of the ribs in the radial development part of the channel. The blockage caused by these latter determines

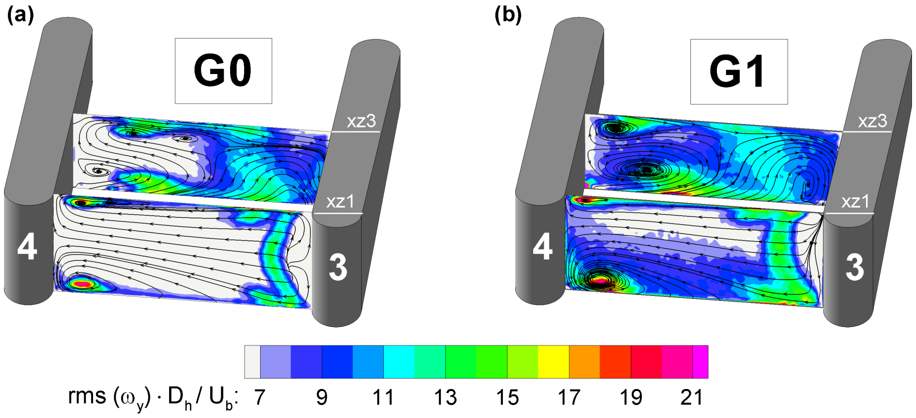

FIGURE 7.23 – Stream-tracers and ω' on measurement plane xz_1 and $xz_3$for G0 (a) and G1(b).

an higher boundary layer thickness at the SS wall in the flow approaching the pedestals as reported in Fig. 7.22(a). Keeping in mind that size of these coherent structures is strictly related to the boundary layer thickness as described by Ballio [83], it follows that an higher boundary layer thickness turns in an increase of the size of the horse-shoe vortices, as it has been observed.

Finally, another interesting observation can be drawn from Fig. 7.23: the increased levels of ω' suggest an higher level of instability of the position of the horse-shoe branch, causing an even higher level of mixing between the flow layers than the one due to a more stable condition, whit benefit to the heat transfer.

Highlighted features of configuration G1

In conclusion the analysis performed for configuration G1 highlighted that:

- the presence of the ribs, beside increasing the mass flow ratio at the IP channel P1, does not vary significantly the flow field in the symmetry plane xy;
- a significant increase of the Nu values is found at the SS wall in the radial development channel;
- a fairly good agreement with the correlation proposed in [84] was found between the normalized Nu number distribution and the cross component of wall-normal and stream-wise fluctuations;
- the increased cross component of wall-normal and stream-wise fluctuations determine an increase of the HTC also inside the TE outlets;
- the increased boundary layer thickness yields to a stronger horse-shoe branch on the pedestal upstream-side which, in turns produces higher Nu peaks than the one observed for G0.

7.3 Configuration G2

In the following the flow features and the HTC increase determined by the adoption of ribs in the TE channels are reported in detail.

7.3.1 Mean flow field

Figure 7.24 reports the contours of time averaged in-plane velocity C_{xy} and the stream-tracers in plane xy for G2. Again as for G1, the maps show little differences with respect to G0. Indeed the in-plane velocity modulus and direction are comparable to the ones measured for G0 and the dead water zones at the model tip and on the down-stream side of the pedestals observed in the smooth channel are still present in G2. However, the size of these latter is smaller than the one found in G0 and, as a consequence of the blockage introduced by the ribs, considerably higher in-plane velocity levels are found at the TE outlet in plane xy_2 as shown in 7.13 (b).

Going into details, the angle of attack computed along a line at $y = -128\ mm$ shows small differences with respect to the one observed for configuration G0 (Fig. 7.25). It can be noticed that a lower angle of attack is found for passages P1 P6, P7 and P8. This behaviour coupled with the blockage caused by the riblets in the IP channels, determines a reduction of the extension of the dead water zones at the TE passages, as it was observed

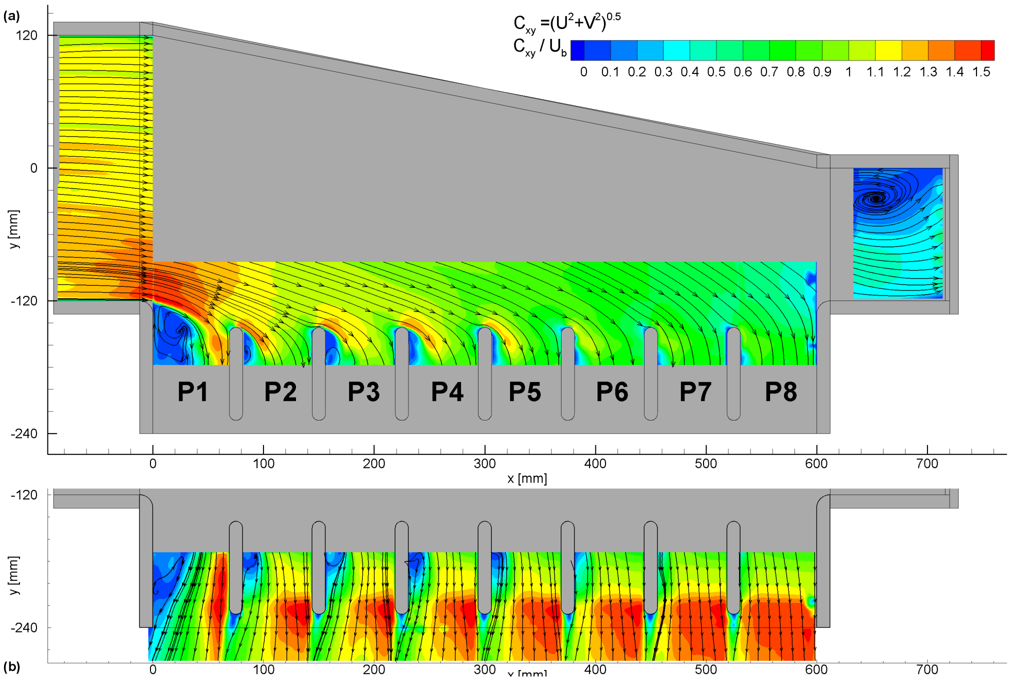

FIGURE 7.24 – Time averaged flow-field on the symmetry plane xy(a) and xy_2(b): contours of in-plane velocity modulus C_{xy}= $\sqrt{U^2 + V^2}$ and stream-tracers for configuration G2

for G1, the most significant reduction is found in passage P1. Figure 7.26 supports these observation, and moreover shows the V velocity peak is closer to each pedestal down-stream face in G2 than in G0, i.e. an overall decrease of the separation bubbles on the downstream side of the pedestals. It should be noted that the time averaged stream-tracers in correspondence of the separation bubbles are less representative of the instantaneous velocity fields in view of the strong 3D features of the flow the TE outlets yielded by the adoption of ribs in this channel portion.

Concerning the mass flow ratio distribution, in section 6.2, it has been reported that the diameter of the discharge holes at the model tip were reduced from 14 to 12.5mm, to re-establish the mass flow ratio split to the values found in G0 between the tip (10% q_{IN}) and the TE (90% q_{IN}).

Indeed, it should be noted that placing the riblets inside the IP passages yields to an augmentation of the pressure drop across the TE channels, therefore an increase of the pressure losses at the model tip is required to keep constant the mass flow ratio at the tip outlets between G0 and G2.

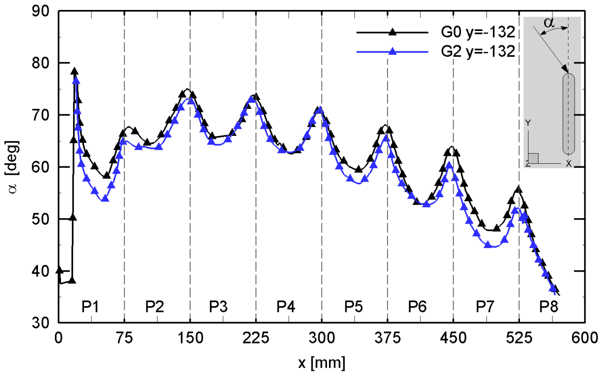

FIGURE 7.25 – Comparison of the angle of attack along a line at $y = -132$ mm between G0 and G2 configuration.

Unfortunately any information regarding the mass flow shares between the different IP channels can be addressed with a satisfactory accuracy. As it will be cleared in the following , the strong 3D features of the flow field inside the IP passages yielded by the ribs make the hypothesis made in section 7.1.1 for G0 to be non applicable in this case. Nevertheless, a qualitative observation can be drawn observing Fig. 7.26: provided that the V velocity profiles for the two configurations are similar to each other, and provided that in the case of G0 the mass flow ratio distribution across the TE was fairly uniform, a certain degree of uniformity could be expected also for G2. However to obtain a precise estimate of the mass split dedicated and time consuming measurements are required.

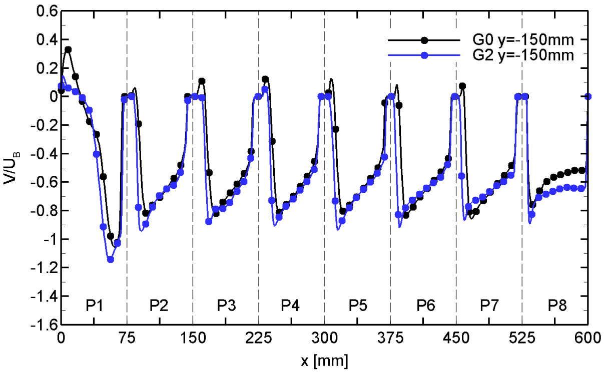

FIGURE 7.26 – Comparison of v̌elocity profiles extracted along a line at $y = -150$ mm from plane xy for G0 and G2.

7.3.2 Thermal field

Figure 7.27 presents the Nu Number distribution detected for G2 configuration.

As it could be expected, the adoption of ribs turbulators only at the TE outlet channels has an impact limited to these regions. Indeed, in the radial development and in the tip region of the channel, the Nusselt distribution does not show any significant difference with respect to the configuration G0. On the opposite, in the TE region, a noteworthy increase of the HTC rates is found. This latter is due to the successive flow separation and reattachment at the SS wall caused by the ribs, as described below.

Effects at the TE outlets

Figure 7.28 shows a detail of the flow field in plane yz_{ip} and the thermal field at the SS across channel P4.

Concerning the PIV measurements here reported, an issue has to be briefly addressed. To overcame the viewing constraints, the flow field was retrieved by means of S-PIV, however, beside the nominal resolution of 0.5 mm, the result is less satisfactory than those obtained on a similar plane for G1 (see Fig.7.19). The motivation of this relies in the rib-height which is almost the half of the ones adopted in G1. Therefore this latter yields to smaller separation structures which would require a considerably higher resolution to be well described by PIV measurements. Nevertheless, data are sufficiently resolved to make possible to observe that the Nu peak position along the line at $x = 262.5$ mm is fairly at the same position of the reattachment point. Moreover, Fig. 7.28 shows also that the thermal field over each IP passages is not uniform in the span-

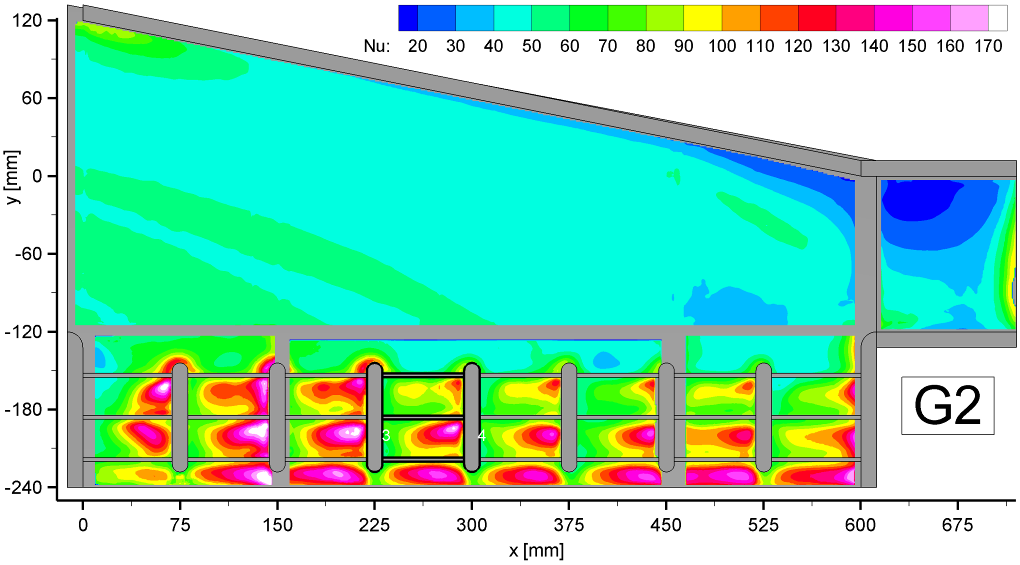

FIGURE 7.27 – Nusselt Number distribution ad the channel SS for G2 configuration.

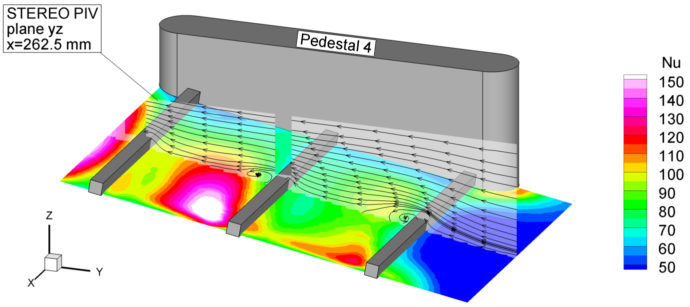

FIGURE 7.28 – Contours of Nu Number on SS wall and and time averaged stream-tracers on plane yz_{ip}.

wise direction (i.e. x) particularly downstream the first and second rib, with maxima localised on the upstream side of the pedestal (Figs. 7.27 and 7.31(a)). This behaviour is due to the coupling of the rib induced separation and the deviation imposed by the pedestals as described in the following. The PIV measurement conducted in plane xy' at $1.5mm$ from the SS reported in Fig. 7.29 allow to observe that the flow layers near the wall are deflected towards the hub (i.e. $y < 0$). At the same time, an horse-shoe vortex branch is developing at the junction between the 4^{TH} pedestal and the channel wall as proven by the S-PIV measurements in plane xz_1 reported in Fig. 7.29(c). The coupled effect of the mixing induced by horse-shoe branch and the flow reattachment past the first and second rib determines an HTC enhancement of the up-stream side of the pedestal. By contrast, since a recirculation bubble is still present on the down-stream side (Fig. 7.24), lower Nu values have to be expected in this region. For the above reasons, an uneven Nu distribution must be found past the first rib, as shown in Fig. 7.31(b).

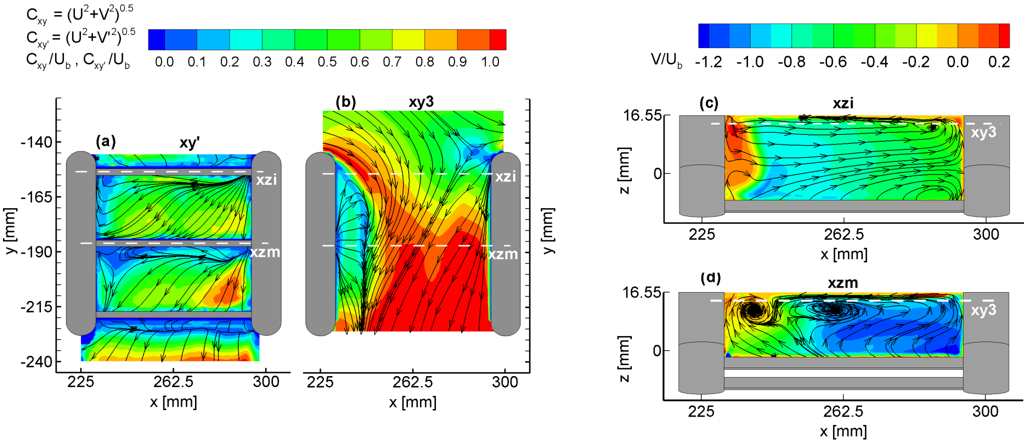

FIGURE 7.29 – Time averaged flow-field in xy'(a), xy_3(b), xz_1(c) and xz_3(d) contours of in-plane velocity modulus and stream-tracers for IP passage P4.

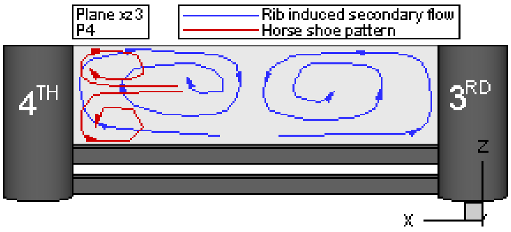

FIGURE 7.30 – Scheme of the secondary flow patterns

Further on in the passage the horseshoe becomes weaker: the stream-tracers on xz_3, Fig. 7.31 (d) do not reveal the presence of coherent structures on the upstream face of the pedestal. This behaviour results from the coupling of two different secondary flows: the rib induced one (further informations in [84]) and the horse-shoe vortex, whose patterns are sketched in Fig. 7.30. More in detail, the horse-shoe branch originated at the junction between the 4^{RD} and the SS wall ($z = -16.55\ mm$) has a vorticity opposite with respect to the rib induced secondary flow. Between the two structures the rib induced one is the strongest and annihilates the other. This observation is supported by the stream-tracers path in plane xz_3, which resembles the one depicted in Fig. 7.30, besides, in this case, one of the two vortex cores (i.e. the one towards the pedestal upstream face) is found not in the corner but in the middle of the cross section. This condition is probably due to the fact that the flow approaches the turbulators after a redirection and not along the direction normal to them as it was in [84].

Concerning the downstream side of the pedestal, the interaction between the separation bubble and the strong flow perturbations caused by the turbolators convects the coolant towards the PS as shown by Figs. 7.29(b,d) and determine a recirculation region in the corner between the downstream face of the 3^{RD} pedestal and the PS wall. It

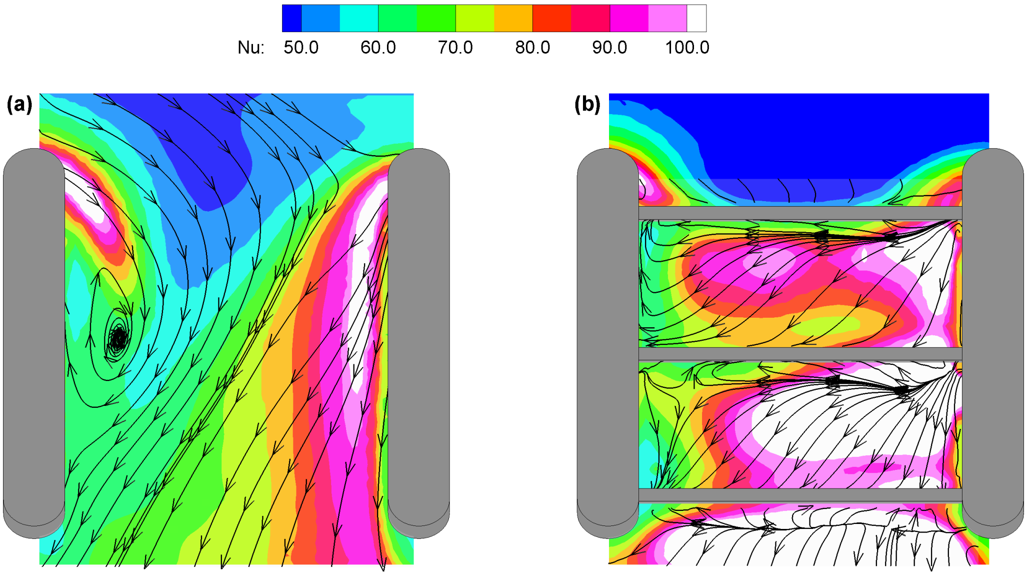

FIGURE 7.31 – Nu Number distribution on the SS across passage P4 and mean stream-tracers on plane xy' for G0 (a) and G2 (b).

should be noted that this latter coherent structure may have a significant impact on the thermal field.

At this point it should be clear that the blockage and the boundary layer tripping induced by the ribs determine a more uniform flow conditions at the SS as the coolant flows in the passage. The proof of this is that the stream-tracers path in plane xy' reveal the appearance of slight trace of a reattachment line after the second riblet, whereas the last obstacle is clearly followed by a reattachment line (see [84]) that is found at the same distance from the rib all along of it. Consequently the Nu Number distribution has to be more uniform moving from the inlet, where the horse-shoes are found, towards the outlet of each IP passage, as shown in Fig. 7.31 (a).

Highlighted features of configuration G2

Summarizing, the analysis performed for configuration G1 highlighted that:

- the presence of the ribs, beside reducing the separation bubbles in the IP channels and particularly in P1, does not vary significantly the flow field in the symmetry plane xy;
- in the TEregion a significant increase of the heat transfer mechanisms is found;
- the Nu Number distribution is strongly non-uniform at the TE channels inlets, where horse-shoe vortices are still detected;
- on the contrary, as towards the TE outlet the rib-induced secondary flows are stronger thus they determine a more uniform HTC distribution along x direction;
- the rib-induced secondary flows and the separation bubble at the pedestal downwind side determine a recirculation region in the corner between the downstream face of the 3^{RD} pedestal and the PS wall, which may have a significant impact on the thermal field.

7.4 Assessment of the global performances

In figure 7.32 the area-averaged Nu Number computed across each IP discharge channel at the TE. It shows that a similar behaviour is found for the three configurations along the radial direction. Passage P1 presents always the minimum values, in view of the recirculation bubble, while P2 and P3 benefit of the highest HTC rates. This latter are due to the higher deflection of the flow approaching the pedestals which determines the strongest secondary structures observed. Moving towards the model tip, decreasing Nu Numbers are found, indeed, as observed previously the flow velocity decreased along the x direction, penalising the HTC mechanisms. G2 grants the highest Nu Numbers, however G1 shows a significant increase of the HTC in the TE portion even if the ribs were installed in the radial development region of the channel. This behaviour has to be ascribed to the features of the flow approaching the pedestals, as reported in section 7.2.

A conclusive observation concerning the enhance of the HTC allowed by G1 and G2 can be obtained by the comparison of the Nu Numbers averaged on the whole SS wall and then normalized with respect to the one obtained for G0. Table 7.1 shows that an augmentation of 25 % is achieved by G1, whereas G2 grants an increase of only 5%, as a consequence of the fact that the Nu Numbers are increased only on a limited portion of the SS.

TABLE 7.1 – Comparison of the global HTC performance parameters.

	G1	**G2**
$\overline{Nu}/\overline{Nu}_{G0}$	1.25	1.05
$\overline{\xi}/\overline{\xi}_{G0}$	1.08	1.13

Moreover, Tab. 7.1 reports also the channel pressure losses increase due to the introduction of the turbolators. Even from this point of view, G1 turns out to be the most profitable, with an increase of the pressure drop of 8%, whereas G2 determines an

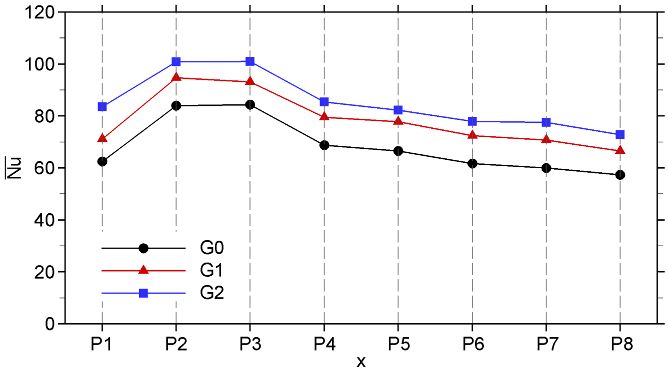

FIGURE 7.32 – Averaged Nu Number distributions over each IP passage at the TE, $-235 < y < -130$ mm.

augmentation of 13%. Indeed the blockage related to the turbulators adopted in G1 is equal to 15%, whereas, the one induced by the third turbulator in G2 is equal to 20% as reported in section 6.2

In conclusion, on the basis of the analysis reported, the most effective configuration is G1, which allows the higher global HTC increase with the smaller pressure losses augmentation.

8

Effects of rotation

In the following chapter, the results of the flow field measurement under rotation are reported. The Coriolis effect is addressed for G0 and G1 configurations. The aerodynamic analysis is then extended to the aero-thermal behavior thanks to the thermal field obtained by means of LCT thermography at the University of Florence.

Before entering in the details, it should be noted that, the experimental conditions of the measurements presented in the following differ from the ones of the previous data. As reported previously in section 6.3, a filter was placed at the channel exits to reduce the centrifugal force pressure gradient negligible. For this reasons, the case at Ro=0 used as reference to support the analysis is constituted by a new experimental campaign taking into account for the modifications on the flow filed induced by the filter. However, as shown in appendix C, the perturbation introduced by this latter on the flow field are small and do not substantially modify the flow features described in section 7.1. It should be noted that a meaningful comparison for the interpretation of the data was obtained.

8.1 Configuration G0

8.1.1 Flow field

Inlet flow characteristics

In Fig. 8.1 the inlet flow characteristics for the rotating channel are reported at position $x = -69.8mm$. The U velocity profiles from plane xy have to be compared with those for Ro=0 in Fig. 7.1(a). Under rotation, the inlet flow is strongly imbalanced toward the leading side of the channel ($y > 0$). Despite the relative low Re Number, this flow deviation has to be ascribed to inviscid flow effects, namely the conservation of angular momentum. Indeed when the flow enters the channel it tends to preserve its angular momentum and so a relative vorticity opposite to the one imposed by rotation must appear. This effect is maximum for the ideal case of a steady potential flow with constant entropy and rothalpy, as shown in [85]. Under these assumptions the analytical solution obtained by Beltrami ([86]) is:

$$\nabla \times \vec{C} = -2\vec{\Omega} \rightarrow \Delta U = 2\Omega b \, (V, W \approx 0) \tag{8.1.1}$$

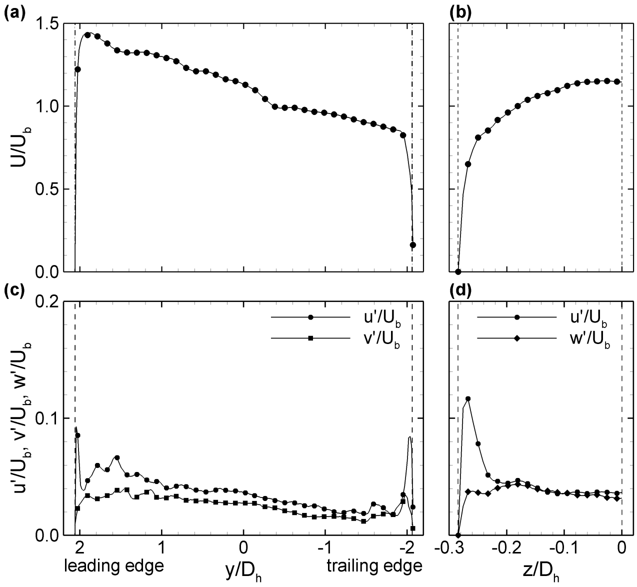

FIGURE 8.1 – Stream-wise U velocity and u', $v'$and $w' r.m.s.$fluctuations profiles at $x = -1.2Dh$ along y (8.1(a),(c)) and z (8.1(b),(d)) directions extracted from measurement plane xy and xz_{IN}in the case of Ro=0.23.

where b is the channel width (4.12 Dh) and ΔU is the velocity difference between the two channel sides. The experimental data agree qualitatively but not quantitatively with the ideal case, showing a lower velocity difference between the channel leading and trailing sides. This is mainly due to the existence of not negligible viscous effects on the flow inside the settling chamber which make the assumption of irrotational flow no longer valid.

For what concerns the stream-wise velocity profile distribution in the vertical symmetry plane of the inlet channel for Ro=0.23 is reported in Fig. 8.1, the comparison with the same data for Ro=0 (Fig. 7.1(a)) does not show significant differences.

In a relative flow field as the present one, Coriolis forces are often considered the only responsible for mass flow redistribution that derives from the appearance of secondary structures acting on the channel cross section. In a channel with outwards radial flow as the inlet section of the present model rotation induced Coriolis vortices yield a velocity profile skewed towards the trailing edge side as shown by Bons and Kerrebrok [32]. In the present case, this effect is overcome by the inviscid flow effect commented above, which is significantly enhanced by the high aspect ratio of the inlet duct cross-section and by the choice of a channel orientation that implies the alignment between the direction of the peripheral velocity and the duct width (see Fig. 6.6). It should be observed that the potential flow effect is a peculiar feature of this geometry. Indeed, as reported in appendix D, the settling chamber guarantees uniform flow conditions whether it is rotating or not. In order to understand the correlation between the potential effect and the cross section

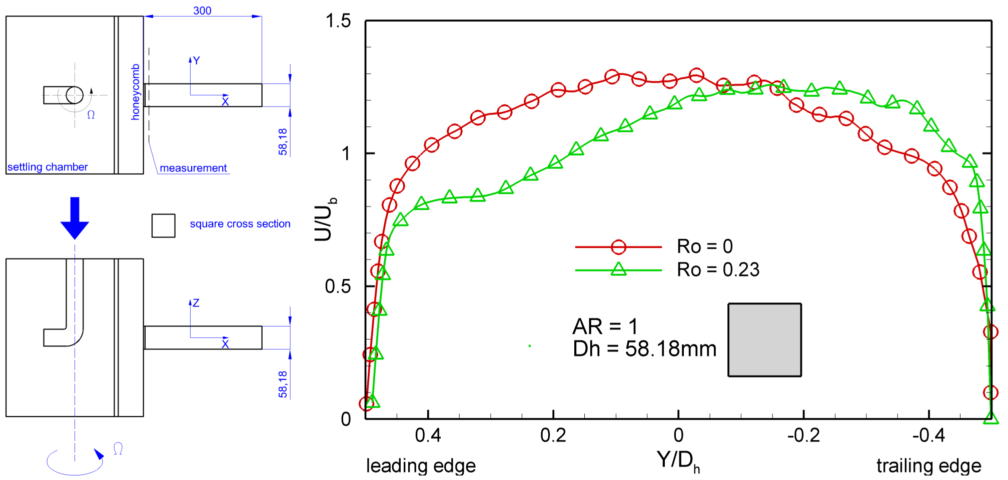

(a) Sketch of the square duct assembly.

(b) U velocity profiles along y at mid-channel height in static and rotating conditions of the square duct, $Dh = 58.18mm$, $20mm$ downstream the honeycomb filter.

FIGURE 8.2

aspect ratio, further test were performed on a radial duct with a square cross section whit the same hydraulic diameter of the test section ($Dh = 58.18mm$). The test reported that the U velocity profile along y will show a maxima displaced towards the TE, Fig. 8.2(b) as shown by Bons et al. Based upon these observations, the observed effect appears to be strictly related to the peculiar features of the geometry. For completeness, it should be noted that the entry section of the preset set up cannot be considered as fully representative of the feeding ducts realised in the blade root. However, a behaviour similar to the one presented cannot be excluded a priori. Consequently, the need for detailed experimental analysis is essential to to provide a reliable insight on the flow behaviour and correct boundary conditions for CFD analysis.

Concerning the velocity fluctuations in plane xy, both u' and v' are higher at the LE than at the TE. This fact is more related to the local velocity levels than to a de-stabilising or de stabilising effect on the boundary layer as proposed by Tritton [30]. Indeed it should be noted that in this channel portion the Coriolis forces play a minor role. The $r.m.s.$ fluctuations of U and W in plane xz_{IN} do not substantially differ from the ones of the static case, as shown by Fig. 8.1. Finally, the small perturbations have to be ascribed to the honeycomb filter placed at the channel entry section, which use is however essential to prevent flow separation and to promote flow turbulence.

Flow field on the symmetry plane xy

The time-averaged relative velocity field measured in plane xy inside the rotating duct is presented in Fig. 8.4(a). The comparison with the stationary data (Fig. 8.3(a)) shows large scale differences in the flow behaviour: wider flow separation at the tip, more

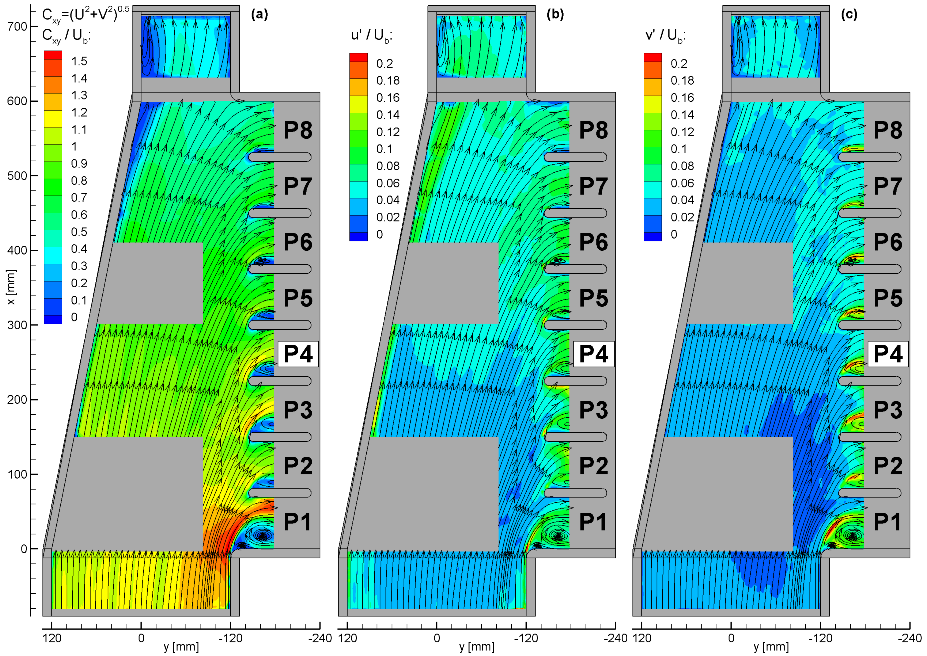

FIGURE 8.3 – Contours of time averaged in-plane velocity C_{xy} (a), u'(b), v'(c) and stream-tracers on the symmetry plane xy for Ro=0.

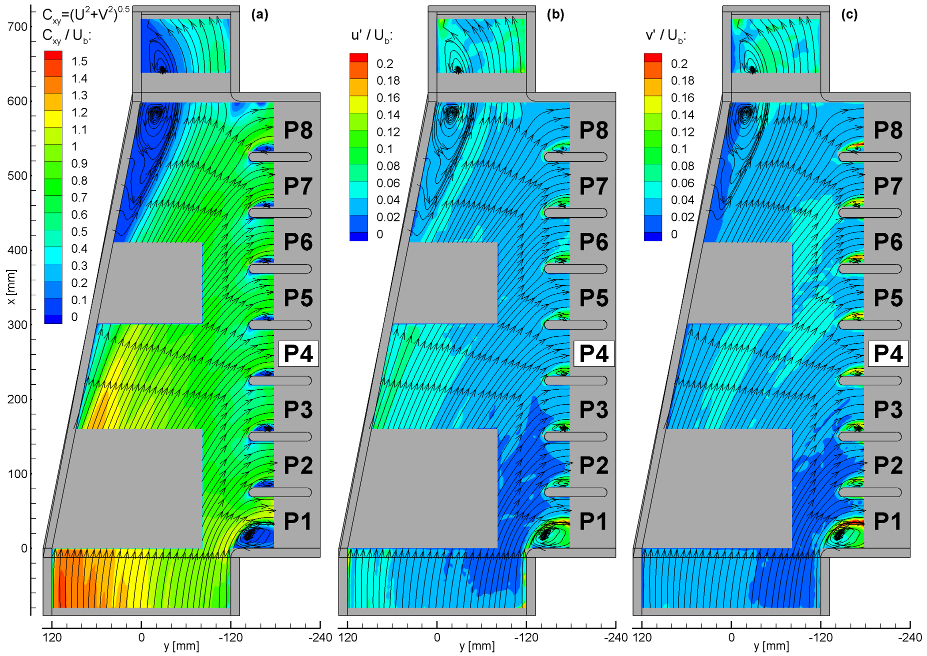

FIGURE 8.4 – Contours of time averaged in-plane velocity C_{xy} (a), u'(b), v'(c) and stream-tracers on the symmetry plane xy for Ro=0.23.

uniform flow velocity at the TE, and substantially different flow velocity distribution in the channel entry section as commented above. By contrast, the estimate of the mass flow discharged at the tip, performed in the same manner as for the Ro=0, showed that the mass flow split between the channel exits does not vary with respect to the static case (about 10% at the tip and 90% along the TE).

Coriolis effects in the radial development channel

Coriolis effects turn out to be more intense in the mean flow at higher radii. Figure 8.5 shows the time averaged stream-tracers superimposed to the contour plots of the in-plane mean velocity in the xy, xy_3, xy_4, and yz_{ip} planes. Different flow paths can be observed by comparing Fig. 8.5(a) with Figs. 8.5(a) and (c). The Coriolis force,$\vec{F_c} = -2\rho\vec{\Omega}\times\vec{C_{xyz}}$, acts in plane xy along the direction normal to the stream-tracers towards $y < 0$, and is proportional to the in-plane flow velocity modulus C_{xy}.

Therefore $\vec{F_c}$ is stronger on the core flow, so resulting in a significant change of the stream-tracers curvature when observed at different channel elevations, as shown also by the plots in Fig. 8.6. In this figure, the flow angles with respect to the y direction are computed along a line at $x = 262.5\ mm$ (the dashed white lines in Figs. 8.5 (a, b, and c) from the data in the xy, xy_3, and xy_4 planes for both Ro=0 and 0.23. In static conditions (Fig. 8.6), the higher inertia of the core flow makes its redirection towards the TE exit less intense with respect to the slower boundary layer flow. As consequence, the flow angle in the xy plane is always bigger with respect to those detected in planes xy_3

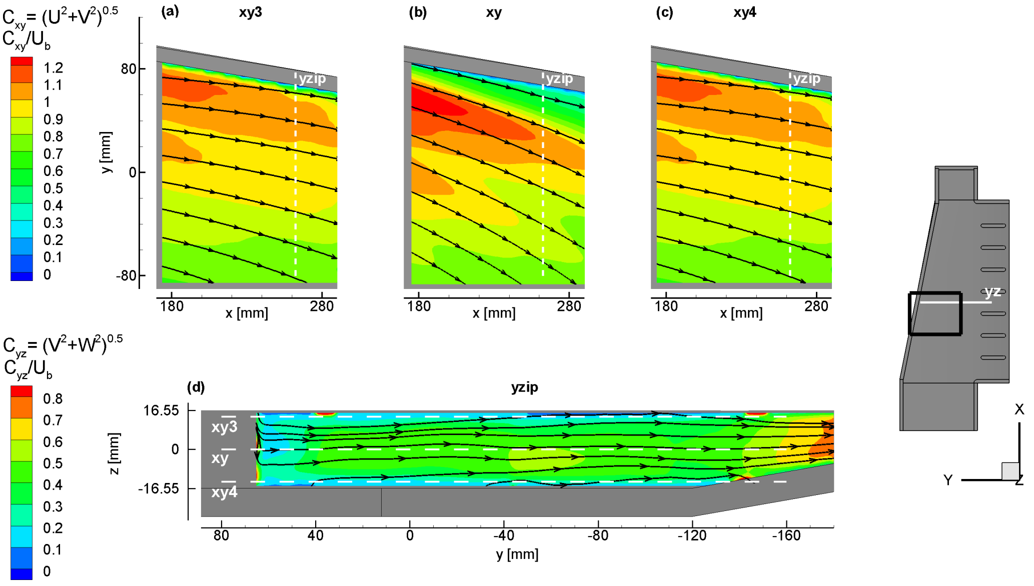

FIGURE 8.5 – Contours of time averaged in-plane velocity C_{xy} (a-c) and C_{yz}(d) and stream-tracers in planes xy_3 (a), xy (b),xy_4 (c) and yz_{ip} (d) for Ro=0.23.

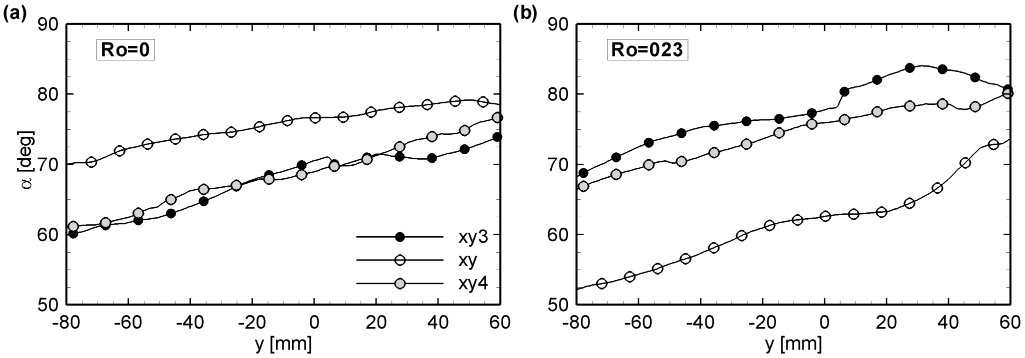

FIGURE 8.6 – Comparison of flow angles, α, for Ro=0 (a) and 0.23 (b). Data extracted from measurement plane xy, xy_3, and xy_4along a line at $x = 262.5mm$.

and xy_4. For Ro=0.23 (Fig. 8.6(b)), opposite trends are found: the smallest angles are detected in the core flow (plane xy) and slightly higher values than for Ro=0 are found in planes xy_3 and xy_4. The commented deviation of the mean flow path has an impact on the flow distribution along the channel height. As an example, Fig. 8.7 reports velocity profiles extracted from the yz_{ip} plane at position $y = -40\ mm$.

Under rotation, Coriolis forces turn the velocity vector in the core flow towards $y < 0$. Consistently, an augmentation of the y velocity component $V$and a reduction of the U one are observed about position $z = 0\ mm$ with respect to the static case (Fig. 8.7 (b and a). Because of momentum conservation, a pressure gradient normal to the core flow velocity vector and pointing towards $y < 0$ will arise. According to boundary layer theory, this pressure gradient acts also in the near wall region where, in view of the lower intensity of Coriolis forces, it produces a flow acceleration along x direction, as clearly shown by the comparison of the Uvelocity profiles in Fig. 8.7(a), further informations can be found in the appendix B. The resulting stream-wise velocity distribution is characterised by a twisted velocity profile (Fig. 8.7 (d and e) with boundary layers far thinner than the ones observed for Ro=0 (Fig. 8.7 (c)).

In the present case, because of the flow discharge along the TE, the mass flow redistribution due to rotation is not associated with the appearance of large and intense secondary vortices, as demonstrated by the stream-tracers path in Fig. 8.5(d). It is important to notice that in this measurements set, a significant uncertainty in the Wvelocity is expected in view of its very low value (about 0.01 U_b). This explains, for example, the wavy path of the stream-tracers presented in Fig. 8.5(d). Nevertheless, those data can still be used at least for a qualitative representation of the mean flow structure. Finally, the enhanced flow curvature commented in the central plane xy (Fig. 8.5(b)) justifies also the existence of a wider separation at the model tip with respect to the static case (see. Figs. 8.4(a) and 8.3(a)).

As a direct consequence of the rotational effects just commented, the flow angle of attack to the pedestals measured in the xy central plane ($z = 0$) is reduced when switching from static to rotating conditions, Fig. 8.8. This in turns makes the flow separation on

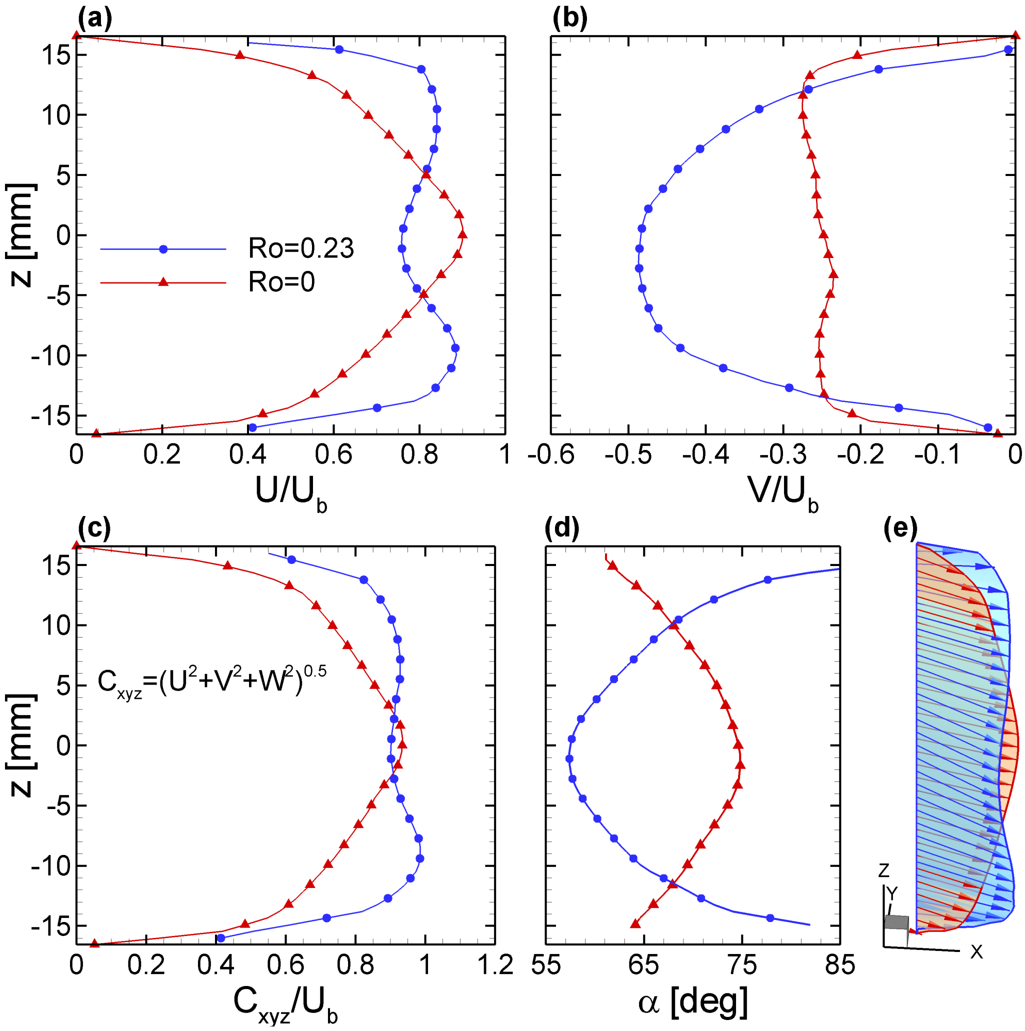

FIGURE 8.7 – Comparison of velocity profiles characteristics for Ro=0 and 0.23 extracted from plane yz_{ip} at $y = -40mm$: mean radial velocity U (a), mean V velocity (b), velocity modulus C_{xyz}(c), incidence angle $\alpha = \arctan(u/-v)$, velocity vectors distribution along the data extraction line (e).

the pedestals suction side less intense and smaller recirculation bubbles are observed in almost all the TE passages (Figs. 8.4(a) and 8.3(a)). A quantitative comparison is provided in Fig. 8.9, where V velocity profiles extracted from plane xy along a line at $y = -150\ mm$ for Ro=0, 0.23 are shown. At this channel elevation ($z = 0$), a clear reduction of the extension of the recirculating flow region is reported for Ro=0.23 in the first five inter-pedestal passages, together with a reduction of the Vvelocity values. For passages P6 and P7, the bubble size is about the same as for Ro=0. Only for passage P8 a wider separation, and consistently an increased flow velocity, is detected with respect

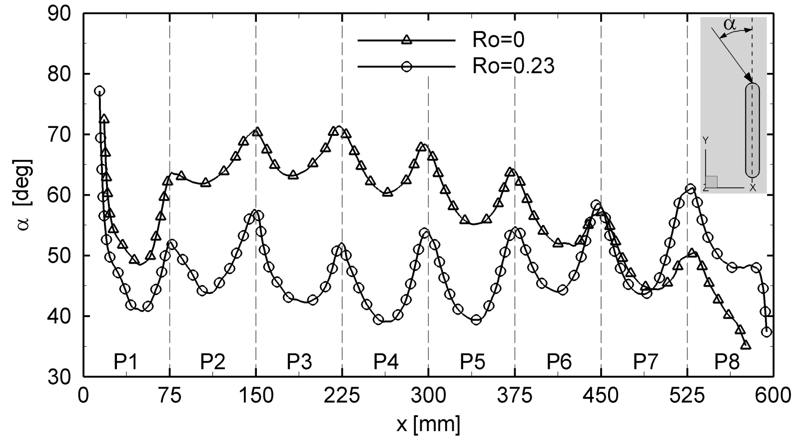

FIGURE 8.8 – Comparison of flow angles, α, for Ro=0 and 0.23. Data extracted from measurement plane xy along a line at $y = -132\ mm$.

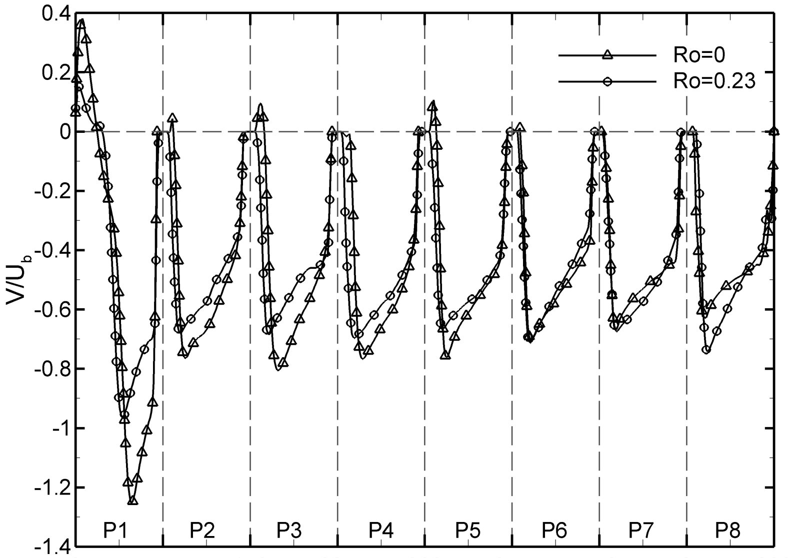

FIGURE 8.9 – Comparison of v̌elocity profiles for Ro=0 and 0.23 extracted from plane xy at $y = -150mm$.

to the static case, in agreement with the higher angle of attack reported in Fig. 6.

The rotational effects on the flow field just commented have also a remarkable impact on the flow turbulent statistics, provided for plane xy in Figs. 8.4(b,c). With respect to the stationary case (Figs. 8.3(b,c)), lower values of both u' and v' fluctuations are found almost at every location of plane xy. Concerning this observation, it is useful to observe that the difference between static and rotating fluctuations in the order of $3 \cdot 10^{-2} U_b$ for u' and $1.5 \cdot 10^{-2} U_b$ for v', therefore comparable with the related uncertainty. Moreover, in the author opinion, considerations about a stabilising or de stabilising effect as the ones that can be found in Tritton et al. [30] for a rotating duct, cannot be drawn in this case in view of the peculiar geometry of the model. Therefore, based on the available informations a meaningful and trustworthy explanation concerning this behaviour cannot be made.

However, it can be observed that the reduced flow angle of attack to the pedestals makes the flow separations downstream of the obstacles less intense, with a consequent reduction of the flow turbulence levels. This, with the exception of passage P8 where the flow angle of attack is higher than for Ro=0, as already commented.

Effects on the inter-pedestals flow structure

The details of the mean inter-pedestals flow structure for Ro=0.23 are reported in Fig. 8.10.

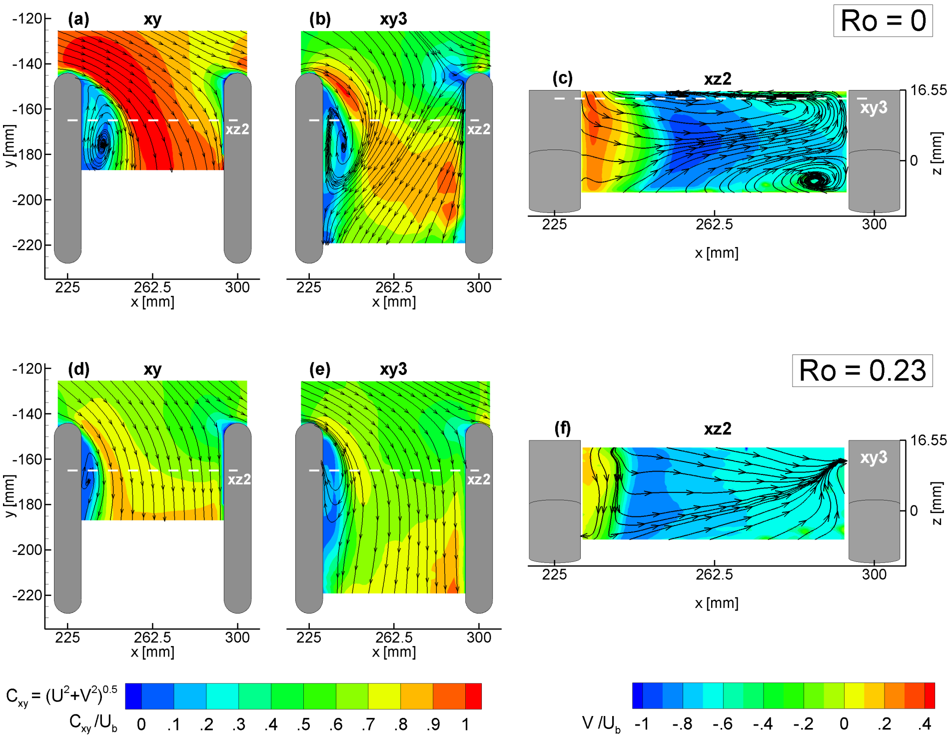

FIGURE 8.10 – Time averaged stream-tracers and velocity contour plots inside the 4^{TH} inter-pedestal passage for Ro=0 (a-c) and 0.23 (d-f).

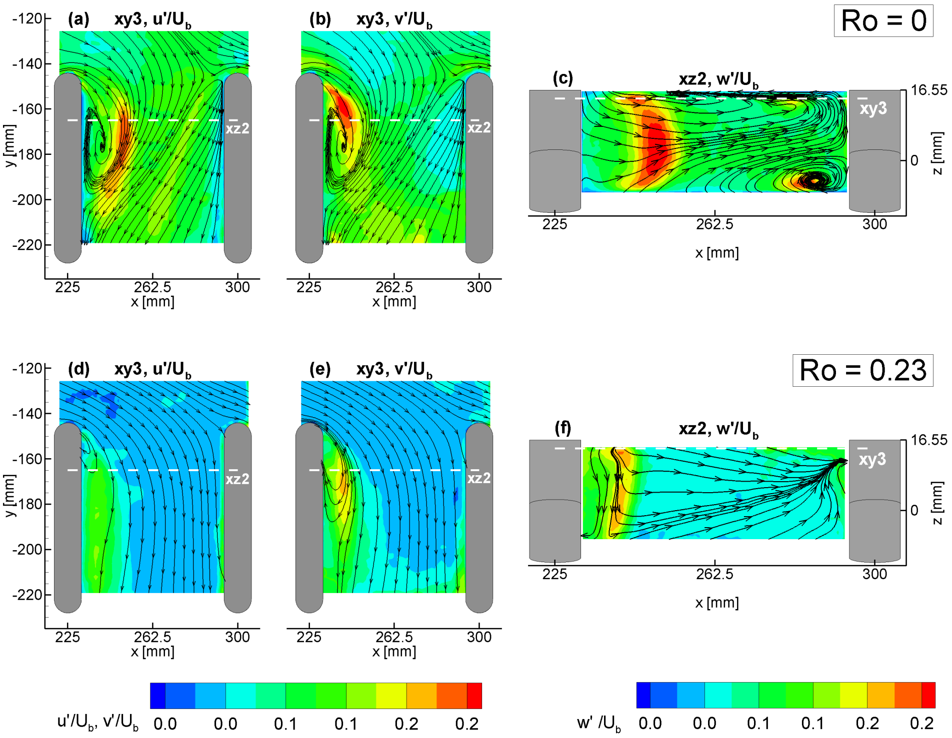

FIGURE 8.11 – Time averaged stream-tracers and contour plots of u' (a,d) and v' (b,e) velocity fluctuations in plane xy_3 and wall normal velocity fluctuations (c,f) in plane xz_2 inside the 4^{TH} inter-pedestal passage for Ro=0 (a-c) and 0.23(d-f).

In comparison with the data for Ro=0 (Fig. 7a and b), the mean flow turns out to be more aligned along the passage axis (Figs. 8.10 (a and b)). This different behaviour results from the combination of multiple effects, namely the reduction of the flow angle of attack to the pedestals (Fig. 8.8) and the Coriolis forces that divert the inter-pedestals flow towards $x < 0$. Moreover, in the near wall flow no evident traces of horse-shoe vortices are found on the upstream side of the pedestal, as highlighted by the stream-tracers in plane xz_2 of Fig. 8.10(c).

The reason of this has to be found in the velocity distribution of the flow approaching the pedestal. Indeed, the horse-shoe dimension is proportional to the extension of the boundary layer that approaches the junction region where the structure is generated, as reported in Ballio et al. [83] and Fleming et al. [82]. Under rotation, because of the rotational effects on the flow inside the channel central portion, the approaching flow is characterised by a more uniform stream-wise velocity distribution and thinner boundary layers with respect to the static conditions (Fig. 8.12), so leading to much smaller and hardly detectable horse-shoes vortices (in Fig. 8.12, position $y = -120mm$ has been chosen because it is about the point where the streamline that impinges onto the obstacle crosses the measurement plane yz, see Fig. 8.4(a)). Also by the visual inspection of the instantaneous flow fields no evidence of horse-shoe structures was found. Dedicated and

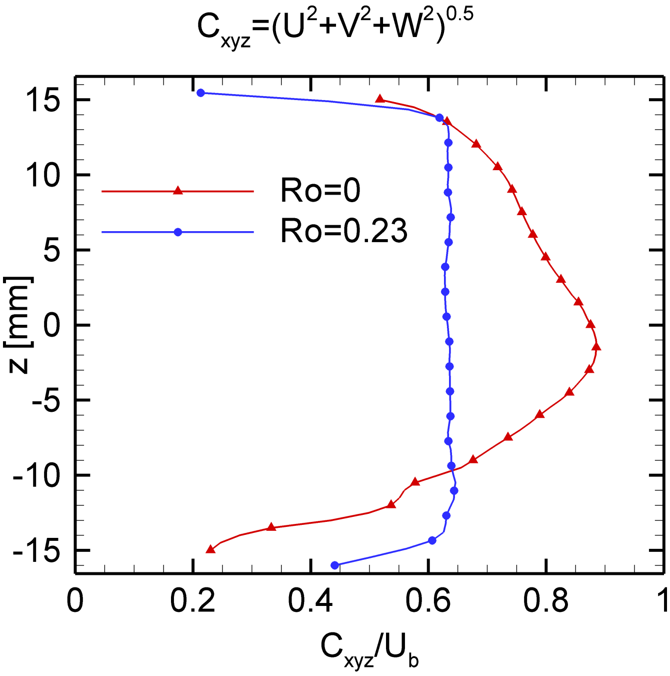

Figure 8.12 – Comparison of stream-wise velocity profiles for Ro=0 and 0.23 extracted from plane yz_{ip} at $y = -120mm$.

very high resolution measurements will be necessary to detected such small flow features. Again, as it was for the flow in the channel central portion (Fig. 8.5(d)), no traces of secondary vortical structures due to Coriolis forces are detected by the stream-tracers path in plane xz_2(Fig. 8.10(c)). All the above observations are supported and confirmed by the velocity fluctuations maps shown in Fig. 8.11.

An overall reduction of the turbulent activity can be observed with respect to the stationary case, as it can be observed from the comparison of Figs. 8.11 (a-c) whit Figs. 8.11 (d-f). It should be noted that the absence of the horse-shoe structures is further confirmed by the lack of wall normal fluctuations peaks in the map of Fig. 8.11(c).

In conclusion, in the inter-pedestals region the rotational effects determine the development of a more uniform flow, characterised by a strong reduction of both the separated flow regions and horse-shoe vortices dimensions. Even if this ensures a more uniform distribution of the heat transfer coefficient over the channel surfaces, the enhancement factor due to the turbulent mixing associated to the horse-shoe vortices will be lost, as it is predicted by the numerical analysis of Andreini et al. [87].

8.1.2 Thermal field

Thanks to the HTC measurements, showed in Fig. **??** performed by the researches of the University of Florence on their brand-new rotating rig, an assessment of the influence of the flow characteristics observed previously on the thermal field can be performed.

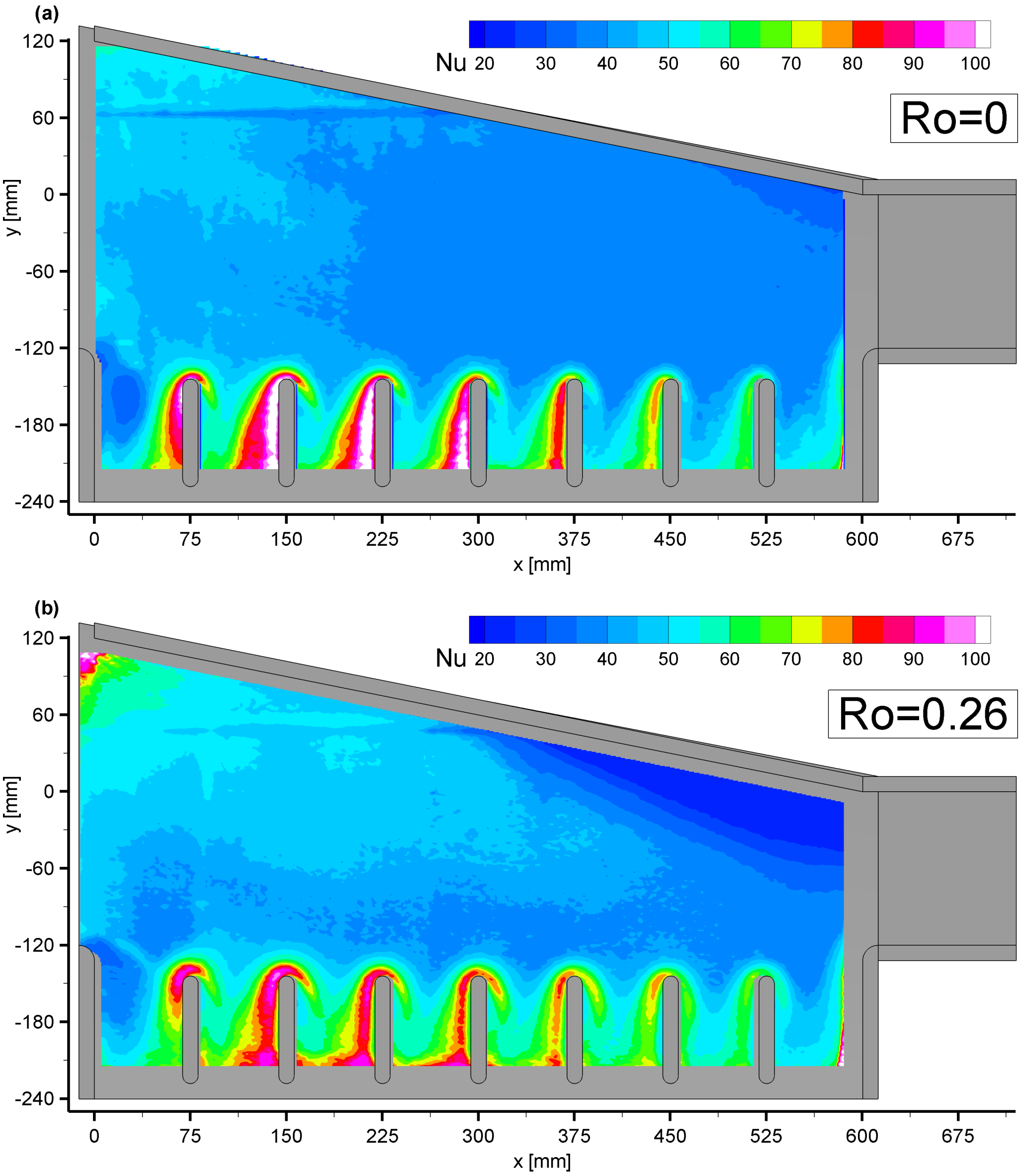

FIGURE 8.13 – HTC distribution on PS for Ro= 0 (a) and 0.26 (b).

The measurements were performed on the same channel geometry at Re=20k and for a rotation Number equal to 0.26 slightly bigger, than the one of the flow field data. Moreover, a filter, having the same characteristics of the one used by the author, was placed at the duct exits as well. Differently to the data presented in the previous chapter, the LCT measurements were performed on the PS in view of the rig viewing constraints.

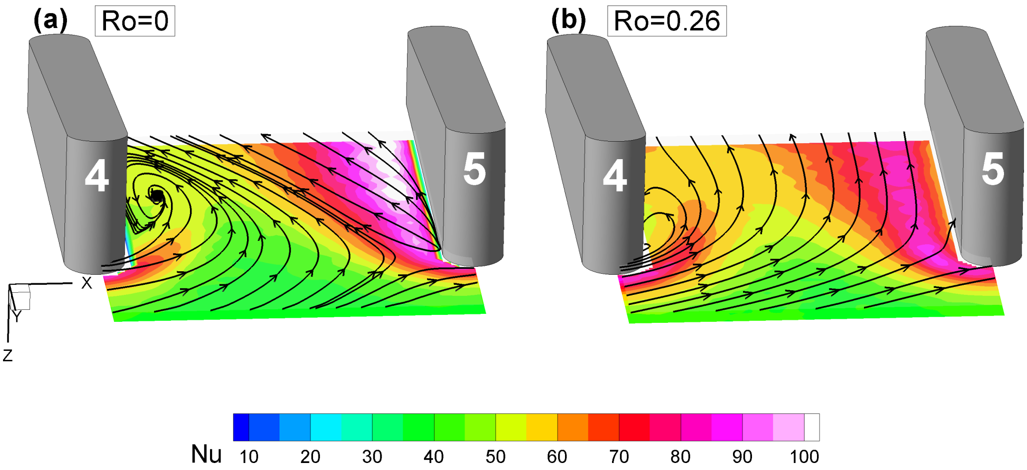

FIGURE 8.14 – HTC distribution on PS and time averaged stream-tracers in plane xy_3 for Ro= 0 (a) and 0.26 (b) for the IP passage P4.

More in detail at the channel inlet the higher velocity at the leading edge side of the channel turns in a more effective convective heat transfer mechanism with respect to the trailing edge side.

In the radial development region a lower boundary layer thickness has been observed (Fig. 8.7), this in turn determines a slight increase of the Nu number in this region with respect to the static case. However, this augmentation is fairly small because in this channel portion the heat transfer mechanism is due only to simple forced convection (Fig. **??**). At the model tip, the significant increase of the recirculation bubble, yields to a enlarged low-HTC region with respect to Ro=0.

Concerning the TE regions, it should be noted that two features with opposite influence on the thermal filed have been found. The reduction of the boundary layer thickness should turn in higher HTC whereas the reduction of w' would determine a less effective heat exchange process. What happens is that the HTC distribution has fairly the same levels in the central part of the passage. In contrast, a reduction of HTC peak is found on the pedestal upstream face, as a consequence of the reduction of the horse-shoe vortex observed previously (Fig. 8.14).

8.1.3 Highlighted effects of Coriolis on the flow field

In conclusion the analysis performed showed that:

- an inviscid flow effect (the momentum conservation) takes place at the channel inlet, yields to higher flow velocities at the leading edge side and lower at the TE;

- the Coriolis forces in the radial development channel deflect the core flow towards the TE, while the boundary layers are deflected towards $y > 0$, i.e. the LE;

- the x-component of the Coriolis forces determine a strong reduction of the boundary layer thickness along the channel height;
- the reduction of the angle of attack to the pedestal and, more significantly, the reduction of the boundary layer thickness determine a strong reduction of the secondary flows in the IP channel which are not observed any more;
- the disappearance of the horse-shoe branch turns in a reduction of the Nu peak at the PS towards the pedestal upstream face;
- a large dead water zone is found at the LE side of the channel from $x \approx 240$ to the model tip, which yields to low HTC values.

8.2 Configuration G1

Once the effects of Coriolis on the flow field have been deeply investigated for the smooth channel, a question arises about the coupling of the flow perturbations induced by the ribs and by rotation.

Rib induced secondary flow under rotation at the LE

In contrast to what has been observed for Ro=0, the adoption of riblets in the radial development channel has a noteworthy impact on the flow field under rotation, as it can be observed in Fig. 8.15. For completeness Fig. 8.16 reports the stationary data acquired with the polyester fibre filter at the outlets.

Shifting the attention to the maps at Ro=0.23, the comparison of the flow field in G0 (Fig. 8.4) and G1 shows that the dead water zone found at the channel LE side is vanished in the ribbed channel. More correctly, low in-plane velocities are still found from $x \approx 260\ mm$ towards the LE side, but the stream tracers path does not reveal the presence of the recirculation bubble that was observed in G0. This behaviour has to be ascribed, of course, to the presence of the turbulence promoters and particularly to their orientation. As shown by Han [2], a negative angle with respect to the stream wise direction will turn in a secondary flow that redistributes the mass flow towards the $y > 0$ side. This observation is confirmed by the velocity maps reported in Fig. 8.17.

The stream-tracers in plane xy_4, Fig. 8.17 (e), clearly reveal that a mass flow redistribution towards the LE side occurs past the 3^{RD} rib. The coolant impinges on the LE and it is thus re-directed towards the upper (PS) wall and then back in the bulk flow, as shown by the stream-tracers in plane xy_3, Fig. 8.17 (d). Indeed, these latter are strongly deflected towards $y < 0$ near the LE of the channel and at $x > 240\ mm$. These informations, coupled with the presence of a separation line between the core flow, at the higher velocity, and the region towards the LE observed in xy_3, allow to hypothesize the presence of a secondary flow as the one sketched in Fig. 8.18. More in detail, this flow structure is made of a counter-clockwise vortex cell which determines a considerable flow mixing. Further investigations, namely S-PIV measurements in a cross-wise plane are planned to better describe this structure ad will be included in the future development of this work.

However some interesting informations can be still addressed even from xy measurement plane. One of this concerns the boundary layer thickness in the radial development channel. In 8.1.1 it has been described how Coriolis force substantially modifies the flow yielding to a strong decrease of the boundary layer thickness. This behaviour is found also for G1. Indeed the in-plane velocity modulus in xy_4 is considerably higher when shifting from static to rotating conditions between the two consecutive ribs 3 and 4, as shown by the comparison of Fig. 8.17 (c) and (e). Unfortunately any further information regarding the effective boundary layer height is available at the moment, but the data in Fig. 8.17 seems to confirm a that a thinner boundary layer is found.

A last observation regards the disappearance of the separation bubble at the LE induced by the strong flow redirection towards this region that takes place at the SS and that is caused by the ribs. From a thermal point of view the existence of a strong

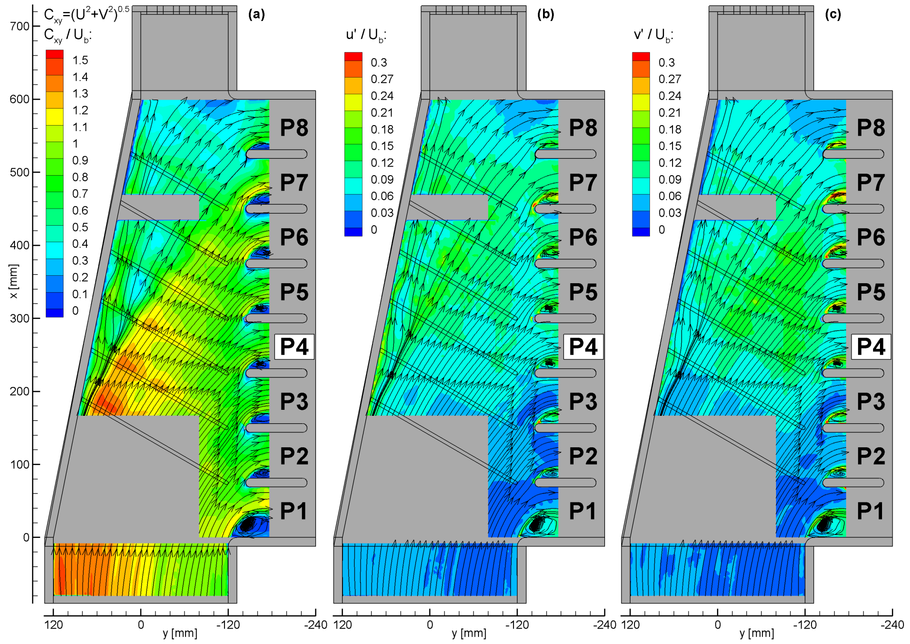

FIGURE 8.15 – Contours of time averaged in-plane velocity C_{xy} (a), u'(b), v'(c) and stream-tracers on the symmetry plane xy for Ro=0.23, configuration G1.

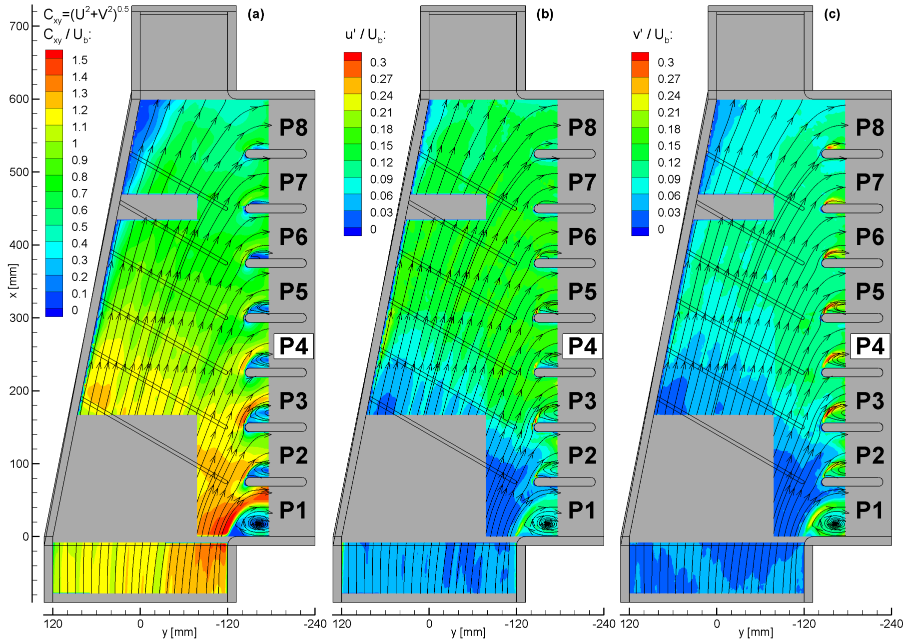

FIGURE 8.16 – Contours of time averaged in-plane velocity C_{xy} (a), u'(b), v'(c) and stream-tracers on the symmetry plane xy for Ro=0, configuration G1

flow mixing at the LE side should turn in a benefit to the heat transfer mechanism as reported in the work by Bonanni et al.[88], where the present channel geometry was equipped with riblets at the PS and operated at comparable flow conditions. This latter HTC augmentation is particularly desired since it regards a region where low HTC values have been observed for G0 at Ro=0.23.

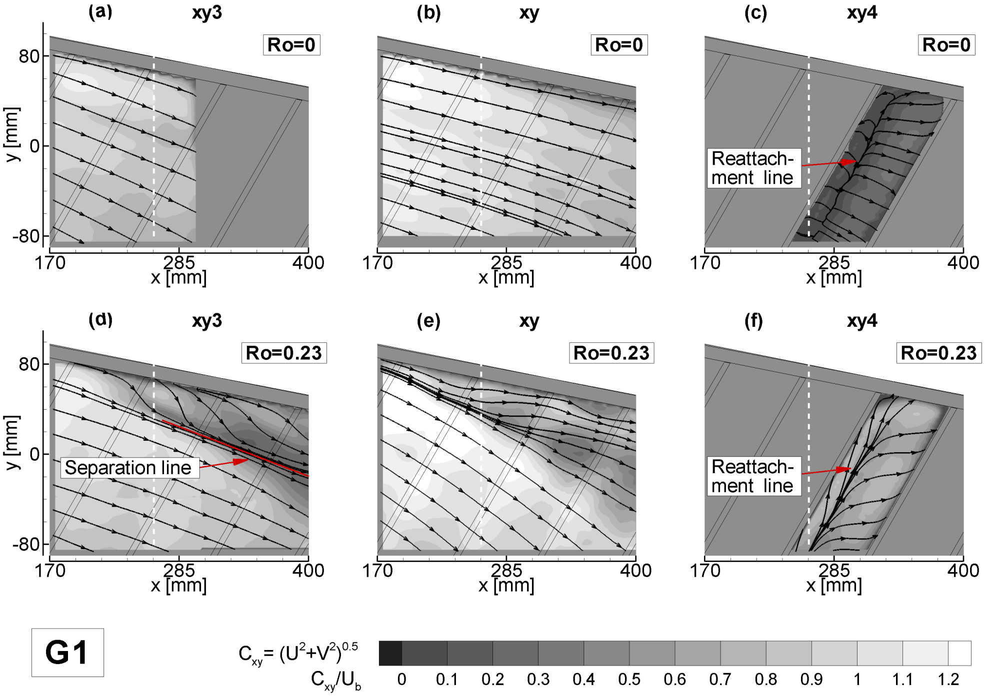

FIGURE 8.17 – Contours of time averaged in-plane velocity C_{xy} and stream-tracers in measurement planes xy_3 (a), xy (b), and xy_4 for Ro=0.23, configuration G1.

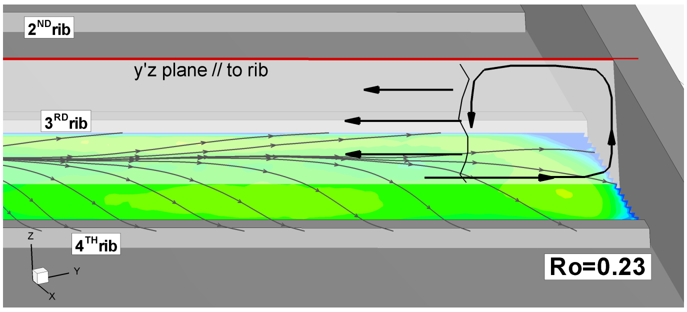

FIGURE 8.18 – Sketch of the secondary flow induced by the ribs a the LE side of the channel.

Flow field in the radial development channel

In contrast to the LE region, the core flow turned out to be similar to the one observed for G0. Indeed the reduction of the in-plane velocity fluctuations u' and v', observed when shifting to rotating conditions for the smooth channel (see 8.1.1) is still found for G1, beside an overall increase of the turbulence levels due to the presence of the riblets, as shown by the comparison of Figs. 8.15 (b,c) with 8.16 (b,c).

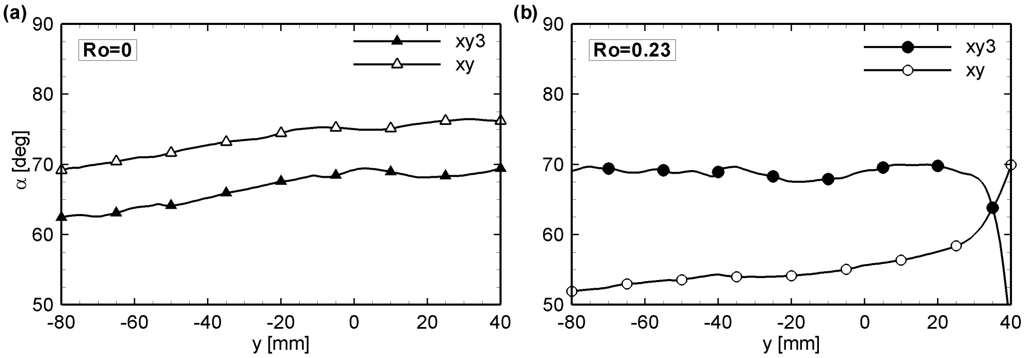

FIGURE 8.19 – Comparison of flow angles, α, for Ro=0 (a) and 0.23 (b). Data extracted from measurement plane $xy$and xy_3 along a line at $x = 262.5mm$, configuration G1.

Moreover, in section 8.1.1 it has been reported that in static conditions, the slower boundary layer flow is more deflected to the TE than the core flow in view of its lower inertia and that it is just the opposite for Ro=0.23 because of the Coriolis forces. This behaviour has been also observed for G1. Indeed the stream-tracerspath in Fig. 8.17 (a,b) for Ro=0 and Fig. 8.17 (c,d) for Ro=0.23 resembles the behaviour observed in G0.

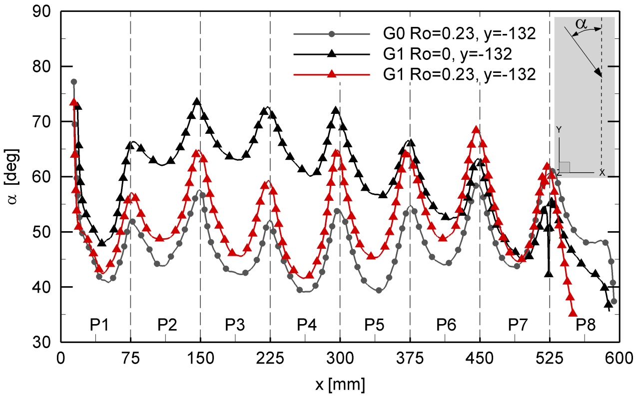

FIGURE 8.20 – Comparison of flow angles, α, for Ro=0 and 0.23. Data extracted from measurement plane xy along a line at $y = -132mm$ for configuration G1.

A more quantitative representation of this opposite trend is presented in Fig. 8.19 where the flow angle with respect to the y direction is computed from velocity profiles extracted from planes xy and xy_3 along a line at $x = 262.5$.

However the redirection towards the TE side induced by the Coriolis forces, turned out to be less intense in G1. Indeed, the flow angle of attack to the pedestal computed along a line at $y = -132mm$ for G1 is considerably lower under rotation, but it is slightly higher than the one measured for G0, as it is reported by Fig. 8.20. This fact is compatible with the deviation imposed by the ribs described previously.

In conclusion, comparable flow conditions at the inlet of the TE outlets were found between G0 ans G1 as suggested by the comparison of v̌elocity profiles extracted from xy along a line at $y = -150mm$ reported in Fig.8.21. Nevertheless, further investigations are needed to investigate the boundary layer thickness of the flow approaching the pedestals.

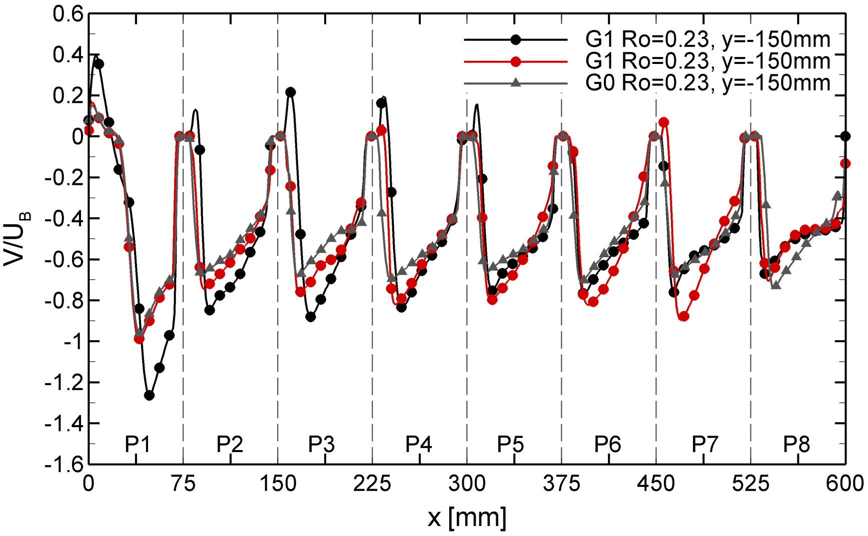

FIGURE 8.21 – Comparison of v̌elocity profiles for Ro=0 and 0.23 extracted from plane xy at $y = -150mm$ for configuration G1.

Effects at the TE outlets

At the present time only a preliminary investigation about the presence an the horse-shoe branch on the PS of the channel are available. Figure 8.22 shows the maps of time averaged in-plane velocity modulus C_{xy} and stream-tracers in plane xy_3 for passage P4. The typical diverging path observed in static conditions determined by the developing of the horse-shoe vortex is disappeared for Ro=0.23 as it was observed in the smooth channel. Therefore it can be reasonably concluded that the size of this latter should be negligible, as it was in G0. By contrast, further investigations are needed (S-PIV measurements in plane xz_2) to discuss the flow features on the PS of the passage. Indeed, on the PS, the absence of secondary flows cannot be excluded a priori, taking into account

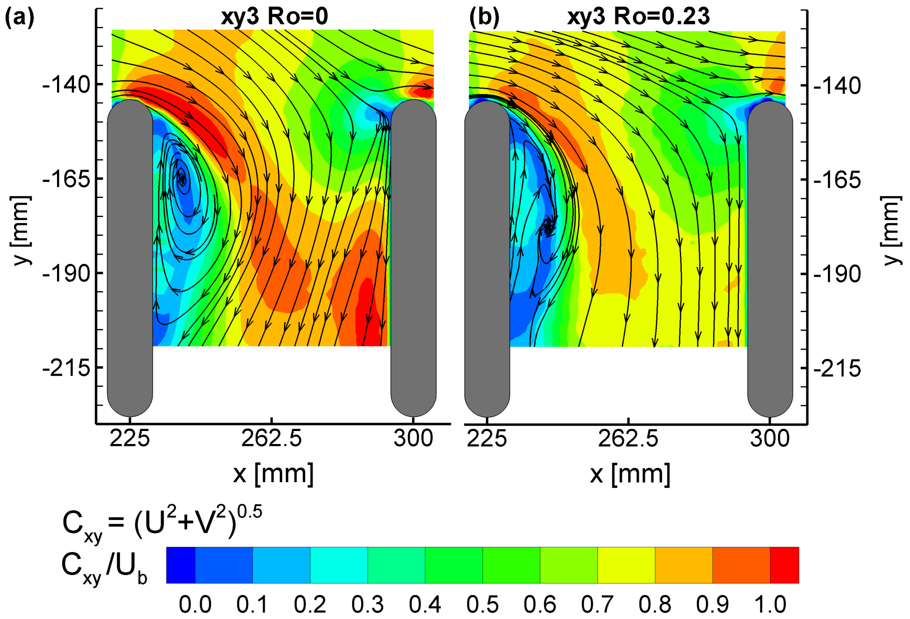

FIGURE 8.22 – Contours of time averaged in-plane velocity C_{xy} and stream-tracers in plane xy_3 for Ro=0(a) and 0.23 (b), configuration G1.

that the presence of the ribs in the radial development channel turned in an increase of the boundary layer thickness at the PS, which is responsible of the horse-shoe size, as reported in section7.2.

8.2.1 Effects of rotation in a ribbed channel

In conclusion the analysis performed showed that:

- a strong flow redirection towards the LE occurs in the flow layers close to the ribbed wall of the channel;
- as a consequence, a secondary structures develops a the LE corner, where G0 showed a dead water zone;
- the flow behaviour in the radial development channel resembles the one observed for G0 with a decrease of the angle of attack to the pedestals;
- inside the TE outlets, any secondary structure is detected on the upstream face of the pedestals at the PS.

Conclusions

The analysis reported in present thesis can be divided in two parts: the first one concerns the analysis of the aero-thermal performance of an internal cooling channel for the trailing edge of a gas turbine blade under static conditions and with two different arrangements to of riblets. The second part provides an assessment of the flow field under rotation for the smooth channel and the most promising configuration of riblets found in the static case. The test were performed at a fixed Reynolds Number of 20k and for two values of the rotation Number, namely Ro=0 and 0.23.

Beside the results here presented, considerable efforts were spent in the design and the manufacturing of the test rig, with particular reference to the balancing and to the synchronisation with the PIV measurement chain. This latter was performed with a relatively simple approach, nevertheless it allowed a noteworthy image position stability.

At the same time, a methodology to obtain the relative flow field from 2D-PIV measurements performed with a fixed system was developed. This latter features an innovative image calibration process, which allows to retrieve the position of the centre of rotation for each acquisition with an high precision. This, coupled with the image position stability allowed by the synchronisation system and to a precise image interpolation scheme allows to de-rotate each second frame of the PIV image pairs by an angle equal to the one occurred during the separation time under rotation. The final result is that the relative flow field can be directly retrieved by cross-correlating the image pairs with an accuracy that is comparable with the one of a standard non rotating PIV measurement.

The aero-thermal analysis was firstly conducted for the smooth channel (G0) and provided a detailed description of the flow field inside the device. Characteristics as the mass flow distributions between the different outlet channels, the 3D features of the flow inside the IP channels at the TE , or the dead water zone in the tip region have been described in detail. This in turn allowed to a full comprehension of the mechanisms that determine the Nu number distribution measured on the SS by means of LCT. More in detail, the thermal analysis revealed that the separation bubble due to the flow angle of attack at the pedestal downstream face and the horse hoe branch developing on the upstream face determine a strongly uneven distribution inside the IP outlets. Also, the the dead water zone in the tip region is responsible for a weak heat transfer process.

By applying the riblets inside the formers a strong HTC augmentation can be obtained, with a more uniform distribution moving from the inlet to the outlet of each channel due to the suppression of the secondary flows a the pedestal upstream face induced by the riblets.

However, the most promising configurations turned out to be G1, i.e. the adoption of riblets in the radial development channel. This latter ensures indeed the highest global HTC increase with the smallest pressure drop increase across the channel. This is a consequence not only of an increase of the Nu number in the radial development region which, in the case of G0 was determined by simple convection, but also to a benefit in the TE region. This latter was justified by an increase of the stream-wise and wall normal component of the velocity fluctuations and to an augmentation of the secondary structures size due to a growth of the boundary layer thickness at the SS.

When the attention was shifted to the analysis of the effects of the Coriolis force on the flow field, significant differences with the stationary conditions were found for G0. More in detail, the inlet flow turned out to be dominated by an inviscid flow effect, namely the conservation of angular momentum, which determines an uneven stream-wise velocity profile. A the same time, the x-component of the Coriolis force determine a strong reduction of the boundary layer thickness in the radial development channel. Then it was observed that the flow deflection imposed by the Coriolis force determines a lower flow angle of attack to the pedestal in the TE region. The former effects are also responsible for a strong reduction of the secondary flows observed at Ro=0 in the TE outlets. Finally, a large recirculation that develops at the LE side of the channel toward the model tip was found. From a thermal point of view, an increase of the HTC in the radial development region is expected in view of the aforementioned reduction of the boundary layer thickness, while low values will be found at the LE, as confirmed by the LCT measurements performed by the researches of the University of Florence.

The preliminary results of the investigation concerning the rotational effects in the rib roughened channel G1 showed that the rib lets promote a mass flow redistribution towards the LE where a strong counter-clockwise rotating structure develops. This, in turn, causes a flow mixing which suppresses the recirculation bubble a the tip observed for G0. Concerning the effects at the TE, any horse-shoe vortex developing at the junction of pedestal upstream face and the PS can be reasonably expected. On the contrary, further investigations are needed to discuss the flow conditions at the SS in the IP channels.

A

Uncertainty analysis

In the following, the uncertainty related to 2D-PIV, S-PIV and LCT measurements is provided.

A.1 2D-PIV measurements uncertainty

Before going into details, it should be noted that the reliability of 2D-PIV (or S-PIV) measurements is, of course, strictly related to the image quality, which itself depends on:

- image focusing;
- background noise of the image;
- the set up alignement;

These error source can be checked and minimizes to negligible values during the preparation of the set up before image acquisition. The processing parameters have a significant importance as well, in section 3.3 the choice of these latter has been addressed.

A.1.1 Static Measurements

The results that will be presented in part III, refer only to statistical quantities, such as the time averaged velocity fields. Due to the limited number of samples (1000) used to compute the flow statistics, the sampling error tends to be larger than other error sources and therefore it was chosen as the overall upper bound estimate for the PIV data uncertainty. For the 2D measurement acquired in planes xy under static conditions, the normalised *r.m.s.* errors in the statistical quantities are computed as in Armellini et al. [89]:

$$\epsilon_u = \frac{\sigma|U|}{|U|} = \frac{1}{\sqrt{N}}\frac{u'}{|U|} \quad , \quad \epsilon'_u = \frac{\sigma|u'|}{u'} = \frac{1}{\sqrt{2N}} \tag{A.1.1}$$

where σ is the standard deviation, U is the mean velocity, u' is the *r.m.s.* velocity fluctuation and N is the number of independent samples. The uncertainties in the measured values of U and u' are simply obtained by multiplying the errors in A.1.1

by a confidence coefficient, Z_c. Assuming values $Z_c = 1.96$ (corresponding to a 95% confidence level) and $N = 1000$, the overall upper bound estimate of the uncertainty in the mean velocities turns out to be less than 2%. This value applies to the largest part of the velocity fields, with the exception of those limited regions affected by very low velocities and high fluctuations, namely inside zones of separated flow. Under the same assumptions, the maximum uncertainty in the estimate of the *r.m.s.*velocities is less than 5%.

A.1.2 Rotating Measurements

Before providing a value on the uncertainty of 2D-PIV measurements in rotating conditions, some issues must be discussed.

As reported in chapter 4, the measurements have been performed in phase locked acquisition with a fixed measurement chain. Since between the trigger input for the PIV chain and the first laser pulse there is a time delay (i.e. the Q-switch delay, see 3.1.1), and because the angular velocity in not constant during a whole acquisition sequence, a variable time delay has to be computed for each revolution. This latter is absolutely necessary to acquire the image pairs with the channel always at the same angular position. Further informations have been given in section 6.1, but at this point of the discussion it is important to keep in mind that the image position stability, i.e. the difference in the channel wall position between different exposures, resulted to be very small: at the model tip the uncertainty in the angular position leads to image shifts of about 1 *px* along both x and y image axes. With a magnification factor of 10 *px/mm* the image shifts were in the order of 0.1 *mm*. This value, considerably smaller than that of [34], allows to neglect the so called phase-averaging error. Indeed a shift as small as $\mp 1 px$ allows that each interrogation window pertains always at the same portion of the channel, therefore, during the further data process only vectors belonging to the same flow region will be averaged together.

A second observation has to be addressed to the pre-processing methodology adopted to retrieve the relative flow field. The careful reader may noticed that an error on the determination of the angular velocity comprises a bias error in the velocity fields, while an error on the determination of the centre of rotation implies a flow distortion, as shown in the work of Armellini et al. [53]. Therefore, the error associated to the de-rotation process has to be added to the one of a standard 2D-PIV measurement. However the analysis reported in [53] reveals that an error comparable to the one of the cross correlation of standard 2D-PIV images, i.e. 0.1 *px* can be achieved if the methodology used in this thesis is followed. Therefore, if particle relative displacements of 6-10 pixels are measured, the de-rotation error is responsible for an increase of the velocity uncertainty of 1% with respect to a standard static measurement.

A.2 Stereo-PIV measurements uncertainty

The S-PIVtechnique has the advantage of providing 3D measurements for a number of points laying on a plane, but its major weakness is the calibration procedure in view of

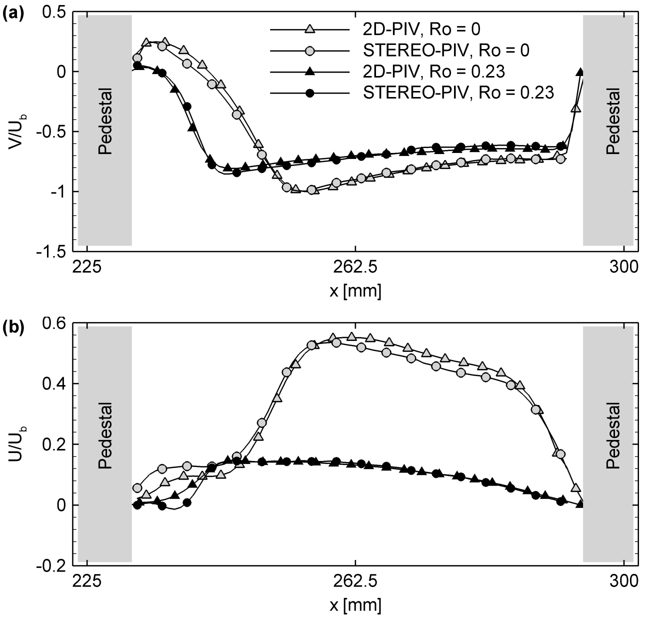

FIGURE A.1 – Comparison of U (b) and V(a) velocity profiles at the intersection line between planes xy and xz_2 for Ro=0 and Ro=0.23.

the misalignment error (see 3.1.3). In the present campaign the disparity correction was used as an attempt to minimise this latter, as suggested by Willert [49]. The disparity map was obtained from the ensemble correlation of 100 images from the two views, as suggested in [51].

As stated in Chapter 4, in the case of S-PIV measurements, the relative velocity field has been retrieved by means a post processing of the instantaneous velocity fields, (i.e. the subtraction of the instantaneous angular velocity). Theoretically, one can perform the de-rotation procedure even with stereo images, but the viewing angles will be required to subtract correctly the peripheral displacements to the particle motion. This means that the error made in the calibration of the measurement chain will be enclosed two times, therefore decreasing the measurement accuracy. Since accurate 2D-PIV measurements are available in both static and rotating conditions the accuracy of the S-PIV ones can be assessed with a cross comparison of velocity profiles extracted along a common line. Figure A.1 shows shows time averaged U and V velocity component profiles extracted along the intersection line between measurement planes xy and xz_2, obtained by means of 2D-PIV and S-PIV respectively. It can be observed that in both test conditions (Ro=0 and 0.23) the Stereo data are almost superimposed to the 2D ones. The differences are within 0.05 U_b, for both in-plane (U) and out-of-plane (V) velocity components of the Stereo data, so revealing a satisfactory accuracy of the Stereo-PIV measurements.

Finally, it has to be observed that for the measurement along the yz and xz planes, the channel rotation determines a misalignment between the laser sheet (image plane) and the actual geometrical plane of the channel. This inconvenience could lead to a significant spatial averaging error. However, in the present experiments the very small separation time required to avoid tracer particles loss, limits the image/geometrical planes misalignment within the laser sheet thickness.

A.3 LCT uncertainty

On the basis of the accuracy of the calibration procedure employed, and of the slight variation of the viewing angle over the camera f-o-v the maximum uncertainty in the superficial temperature T_{wall} can be considered equal to $\pm 0.5K$. The effect of this latter on the determination of the HTC (h) was minimised by keeping the temperature difference between the fluid and the wall at about $20K$.

The other error sources are the ones made in the evaluation of $q_{\dot{disp}}$ and $q_{\dot{irr}}$. An accurate measure of these quantities is particularly difficult, therefore particular care was devoted to keep them as low as possible thus minimising the effects of their errors on h. In the present case the use of an air gap and the low emissivity of the low emissivity of the Inconel heating foil allowed to keep both $q_{\dot{disp}}$ and $q_{\dot{irr}}$ as low as possible. Furthermore, the evaluation of these latter has been performed by following two different approaches. The first of these two was made as it follows: several thermocouples have been applied to the interior and exterior surface of the channel walls, thus allowing an estimation of the conductive heat flux. In contrast, in the second one, the heating foil was powered without any fluid motion inside the channel. Then the power necessary to keep the channel surface at a constant temperature was measured. The results obtained by the two procedures turned out to be comparable, thus a global heat exchange coefficient U equal to 6.5 $W(m^2K)$ was estimated.

Taking into account that $q_{\dot{disp}} + q_{\dot{irr}} = U(T_{wall} - T_{amb})$ and considering an uncertainty on $q_{\dot{disp}} + q_{\dot{irr}}$ equal to 20 % , the error propagation proposed by Kline and Mc-Clintock [71] with a confidence interval of 20:1 (and considering the other error sources) allows to estimate an uncertainty on the Nusselt Number equal to 4 % and 11 % for the highest and the lowest heat exchange regions respectively.

B

Flow governing equations, dimensionless parameters and Coriolis effects

B.1 The Navier Stokes equations

The governing Navier Stokes equations in a coordinate system fixed with the rotating duct are:

$$\frac{\partial \vec{\mathbf{u}}}{\partial t} + \vec{\mathbf{u}} \cdot \nabla \vec{\mathbf{u}} = -\frac{1}{\rho} \nabla P - 2\vec{\Omega} \times \vec{\mathbf{u}} + \beta \left(T - T_{\infty}\right) \left(\vec{\Omega} \times \vec{\Omega} \times \vec{\mathbf{r}}\right) + \nu \nabla^2 \vec{\mathbf{u}} \tag{B.1.1}$$

where $\vec{\mathbf{u}} = U\vec{\mathbf{i}} + V\vec{\mathbf{j}} + W\vec{\mathbf{k}}$ and $\vec{\Omega} = \Omega\vec{\mathbf{k}}$. The Boussinesq approximation has been applied so that density variations are only accounted for in the buoyancy therm. By assuming the steady state conditions, eq. B.1.1 becomes:

$$\vec{\mathbf{u}} \cdot \nabla \vec{\mathbf{u}} = -\frac{1}{\rho} \nabla P - 2\vec{\Omega} \times \vec{\mathbf{u}} + \beta \left(T - T_{\infty}\right) \left(\vec{\Omega} \times \vec{\Omega} \times \vec{\mathbf{r}}\right) + \nu \nabla^2 \vec{\mathbf{u}} \tag{B.1.2}$$

The above expression can be more conveniently expressed in non-dimensional form using the passage hydraulic diameter Dh and the area averaged inlet velocity U_b. The procedure is here proposed only for the x-component of eq. B.1.2.

$$U^* \frac{\partial U^*}{\partial x^*} + V^* \frac{\partial U^*}{\partial y^*} + W^* \frac{\partial U^*}{\partial z^*} = \tag{B.1.3}$$

$$= \frac{\mu}{\rho Dh} \nabla^2 U^* - \frac{1}{\rho {U_b}^2} \frac{\partial p}{\partial x^*} - 2\frac{\Omega Dh}{U_b} W^* - \frac{T - T_{bulk}}{T} \left(\frac{\Omega Dh}{U_b}\right)^2 \frac{R_m}{Dh} \tag{B.1.4}$$

where $x^* = x/Dh$ and $U^*, V^*, W^* = U, V, W/Dh$. Several well known dimensionless parameters can be recognised in, namely the Reynolds Number, Re, the Rotation Number, Ro, and the Buoyancy parameter, Bo.

$$Re = \frac{U_b Dh}{\nu} \tag{B.1.5}$$

$$Ro = \frac{\Omega Dh}{U_b} \tag{B.1.6}$$

$$Bo = \frac{T - T_{bulk}}{T} \left(\frac{\Omega Dh}{U_b} \right)^2 \frac{R_m}{Dh} \tag{B.1.7}$$

The Reynolds Number represents the ratio of inertial to viscous forces, the Rotation Number the one of the Coriolis to the inertial forces. An equivalent formulation of this latter is represented by the Rossby Number which is equal to 1/Ro. The Buoyancy parameter represents the ratio of centrifugal to inertial forces.

B.2 Heat transfer

Concerning the heat transfer, the non-dimensional parameter chosen is the Nusselt Number, that is:

$$Nu = \frac{hDh}{\lambda} \tag{B.2.1}$$

where h is the heat transfer coefficient and λ the thermal conductivity of the fluid.

B.3 Effect of Coriolis Forces on the flow

If the buoyancy therm is neglected, the three components of the Navier Stokes can be written as it follows:

x component

$$U\frac{\partial U}{\partial x} + V\frac{\partial U}{\partial y} + W\frac{\partial U}{\partial z} = \nu \nabla^2 U - \frac{1}{\rho}\frac{\partial p}{\partial x} - 2\Omega V \tag{B.3.1}$$

y component

$$U\frac{\partial V}{\partial x} + V\frac{\partial V}{\partial y} + W\frac{\partial V}{\partial z} = \nu \nabla^2 V - \frac{1}{\rho}\frac{\partial p}{\partial y} + 2\Omega U \tag{B.3.2}$$

z component

$$U\frac{\partial W}{\partial x} + V\frac{\partial W}{\partial y} + W\frac{\partial W}{\partial z} = \nu \nabla^2 W - \frac{1}{\rho}\frac{\partial p}{\partial z} \tag{B.3.3}$$

It is clear that the Coriolis forces have two effects, one in the x-component and one on the y-component. The $+2\Omega U$ in the y-component creates the well-documented Coriolis double vortex associated with pipe flow rotating in the orthogonal mode. The second effect raises if the y-component of the velocity is not negligible, in view of the developing of the aforementioned double vortex structure or, for example, of a flow redirection. If so the Coriolis effect associated to the -$2\Omega V$ therm in the x-component becomes important. This latter provides additional stream-wise acceleration to the flow near the wall and constitutes a deceleration for the bulk flow.

C

The effect on the flow field of the polyester filter at the duct outlets

In the following for the clearer reading of the present work the comparison between the flow field inside the cooling duct with and without the polyester fibre filter placed at the outlets is reported for Ro=0 to clarify that the flow features described in chapter 7 are fully maintained when the channel is equipped with the filter (in the following indicated as G0$\star$), beside small differences.

Figure C.1 presents the comparison of the time averaged velocity field and the stream-tracers in plane xy for G0 and G0$\star$. The main difference between G0 and G0$\star$ is that the separation bubble at the model tip is reduced.

Figure C.1 also shows that the separation bubbles at the downwind side of the pedestals are still found for G0$\star$, but their size is reduced, particularly at the IP passage P1. This fact is consistent with the adoption the filter. Indeed, it should be noticed that the pressure losses ascribed to the channel are very low ($\approx 60Pa$). When a high pressure loss, as the one imposed by the filter, is added at the outlets what happens is that the difference between the pressure drop across the different exits is smaller. Thus the coolant is more uniformly discharged throughout them. Moreover, the computations of the mass flow ratio across the different sections, performed whit the procedure described in section 7.1.1 revealed that a more uniform distribution is effectively obtained in G0$\star$. Nevertheless the ratio of the mass flow flowing at the TE to the one at the model tip observed for G0.

Looking at Fig. C.3, it is possible to observe that, beside the differences in the modulus of the V velocity, which have been already justified, the profile shape is comparable between G0 and G0$\star$.

In conclusion, it is possible to state that the flow field obtained whit the adoption of the filter is comparable whit the one observed without it. The definitive confirmation comes from the observation of the flow features reported in chapter 8.1 for Ro=0, which resemble the one made for G0, for example the horse shoe branch on the upstream side of the pedestal at the IP passage P4.

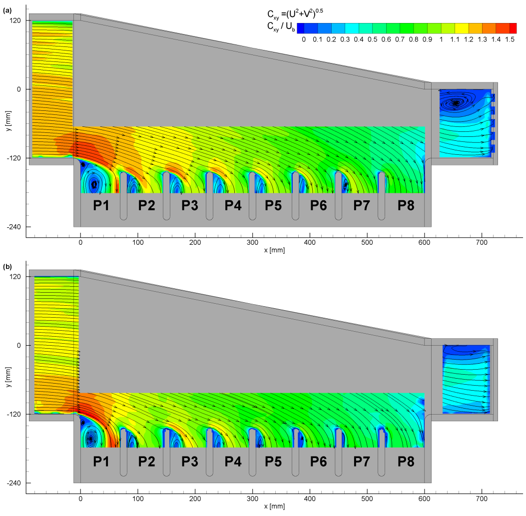

t!

FIGURE C.1 – Contours of time averaged in-plane velocity C_{xy} and stream-tracers on the symmetry plane xy without (a) and with (b) filter.

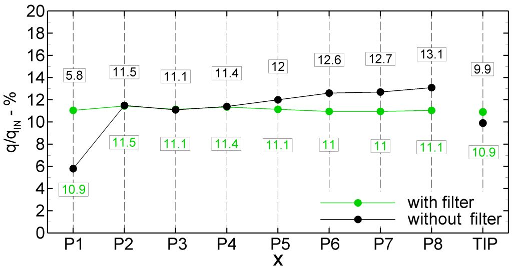

FIGURE C.2 – Comparison of the mass flow ratio across the different outlets of the channel with and without filter.

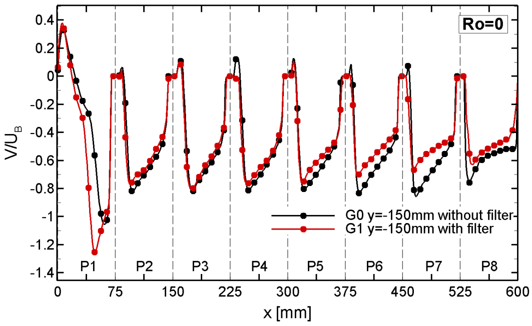

FIGURE C.3 – Comparison of v̌elocity profiles with and without filter at the outlets extracted from plane xy at $y = -150mm$.

D

Assessment of the settling chamber

The discussion on the potential flow effects in 8.1 is supported by the analysis of the the performance of the settling chamber hereby reported. Figure D.1 the U relative velocity profiles along y for Ro=0 (red line) and Ro=0.23 (green line) are presented.

The profiles have been extracted $10mm$ downstream the honeycomb filter Fig. D.2, which is responsible for the small perturbations. The profiles have been extracted from measurements performed without any test section attached to the settling chamber. It can be observed that the flow conditions can be reasonably considered the same for the

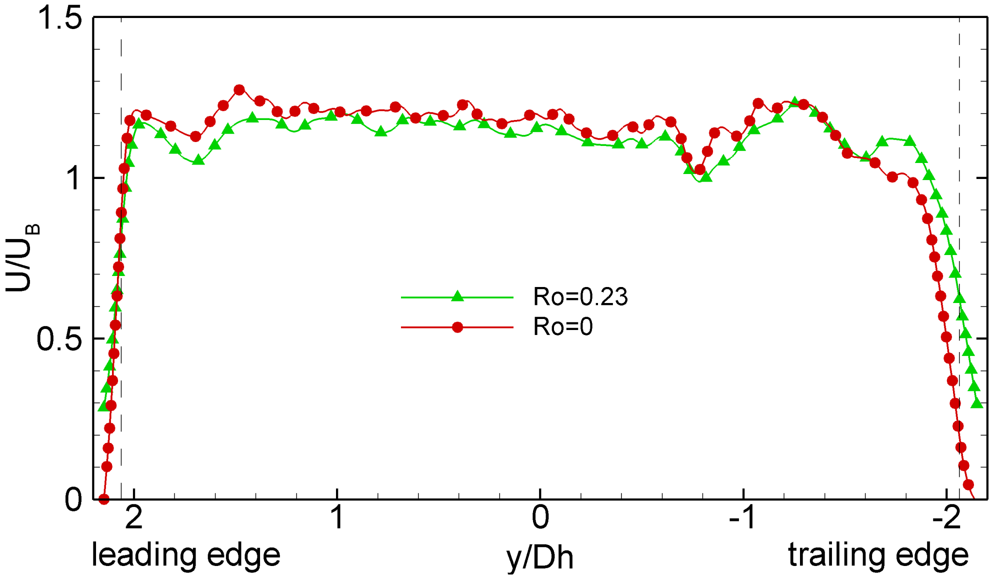

FIGURE D.1 – Stream-wise U velocity profile at $10mm$ from the honeycomb filter along y (D.2 extracted from measurement plane xy.

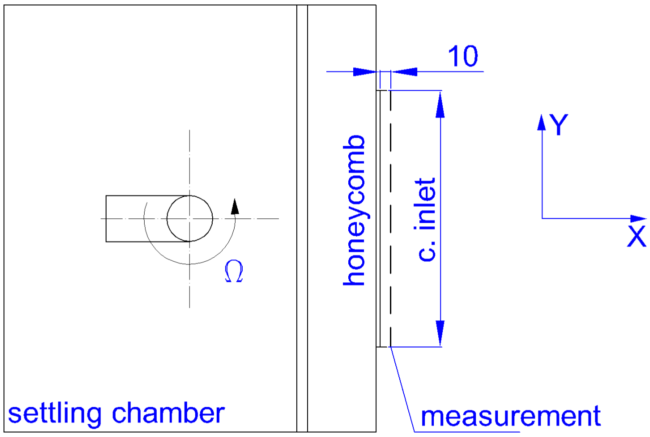

Figure D.2 – Scheme of the settling box and the position of the profiles in Fig. D.1

two cases, beside the region towards $y < 0$ where the effect of the peripheral velocity field is appreciable. Furthermore any flow separation can be noticed.

In view of these observations it is possible to state that the settling chamber guarantees flow conditions that are comparable for Ro=0 and Ro=0.23.

E

List of Pubblications

In the following the publications related to the present thesis are reported:

Journal articles

- A. Armellini, L. Casarsa, C. Mucignat; Flow field analysis inside a gas turbine trailing edge cooling channel under static and rotating conditions. International J. of Heat and Fluid Flow, 32(6), 1147-1159. doi:10.1016/j.ijheatfluidflow.2011.09.007
- A. Armellini, L. Casarsa, C. Mucignat, P.Giannattasio; Flow Field investigations in Rotating Facilities by means of stationary PIV systems. Measurement Science and Technology, 23(2), 025302. doi:10.1088/0957-0233/23/2/025302

Conference proceedings

- M. Pascotto, A. Armellini, L. Casarsa, C. Mucignat, P.Giannattasio; Effects of rotation and channel orientation on the flow field inside a trailing edge internal cooling channel, accepted for presentation at the ASME Turbo Expo 2012: Power for Land, Sea and Air, GT2012. Copenaghen, Denmark.
- Armellini, L. Casarsa, C. Mucignat; Analisi sperimentale delle prestazioni aerotermiche di canali di raffreddamento per il bordo d'uscita di pale di turbina a gas, proc. of 66th Congresso Nazionale ATI, Rende (Cosenza), 2011.
- Armellini, L. Casarsa, C. Mucignat; Effect of rotation on the flow field inside a trailing edge cooling passage, proc. of 9th European Turbomachinery Conference, Istanbul, Turkey, 21-25 March 2011.
- Armellini, L. Casarsa, C. Mucignat, P. Pinamonti; Indagine sperimentale del campo di moto in un canale di raffreddamento per il bordo d'uscita di pale rotoriche di turbina a gas; proc. of 65th Congresso Nazionale ATI, Cagliari, 2010.

Nomenclature

Notation	**Description**
C_{xyz}	Relative velocity modulus.
C_{xy}	In-plane velocity modulus in xy planes.
C_{yz}	In-plane velocity modulus in yz_{ip} planes.
P_{TE1}	Velocity profile along x at $y = -150mm$.
P_{TE2}	Velocity profile along x at $y = -234mm$.
P_{TE3}	Velocity profile along x at $y = -250mm$.
T_I	Turbulence intensity.
U_b	Bulk flow velocity.
U	Velocity along x.
V	Velocity along y.
W	Velocity along x.
ΔT_{Delay}	Delta T delay.
ΔT_{PIV}	Separation Time $[\mu m]$.
Δx	x axis displacement [px].
Δy	y axis displacement [px].
Δz	z axis displacement [px].
Ω	Angular velocity, $[rad/s]$.
u'	U velocity fluctuation.
v'	V velocity fluctuation.
w'	W velocity fluctuation.
xy'_{G2}	Measurement plane 1.5 mm parallel to the SS.
xy'	Measurement plane parallel to the SS.
xy_2	Measurement plane at $z = 10.55$ mm.
xy_3	Measurement plane at $z = 14.55$ mm.
xy_4	Measurement plane at $z = -14.55$ mm.
xy_{4-G1}	Measurement plane at $z = -14$ mm.
xy	Measurement plane $z = 0$ mm.
$xz - A$	Measurement plane at $y = -150$ mm.
$xz - B$	Measurement plane at $y = -165$ mm.
$xz - C$	Measurement plane at $y = -180$ mm.
xz_1	Measurement plane at $y = -150$ mm.
xz_2	Measurement plane at $y = -165$ mm.
xz_3	Measurement plane at $y = -180$ mm.
xz_{IN}	xz meas. plane at the c. inlet, at $y = 0$ mm.
x	x axis of reference frame, radial direction $[mm]$.
yz_{ip}	Measurement plane at $x = -262.5$ mm.
y	y axis of reference frame, $[mm]$.

Notation	Description
z	z axis of reference frame, wall normal direction $[mm]$.
AR	Cross-section aspect ratio (width/height).
Bo	Buoyancy parameter.
Dh	Hydraulic Diameter $[mm]$.
HTC	Heat Exchange Coefficient, $[\ W/m\ K]$.
M	Magnification Factor, $[Px/]$.
Nu	Nusselt Number.
Re	$Re = \rho D_h U_b/\mu$, Reynolds Number.
Ro	$Re = \omega D_h/U_b$ Rotation Number.

Acronyms

Notation	Description
2D-PIV	2-Dimensional Particle Image Velocimetry.
f-o-v	camera field-of-view.
FRAME B	second image of the PIV image pair.
G0	configuration G0.
G1	configuration G1.
G2	configuration G2.
IP	Inter Pedestal.
LCT	Liquid Crystal Thermography.
LE	Leading Edge.
PS	Pressure Side Wall.
QSD	Q-Switch delay.
S-PIV	Stereoscopic Particle Image Velocimetry.
SS	Suction Side Wall.
TE	Trailing Edge.
WIDIM	Window Displacement Iterative Multi-grid.

Bibliography

[1] Giovanni Lozza. *Turbine a gas e cicli combinati.* Società Editrice Esculapio, Bologna, 2006.

[2] Je-Chin Han. Recent Studies in Turbine Blade Cooling. *The International Journal of Rotating Machinery*, 10(6):443–457, November 2004.

[3] M. E. Taslim and T Li. Measurements of heat transfer coefficients in rib-roughned trailing-edge cavityies with crossover jets. Number Figure 1. ASME Paper NO-98GT-435, 1998.

[4] Alessandro Armellini, Filippo Coletti, Tony Arts, and Christophe Scholtes. Aerothermal Investigation of a Rib-Roughened Trailing Edge Channel With Crossing-JetsPart I: Flow Field Analysis. *Journal of Turbomachinery*, 132(1):011009, 2010.

[5] Filippo Coletti, Alessandro Armellini, Tony Arts, and Christophe Scholtes. Aerothermal Investigation of a Rib-Roughened Trailing Edge Channel With Crossing Jets - Part II: Heat Transfer Analysis. *Journal of Turbomachinery*, 133(3):031024, 2011.

[6] Jung-ho Choi, Shantanu Mhetras, Je-Chin Han, Sai C. Lau, and Ron Rudolph. Film Cooling and Heat Transfer on Two Cutback Trailing Edge Models With Internal Perforated Blockages. *Journal of Heat Transfer*, 130(1):012201, 2008.

[7] Bruno Facchini, F Simonetti, and L Tarchi. Experimental investigation of turning floe effects on innovative trailing edge cooilng configurations based on circuler and oblong pin fins. In *8Th European Turbomachinery Conference (ETC)*, Graz, Austria, 2009.

[8] T. Horbach, A. Schulz, and H.-J. Bauer. Trailing Edge Film Cooling of Gas Turbine Airfoil - External Cooling Performance of Various Internal Pin Fin Configurations. *Journal of Turbomachinery*, 133(4):041006, 2011.

[9] Giovanna Barigozzi, Silvia Ravelli, and A Perdichizzi. Pressure Side and Cutback Trailing Edge Film Cooling in a Linear Nozzle Vane Cascade at Different Mach Numbers. In *ASME Paper GT2011-*, 2011.

[10] J P Johnston, R M Halleen, and D K Lezius. Effect of spanwise rotation on the structure of two-dimensional fully developed turbulent channel flow. *Journal of Fluid Mechanics*, 56(3):533–557, 1972.

[11] R. Kristoffersen and Helge I. Andersson. Direct simulations of low-Reynolds-number turbulent flow in a rotating channel. *Journal of Fluid Mechanics*, 256:163–197, 1993.

[12] J E Hart. Instability and secondary motion in a rotating channel flow. *Journal of Fluid Mechanics*, 45:341–351, 1970.

[13] J. Pallares and L. Davidson. Large-eddy simulations of turbulent flow in a rotating square duct. *Physics of Fluids*, 12(11):2878–2894, 2000.

[14] Filippo Coletti, Thomas Maurer, Tony Arts, and Alberto Di Sante. Flow field investigation in rotating rib-roughened channel by means of particle image velocimetry. *Experiments in Fluids doi:10.1007/s00348-011-1191-2*, September 2011.

[15] Mauro Gallo and Tommaso Astarita. 3D reconstruction of the flow and vortical field in a rotating sharp U turn channel. *Experiments in Fluids*, 48(6):967–982, November 2009.

[16] Hector Iacovides, D C Jackson, B E Launder, and Y M. Yuan. An experimental study of a rib-roughened rotating U-bend flow. *Experimental Thermal and Fluid Science*, 19(3):151–159, 1999.

[17] T Liou, S Chang, J Hung, and S Chiou. High rotation number heat transfer of a 45 rib-roughened rectangular duct with two channel orientations. *International Journal of Heat and Mass Transfer*, 50(19-20):4063–4078, September 2007.

[18] L M Wright, W L Fu, and J C Han. Influence of entrance geometry on heat transfer in rotating rectangular cooling channles (AR=4:1) with angled ribs. *Journal of Heat Transfer*, 127:378–387, 2005.

[19] Yao-Hsien Liu, Michael Huh, Lesley M Wright, and Je-Chin Han. Heat Transfer in Trailing Edge, Wedge Shaped Cooling Channels with Slot Ejection under High Rotation Numbers. In *Proceedings of ASME Turbo Expo 2008*, Berlin, Germany, 2008.

[20] Shyy Woei Chang, Tong-minn Liou, Shyr Fuu Chiou, and Shuen Fei Chang. High Rotation Number Heat Transfer of Rotating Trapezoidal Duct With 45-deg Staggered Ribs and Bleeds from Apical Side Wall. In *Proceedings of GT2007 ASME Turbo Expo 2007*, Montreal, Canada, 2007.

[21] Alessandro Armellini, Luca Casarsa, and Claudio Mucignat. Rotational effects on the trailing edge cooling passage flow field. In *9Th European Turbomachinery Conference (ETC)*, Istanbul,Turkey, 2011.

[22] Ronald S. Bunker. Gas Turbine Heat Transfer: Ten Remaining Hot Gas Path Challenges. *Journal of Turbomachinery*, 129(2):193–201, 2007.

[23] M. E. Taslim and A. Nongsaeng. Experimental and Numerical Cross-Over Jet Impingement in an Airfoil Trailing-Edge Cooling Channel. *Journal of Turbomachinery*, 133(4):041009, 2011.

[24] Filippo Coletti, Manfredi Scialanga, and Tony Arts. Experimental Investigation of Conjugate Heat Transfer in a Rib-Roughened Trailing Edge Channel With Crossing Jets. *Journal of Turbomachinery*, 134(4):041016, 2012.

[25] S L Dixon. *Fluid Dynamics and Thermodynamics of Turbomachinery.* Butterworth-Heinemann, Woburn, MA, USA, 1998.

[26] Hans-Jurgen Rehder. Investigation of Trailing Edge Cooling Concepts in a High Pressure Turbine Cascade: Aerodynamic Experiments and Loss Analysis. In *Proceedings of ASME Turbo Expo 2009*, Orlando FL, U.S.A., 2009.

[27] Bruno Facchini, Francesco Simonetti, and Lorenzo Tarchi. Experimental Investigation of Turning Flow Effects on Innovative Trailing Edge Cooling Configurations With Enlarged Pedestals and Square or Semicircular Ribs. *ASME Conference Proceedings*, 2009(48845):795–806, 2009.

[28] Charles G Speziale. Numerical study of viscous flow in rotating rectangular ducts. *Journal of Fluid Mechanics*, 122:251–271, 1982.

[29] Charles G Speziale and S Thangam. Numerical study of secondary flows and roll-cell instabilities in rotating channel flow. *Journal of Fluid Mechanics*, 130:377–395, 1983.

[30] D. J. Tritton. Stabilization and destabilization of turbulnet shear flow in a rotating channel. *Journal of Fluid Mechanics*, 241:503–523, 1992.

[31] John Moore. *Effects of Coriolis on turbulent flow in rotating rectangular channels.* PhD thesis, 1967.

[32] J. P. Bons and J. L. Kerrebrock. Complementary Velocity and Heat Transfer Measurements in a Rotating Cooling Passage With Smooth Walls. *Journal of Turbomachinery*, 121(4):651–662, 1999.

[33] A Di Sante, R Theunissen, and R A Van Den Braembussche. A new facility for time-resolved PIV measurements in rotating channels. *Experiments in Fluids*, 44(2):179–188, 2008.

[34] Martin Elfert, M Voges, and J Klinner. Detailed flow investigation using PIV in a rotating square-sectioned two-pass cooling system with ribbed walls. In *Proceedings of ASME Turbo Expo 2008*, Berlin, Germany, 2008.

[35] Martin Elfert, Michael Schroll, and Wolfgang Forster. PIV Measurement of Secondary Flow in a Rotating Two-Pass Cooling System With an Improved Sequencer Technique. *Journal of Turbomachinery*, 134(3):031001, 2012.

[36] Martin Elfert, M. Schuler, H.M. Dreher, and S.O. Neumann. Numerical predictions of the effect of rotation on fluid flow and heat transfer in an engine-similar two-pass internal cooling channel with smooth and ribbed walls. In *Proceedings of ASME Turbo Expo 2010*, Glasgow (UK), 2010.

[37] Shyy Woei Chang, Tong-Miin Liou, and Yu Po. Coriolis and rotating buoyancy effect on detailed heat transfer distributions in a two-pass square channel roughened by 45 ribs at high rotation numbers. *International Journal of Heat and Mass Transfer*, 53(7-8):1349–1363, March 2010.

[38] F T Willet and A E Bergles. Heat transfer in rotating narrow rectangular ducts with heated sides oriented at 60 to the r-z plane. *Journal of Turbomachinery*, (123):288–295, 2001.

[39] Yao-Hsien Liu, Michael Huh, Je-Chin Han, and Hee-Koo Moon. High Rotation number effect on heat transfer in a triangular channel with 45, inverted 45, and 90 ribs. In *Proceedings of ASME Turbo Expo 2009*, Orlando FL, U.S.A., 2009. ASME.

[40] Michael Huh, Yao-hsein Liu, and Je-Chin Han. Effect of rib height on heat transfer in a two pass rectangular channel (AR=1:4) with a sharp entrance at high rotation numbers. *International Journal of Heat and Mass Transfer*, 52(19-20):4635–4649, September 2009.

[41] Michael Huh, Jiang Lei, Yao-Hsien Liu, and Je-Chin Han. High Rotation Number Effects on Heat Transfer in a Rectangular (AR=2:1) Two Pass Channel. In *Proceedings of ASME Turbo Expo 2009*, Orlando FL, U.S.A., 2009. ASME.

[42] Akhilesh P Rallabandi, Yao-Hsien Liu, and Je-Chin Han. Heat Transfer in Trailing Edge Wedge-Shaped Pin-Fin Channels With Slot Ejection Under High Rotation Numbers. *Proceedings of ASME Turbo Expo 2010*, 2010(43994):369–380.

[43] R. J. Adrian. Twenty years of particle image velocimetry. *Experiments in Fluids*, 39(2):159–169, July 2005.

[44] M. Raffel, C. Willert, S.T. Wereley, and J. Kompenhans. *Particle Image Velocimetry: a pratical guide.* Springer-Verlag Berlin Heidelberg, Berlin,Germany, 2007.

[45] F. Scarano and M L Riethmuller. Iterative multigrid approach in PIV image processing with discrete window offset. *Experiments in Fluids*, (29):513–523, 1999.

[46] A. K. Prasad. Stereoscopic particle image velocimetry. *Experiments in Fluids*, 29(2):103–116, August 2000.

[47] S.M. Soloff, R. J. Adrian, and Z C Liu. Distortion compensation for generalized stereoscopic particle image velocimetry. *Measurement Science Technology*, (8):1441–1454, 1997.

[48] N J Lawson and J Wu. Three-dimensional particle image velocimetry: error analysis of stereoscopic techniques. *Measurement Science Technology*, (8):894–900, 1997.

[49] C. Willert. Stereoscopic digital particle image velocimetry for application in wind tunnel flows. *Measurement Science and Technology*, 8:1465–1479, 1997.

[50] Tommaso Astarita and R. Giordano. Spatial resolution of the Stereo PIV technique. *Experiments in Fluids doi:10.1007/s00348-008-0589-y*, 2008.

[51] F. Scarano, L. David, M. Bsibsi, and D. Calluaud. S-PIV comparative assessment: image dewarping+misalignment correction and pinhole+geometric back projection. *Experiments in Fluids*, 39(2):257–266, July 2005.

[52] B. Wieneke. Stereo-PIV using self-calibration on particle images. *Experiments in Fluids*, 39(2):267–280, May 2005.

[53] Alessandro Armellini, Claudio Mucignat, Luca Casarsa, and Pietro Giannattasio. Flow field investigations in rotating facilities by means of stationary PIV systems. *Measurement Science and Technology*, 23(2):025302, February 2012.

[54] G Wuibaut, G Bois, P Dupont, G Caignaert, and M Stanislas. PIV measurements in the impeller and the vaneless diffuser of a radial flow pump in design and off-design operating conditions. *Journal of Fluids Engineering*, 124(3):791–797, 2002.

[55] H Hayami, M Hojo, and S Aramaki. Flow measurement in a transonic centrifugal impeller using a PIV. *Journal of Visualization*, 5(3):255–261, 2002.

[56] N Pedersen, P S Larsen, and C B Jacobsen. Flow in a centrifugal pump impeller at design and off-design conditions - Part I: Particle image velocimetry (PIV) and laser Doppler velocimetry (LDV) measurements. *Journal of Fluids Engineering*, 125(1):61–72, 2003.

[57] Y.-D. Choi, K Nishino, J Kurokawa, and J Matsui. PIV measurement of internal flow characteristics of very low specific speed semi-open impeller. *Experiments in Fluids*, 37(5):617–630, 2004.

[58] N Krause, K Zähringer, and E Pap. Time-resolved particle imaging velocimetry for the investigation of rotating stall in a radial pump. *Experiments in Fluids*, 39(2):192–201, 2005.

[59] G Wuibaut, G Bois, M El Hajem, A Akhras, and J Champagne. Optical PIV and LDV comparisons of internal flow investigations in SHF impeller. *International Journal of Rotating Machinery*, DOI 10.115, 2006.

[60] D Kearney, R Grimes, and J Punch. An experimental investigation of the flow fields within geometrically similar miniature-scale centrifugal pumps. *Journal of Fluids Engineering*, 131(10):1011011–10110110, 2009.

[61] R W Westra, L Broersma, K Van Andel, and N P Kruyt. PIV measurements and CFD computations of secondary flow in a centrifugal pump impeller. *Journal of Fluids Engineering*, 132(6):611041–611048, 2010.

[62] H Hayami, S Aramaki, and Y Watanabe. *PC-PIV System for a Measurement of Relative Flow in a Rotating Impeller.* The second international workshop on PIV, Fukui, Japan, 1997.

[63] S Aramaki and H Hayami. *Unsteady Flow Measurement in a Rotating Impeller Using PIV.* Proceedings of the 3rd International Workshop on Particle Image Velocimetry, Santa Barbara, USA, 1999.

[64] M T Stickland, T J Scanlon, P Waddell, J Fernandez-Francos, and E Blanco. Measurement of rotating flows using PIV and image derotation. *Experiments in Fluids*, 34(2):304–306, 2003.

[65] Yves Servouze, Christophe Brossard, and Pierre Gicquel. PIV Flow Field Measurements in a Rotating U-Shaped Channel . Comparison of smooth and 90 rib-roughened walls . In *Proceedings of the International Gas Turbine Congress IGTC2003*, Tokyo, Japan, 2003.

[66] M Gallo, Tommaso Astarita, and G M Carlomagno. *Experimental analysis of the flow field in a rotating 'U' channel.* 26th International Congress of the Aeronautical Sciences, Anchorage, Alaska, U.S.A., 2008.

[67] Martin Elfert, M. Shroll, and W. Forster. PIV-Measurement of secondary flow in a rotating two-pass cooling system with an improved sequencer technique. In *ASME Turbo Expo 2010*, Glasgow (UK), 2010.

[68] R Bharadwaj, J Poncer, and J D Jacob. *Effect of rotation on flow in a ribbed rotating turbine blade cooling duct model.* ASME AIAA SAE ASEE Joint Porpulsion Conference, Indianapolis, USA, 2002.

[69] Hector Iacovides, Diamantis Kounadis, Brian E. Launder, Jiankang Li, and Zeyuan Xu. Experimental Study of the Flow and Thermal Development of a Row of Cooling Jets Impinging on a Rotating Concave Surface. *Journal of Turbomachinery*, 127(1):222, 2005.

[70] Jan Visscher, Helge I. Andersson, Mustafa Barri, Henri Didelle, Samuel Viboud, Damien Sous, and Joël Sommeria. A new set-up for PIV measurements in rotating turbulent duct flows. *Flow Measurement and Instrumentation*, 22(1):71–80, March 2011.

[71] S J Kline and F A McClintok. Describing Uncertainties in Single Sample Experiments. *Mechanical Engineering Journal*, 75(1):3–8, 1953.

[72] Tommaso Astarita and Cardone G. Analysis of interpolation schemes for image deformation methods in PIV: effect of noise on the accuracy and spatial resolution. *Experiments in Fluids*, 40(6):977–987, 2006.

[73] M. R. Anderson and J. W. Baughn. Liquid-Crystal Thermography: Illumination Spectral Effects. Part 1: Experiments. *Journal of Heat Transfer*, 127(6):581, 2005.

[74] M Çakan. *Aero-Thermal Investigation of Fixed Rib-Roughened Internal Cooling Passages.* PhD thesis, Universitè Catholique de Louvain/Von Karman Institute for Fluid Dynamics, Belgium, 2000.

[75] N Akino, T Kunugi, K Ichimiya, K Mitsushiro, and M Ueda. Improved Liquid-Crystal Thermometry Excluding Human Color Sensation. *Journal of Heat Transfer*, 111(2):558–565, 1989.

[76] ISO 5167 UNI EN 2004 - Measurement of fluid flow by means of pressure differential devices inserted in circular cross-section conduits running full.

[77] Ronald S. Bunker. The Effects of Manufacturing Tolerances on Gas Turbine Cooling. *Journal of Turbomachinery*, 131(4):041018, 2009.

[78] Bruno Facchini and Lorenzo Tarchi. Investigation of innovative trailing edge cooling configurations with enlarged pedestals and square or semicircular ribs. Part1 - experimental results. In *Proceedings of ASME Turbo Expo 2008*, Berlin, Germany, 2008.

[79] Matteo Pascotto, Alessandro Armellini, Luca Casarsa, Giannattasio Pietro, and Claudio Mucignat. Effects of rotation and channel orientation on the flow field inside a trailing edge internal cooling channel. In *Proceedings of ASME Turbo Expo 2012*, Copenaghen, Denmark, 2012.

[80] Silvia Barigozzi, GiovannaRavelli. Effects of Trailing Edge Film Cooling on the Aerodynamic Performance of a Nozzle Vane Cascade. In *9TH European Turbomachinery Conference*, Istanbul,Turkey, 2011.

[81] William J Devenport and Roger L Simpson. Time-depeiident and time-averaged turbulence structure near the nose of a wing-body junction. *Journal of Fluid Mechanics*, 210:23–55, 1990.

[82] J L Fleming, R L Simpson, J E Cowling, and W J Devenport. Ex riments in Fluids An experimental study of a turbulent wing-body junction and wake flow. *Experiments in Fluids*, 14:366–378, 1993.

[83] F Ballio, C Bettoni, and S Franzetti. A Survey of Time-Averaged Characteristics of Laminar and Turbulent Horseshoe Vortices. *Journal of Fluids Engineering*, 120(2):233–242, 1998.

[84] Luca Casarsa and Tony Arts. Experimental Investigation of the Aerothermal Performance of a High Blockage Rib-Roughened Cooling Channel. *Journal of Turbomachinery*, 127(3):580, 2005.

[85] Olof Grundestam, Stefan Wallin, and Arne V. Johansson. Direct numerical simulations of rotating turbulent channel flow. *Journal of Fluid Mechanics*, 598:177–199, February 2008.

[86] M.H. Vavra. *Aero-Thermodynamics and Flow in Turbomachines.* Co., RE Krieger Publisher, 1974.

[87] Antonio Andreini, C. Bianchini, and B Facchini. Numerical analysis of the heat transfer in a trailing edge cooling duct in stationary and rotating conditions,. In *9TH European Turbomachinery Conference*, Istanbul,Turkey, 2011.

[88] Leonardo Bonanni, Carlo Carcasci, Bruno Facchini, and Lorenzo Tarchi. Heat tranfer measurements and effect of rotation in a trailing edge cooilng system. In *66 Congresso Nazionale ATI*, pages 5–9, Rende (Cosenza), 2011.

[89] Alessandro Armellini, L Casarsa, and P Giannattasio. Separated flow structures around a cylindrical obstacle in a narrow channel. *Experimental Thermal and Fluid Science*, 33(4):604–619, 2009.


UNIVERSITAS STUDIORUM UTINENSIS